Missouri S&T Library and Learning Resources

Scholars' Mine

Doctoral Dissertations | Student Theses and Dissertations

Spring 2019

Scaleable nanomanufacturing of metasurfaces using microsphere photolithography

Chuang Qu

Follow this and additional works at: https://scholarsmine.mst.edu/doctoral_dissertations

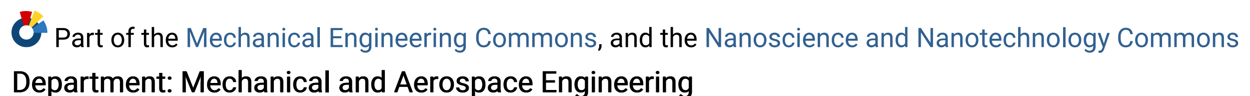

Part of the Mechanical Engineering Commons, and the Nanoscience and Nanotechnology Commons

Department: Mechanical and Aerospace Engineering

Recommended Citation

Qu, Chuang, "Scaleable nanomanufacturing of metasurfaces using microsphere photolithography" (2019). *Doctoral Dissertations*. 3137.
https://scholarsmine.mst.edu/doctoral_dissertations/3137

This thesis is brought to you by Scholars' Mine, a service of the Missouri S&T Library and Learning Resources. This work is protected by U. S. Copyright Law. Unauthorized use including reproduction for redistribution requires the permission of the copyright holder. For more information, please contact scholarsmine@mst.edu.

SCALEABLE NANOMANUFACTURING OF METASURFACES USING

MICROSPHERE PHOTOLITHOGRAPHY

by

CHUANG QU

A DISSERTATION

Presented to the Faculty of the Graduate School of the

MISSOURI UNIVERSITY OF SCIENCE AND TECHNOLOGY

In Partial Fulfillment of the Requirements for the Degree

DOCTOR OF PHILOSOPHY

in

MECHANICAL ENGINEERING

2019

Approved by:

Edward C. Kinzel, Advisor
Mahmoud Almasri
Kelly O. Homan
Heng Pan
Manashi Nath

© 2019

Chuang Qu

All Rights Reserved

PUBLICATION DISSERTATION OPTION

The dissertation consists of the following articles that have been published or submitted for publication as follows:

Paper I, pages 6-19 have been published in Journal of Optics Letters.

Paper II, pagers 20-35 have been published in Journal of Optical Express.

Paper III, pages 36-45 have been published in Proceedings of the ASME 2017 Heat Transfer Summer Conference as conference paper.

Paper IV, pages 46-56 have been published in Proceedings of SPIE - The International Society 2018 for Optical Engineering as conference paper.

Paper V, pages 57-80 have been summited to Journal of Micro/Nanolithography, MEMS, and MOEMS.

Paper VI, pages 81-93 have been published in Proceedings of the ASME 2018 13th International Manufacturing Science and Engineering Conference as conference paper.

ABSTRACT

The cost-effective manufacturing of metasurfaces over large areas is a critical issue that limits their implementations. Microsphere photolithography (MPL) uses a scalable self-assembled microsphere array as an optical element to focus collimated light to nanoscale photonic jets in a photoresist layer. This dissertation investigates the fabrication capabilities, process control, and potential applications of MPL. First, the MPL concept is applied to the fabrication of metasurfaces with engineered IR absorption (e.g. perfect absorption with multiband/broadband and wavelength/polarization dependences). Improving the patterning of the photoresist requires a fundamental understanding the photochemical photonic jet interactions. The dissertation presents a model of the MPL process with a cellular automata algorithm to simulate the development process. The model accurately predicts the size and shape of the features generated from MPL. It enables the identification of fabrication conditions to improve the resolution for the MPL process. Finally, the dissertation discusses the potential for a reusable microsphere array. Control of the contact forces is critical for minimizing the gap in between the microsphere array and the substrate and maintaining the consistent performance. Overall, the dissertation provides a foundation for understanding the process-structure-performance relationships for the fabrication of metasurfaces using microsphere photolithography. The use of the MPL for the fabrication of metasurfaces, with application such as sensing and thermal management, is novel as is the modeling of the MPL process.

ACKNOWLEDGMENTS

I would like to thank my academic advisor, Dr. Edward Kinzel, for his guidance and support on my entire doctoral career. I am profoundly grateful to grow up with Dr. Kinzel to be a better engineering researcher and a better person.

I would gratefully acknowledge financial support from NSF (ECCS-1509589, CMMI-1653792), as well as the Material Research Center at the Missouri University of Science and Technology.

I would like to thank all my committee members, Dr. Mahmoud Almasri, Dr. Kelly Homan, Dr. Heng Pan, and Dr. Manashi Nath, for offering me invaluable feedback and help on my research.

I would like to thank Mr. Chen Zhu and Mr. Kelly Mauntel, who assisted me with the research. I would like to thank my former and current co-workers in Thermal Radiation Lab: Mr. Jacob S. Wilson, Dr. Junjie Luo, Mr. Arvindvivek Ravichandran, Mr. Harshvardhan Sahu, Mr. John M. Hostetler, Mr. Cody Lough, Mr. Nicholas Capps, Mr. Tristan Cullom.

Finally, I would like to thank my parents, Mr. and Mrs. Qu, who support all my decisions and love me unconditionally.

TABLE OF CONTENTS

Page

PUBLICATION DISSERTATION OPTION iii

ABSTRACT iv

ACKNOWLEDGMENTS v

LIST OF ILLUSTRATIONS ix

LIST OF TABLES xiii

SECTION

1. INTRODUCTION 1

1.1. BACKGROUND 1

1.2. RESEARCH OBJECTIVES 3

PAPER

I. POLYCRYSTALLINE METASURFACE PERFECT ABSORBERS/EMITTERS FABRICATED USING MICROSPHERE PHOTOLITHOGRAPHY 6

ABSTRACT 6

REFERENCES 18

II. INFRARED METASURFACES CREATED WITH OFF-NORMAL INCIDENCE MICROSPHERE PHOTOLITHOGRAPHY 20

ABSTRACT 20

REFERENCES 33

III. THERMAL RADIATION FROM MICROSPHERE PHOTOLITHOGRAPHY PATTERNED METASURFACES 36

ABSTRACT 36

REFERENCES 44

IV. FABRICATION OF INFRARED BROADBAND POLARIZED EMITTING METASURFACES USING MICROSPHERE PHOTOLITHOGRAPHY 46

ABSTRACT 46

1. INTRODUCTION 47

2. EXPERIMENT 49

3. CONCLUSION 53

REFERENCES 55

V. MODELING OF MICROSPHERE PHOTOLITHOGRAPHY 57

ABSTRACT 57

1. INTRODUCTION 58

2. FABRICATION PROCESS 60

3. MODELING 64

4. DISCUSSION 66

4.1. RESOLUTION STUDY 66

4.2. SIMULATION FOR OFF-NORMAL ILLUMINATIONS 73

5. CONCLUSION 75

REFERENCES 78

VI. MASK-BASED MICROSPHERE PHOTOLITHOGRAPHY 81

ABSTRACT 81

1. INTRODUCTION 81

2. EXPERIMENTS AND DISCUSSION 83

3. CONCLUSIONS 90

REFERENCES 91

SECTION

2. CONCLUSION 94

APPENDICES

A. MATLAB CODE FOR SIMULATION OF MICROSPHERE PHOTOLITHOGRAPHY 97

B. CONSTRAINED SELF-ASSEMBLY OF MICROSPHERES 106

BIBLIOGRAPHY 123

VITA 127

LIST OF ILLUSTRATIONS

Page

PAPER I

Figure 1. Illustration of MPL technique used for patterning metal- insulator-metal metasurfaces. 10

Figure 2. Simulated MPL E-field intensity enhancement for 480-nm-thick photoresist layer on 180 nm Si/optically thick Al substrate illuminated at 365 nm 11

Figure 3. Measured diameter of MPL-patterned Al disks after lift-off. 12

Figure 4. Comparison between simulated (dashed lines) and measured (solid lines) absorption spectra for different diameter disks 14

Figure 5. Polycrystalline metasurface with $d = 720$ nm and $p = 1.93$ μm. 16

Figure 6. Measured absorption spectra for single and polycrystalline areas. 17

Figure 7. Simulated electric field for an infinitely large single-crystal metasurface with $d = 653$ nm at $\lambda = 5.00$ μm for TE illumination incident from 29.5° 17

PAPER II

Figure 1. Illustration of fabrication procedure (a) directional illumination of self-assembled microspheres from polar angle, θ, and azimuthal angle, φ, (b) pattern revealed in photoresist after exposure and development (c) final metal split-ring resonators after lift-off 25

Figure 2. Simulation of off-axis exposure of different sized microspheres. 26

Figure 3. SEM images taken from 52° of hole-pairs after FIB cross sectioning (a) 1.44 mJ/cm^2, ±10°; (b) 3.6 mJ/cm^2, ±10°; (c) 3.6 mJ/cm^2, ±25° 27

Figure 4. (a)-(c) SEM images of disks pairs (E=7.2 mJ/cm^2, θ=±35°, p=3 μm) after lift-off (a) φ=13°, (b) φ=52°, and (c) φ=22° resulting from different orientations of the microsphere lattice relative to the illumination directions. 28

Figure 5. Measured disk displacement normalized to sphere diameter for deposited disks produced with different incident angles. 28

Figure 6. Reflectance spectra of split ring resonator sample shown in the inset (SEM image).. 31

Figure 7. Absorption spectra of tripole FSS shown in the inset (SEM image)..... 32

PAPER III

Figure 1. Fabrication of metasurface with MIMIM structure using Microsphere Photolithography (a) microspheres applied on photoresist on Si/Al films (b) holes revealed after photolithography and development (c) deposition of Al/Si/Al (d) final MIMIM structure with Al/Si/Al disk stack on Si/Al..... 39

Figure 2. SEM image of the MIMIM disc arrays (a) top view (b) 45° tilt during imaging. 41

Figure 3. Absorption spectra of MIMIM (black) & MIM (red) samples with disk diameters of (a) 566 nm (b) 720 nm (c) 824 nm (d) 894 nm..... 42

Figure 4. Thermal image of MIM-structure metasurface fabricated by MPL hierarchical patterning. 43

Figure 5. Absorptance/Emittance spectra of S&T logo area (blue) and background area (red) 43

PAPER IV

Figure 1. Illustration of creating dipole patterns in MPL process. 50

Figure 2. HFSS simulation of polarized metasurface at 30° off-normal illumination when the dipoles are parallel to the plane of incidence (assuming optimized dimensions and film thicknesses). 52

Figure 3. (Left) SEM image of dipole arrays fabricated in MPL approach (Right) Absorption spectra of TE (red) TM (blue) incidences from sample exposed with polar angle from -27° to 27°. 54

Figure 4. Thermal images of hierarchical FSS metasurface through a polarizer whose orientation (a) parallel to the polarization of emittance (b) perpendicular to the polarization of emittance..... 54

PAPER V

Figure 1. Exposure model 63

Figure 2. (a) E/E_0 ratio from HFSS simulation; (b) Hole profile generated from development model (scale changed for matching (c)); (c) Hole profile from SEM image with 52° tilt while imaging. The hole is in 540 nm photoresist; exposure dosage for this sample is 1.14 mJ/cm^2; the development duration is 15s. 66

Figure 3. (a) Hole diameter versus exposure dosage on various thicknesses of photoresist with 15 seconds development durations. Red, green, and blue dots/lines are for the 120 nm photoresist, 260 nm photoresist, and 540 nm thick photoresist, respectively. Representative SEM images of hole arrays for (b) 120 nm thick photoresist with exposure dosage of 2.71 mJ/cm^2; (c) 120 nm thick photoresist with exposure dosage of 0.42 mJ/cm^2; (d) 120 nm thick photoresist with exposure dosage of 10.50 mJ/cm^2; (e) 540 nm thick photoresist with exposure dosage of 10.50 mJ/cm^2. Scale bar: 2 μm.............. 67

Figure 4. (a) Hole diameter versus exposure dosage for various development durations on 540 nm thick photoresist. The blue and orange symbols are for the 15 and 60 seconds developments, respectively. (b) SEM image of the sample processed with 4.26 mJ/cm^2 exposure dosage and 60 seconds development time; (c) SEM image of the sample processed with 4.26 mJ/cm^2 and 15 seconds development time. Scale bar: 2 μm.......... 68

Figure 5. (a) Hole profiles with exposure dosage of 0.42 mJ/cm^2 and development durations of $0.8\tau_{min}$, τ_{min}, $1.2\tau_{min}$ and $2.4\tau_{min}$; (b) Hole profiles with exposure dosage of 1.73 mJ/cm^2 and development durations of $0.8\tau_{min}$, τ_{min} and $1.2\tau_{min}$ and $2.4\tau_{min}$;(c) The dependence of the diameter of holes (color) on exposure dosage (x) and development time (y); (d) The trade-off relation between the minimum development time τ_{min} and minimum exposure dosage E_{exp} for a through-hole for three thicknesses; (e) Sensitivity curve s_1 describing the exposure dosage dependency of the diameter of the holes; (f) Sensitivity curve s_2 describing the development time dependency of the diameter of the holes. 71

Figure 6. SEM images of (a) sub-100 nm holes (b) sub-100 nm Al disk array (c) sub-100 nm disks are from the fabrication condition of 120 nm photoresist, 0.42 mJ/cm^2 exposure dosage, and 15 second development time. 73

Figure 7. Hole profiles from simulation (a) 5s development, xz plane (b) 5s development, yz plane (c) 120s development, xz plane (d) 120s development, yz plane and experiment (e) 5s development, xz plane. The exposure is in xz plane with an angle of 30° and exposure dosage of 1.14 mJ/cm^2. (f) Effective diameter of holes for various development durations and exposure dosages. .. 76

Figure 8. Simulation results and corresponding SEM images of split-ring resonators 77

PAPER VI

Figure 1. Illustration of mask-based microsphere photolithography approach 84

Figure 2. SEM image of microsphere mask (tape) with inset showing 2D Fourier Transform.. 85

Figure 3. SEM image of holes in S1805 photoresist 87

Figure 4. Experimental results showing the change in pattern periodicity due to diffractive effects at large gaps (a) 2 μm periodicity (b) 1 μm periodicity. Scale bar: 5 μm. Simulation on MPL exposure process with different gaps (c) 0 μm (d) 10 μm.. 88

Figure 5. SEM images of samples 1, 6, 8 and 13.. 88

Figure 6. Measured absorptance for different metasurfaces patterned with a common microsphere mask. The simulated absorptance is plotted with a dashed line.... 89

Figure 7. Properties of the different samples (a) resonant wavelength and (b) resonant absorptance. 91

LIST OF TABLES

PAPER V Page

Table 1. Fitting parameters used in the model 66

SECTION

1. INTRODUCTION

1.1. BACKGROUND

Metamaterials are composite structures that create extraordinary responses. Metasurfaces are two-dimensional metamaterials composed of networks of subwavelength of antenna elements. Over the past decade, there has been extensive research interest in the development of optical/infrared metasurfaces [1]. Many design concepts can be adapted from frequency selective surfaces (FSS) applied in radio frequency. FSS application in radio/microwave frequencies begins in 1960s and was applied as hybrid radome, band-pass filters, circuit analog absorbers, etc. [2]. The ability to control the interaction between radiation and the surface can be scaled from radio/microwave to infrared and optical frequencies. The critical difference is that the feature sizes scale with wavelength, which shrink from millimeters to less than a micrometer at visible/near infrared wavelengths. The size-shrink brought more applications for infrared spectrum including sensors [3], daytime radiative cooling [4], and enhancing the performance of direct energy conversion devices such as thermophotovoltaic emitters [5]. The achievement of size reduction requires a dramatic change in fabrication processes. The goal of this study is to create functional infrared metasurfaces in a scalable and cost-effective way.

There are certain fabrication requirements of infrared metasurfaces: feature size/distribution, device area, fabrication efficiency in terms of both cost and time, etc. Conventional photolithography applied in integrated circuit (IC) manufacturing is one of

the choices. The conventional UV light source suffers with the diffraction limit; the photomask used in the process is rigid and expensive. An alternative approach is NanoImprint Lithography (NIL). Roll-to-roll NIL has also been demonstrated for patterning IR metasurfaces for filters and photovoltaics [6]. NIL process also requires an expensive mask, which is usually patterned with Electron Beam Lithography (EBL) and Reactive Ion Etching (RIE). Two significant obstacles to the industrial implementation of the process are the expense of the mask (nanoscale features must still be patterned using EBL and the roller mask is still subject to wear) and the expense of metallization (high vacuum metal deposition).

Some maskless techniques such as EBL [7] and focused ion beam (FIB) milling [8] are options for fabrication of resolution as small as sub-10 nm. However, these techniques are not efficient as cost and time, especially for mass productions. Interference lithography [9] is another photolithography technique that exploits interference by mirror interferometer for patterning. However, interference lithography is very sensitive to displacements, and large area patterning requires laser beams of very good homogeneity. This raises issues when applied to large areas and in high throughput approaches such as roll-to-roll fabrication.

Colloidal particles were first used for lithography since the early 1990s. Nanosphere Lithography (NSL) is used to generate plasmonic structures in the visible and near-IR [10-11]. A self-assembled Hexagonal Closed Packed (HCP) particle array acts as a physical shadow/etch mask, and the nanopattern through the interstitial locations in the lattice can be transferred on or through substrate. However, as the nanospheres cannot be recollected in the NSL process, it is unlikely to be used for large-scale

nanomanufacturing problems. The alternative of using microspheres as shadow masks is to use them as optical elements, as Microsphere Photolithography (MPL). In this technique, the microspheres are in contact with the photoresist layer and focus incident light to photonic jets with FWHM of as small as $\lambda/3$ [12]. This is a result of both evanescent and propagating fields that allow the subwavelength photonic jet to extend more than λ into the photoresist [13]. Previous work on demonstration of exploiting photonic jets for patterning by Mohseni's group are shown in [14-18].

Numerical simulation is an important aspect in photolithography research. The exposure and development procedures can be optimized by the simulation results, which enables the creation of smaller features. The key for predicting the resist profile is to determine the intensity distribution of the light inside the photoresist. In the exposure kinetics, the UV illumination decomposes the photoactive compound (PAC) inside the photoresist; this results in a relative concentration of the PAC to the original state. The development rate is highly depend on the concentration of the PAC based on Original Mack model [19]. Thus, the resist profile can be obtained combining the development rate matrix and etching algorithms. Common algorithms used for development simulations for positive photoresist reported are cell-removal, ray tracing, string models, and linear weight method [20-21].

1.2. RESEARCH OBJECTIVES

The main objective of this dissertation is to describe the fabrication capabilities of microsphere photolithography for infrared metasurfaces. With the modeling of the MPL,

the fabrication conditions for metasurfaces with particular designs can be predicted and optimized. The dissertation contains six papers on three research topics.

The first research topic focuses on the creation of functional infrared metasurfaces with various designs using microsphere photolithography, including Papers I-IV. Paper I demonstrates the fabrication and characterization of a basic Metal-Insulator-Metal (MIM) perfect absorber metasurface with Al disks as the top layer. The dependency of the diameter of the Al disks on the exposure dosage will be shown. The tunable perfect absorber metasurfaces in mid-wave infrared spectrum varied with the diameter of the disks will be proved as well. Paper II introduces the ability of MPL to fabricate complicated micron-scaled antenna elements by off-normal incidence illuminations. The key point in this study is the discussion on the relationship between the offset of the feature to the center of the sphere scales with the illumination angle and the size of the microsphere. This fabrication rule enables the fabrication of infrared metasurfaces with complicated designs such as split-ring resonator and tripole elements. Papers III and IV discuss the designs for expanding the absorption bandwidth and achieving polarization dependences of the metasurfaces created by microsphere photolithography. Paper III mainly discusses the design and fabrication of dual-band absorption of metasurfaces using MPL by coupling with additional MIM resonator. Paper IV talks about the design of broadband absorption by coupling the resonances of the MIM cavity the SiO_2 phonon mode. The polarization dependence of the metasurfaces is designed as well by dipole elements. Both papers will show the hierarchical patterning abilities of MPL as well.

Modeling and simulation of the MPL process is the second research topic in this dissertation, as shown in Paper V. This paper introduces the modeling of the

development process for predictions of the size and shape of the features generated from MPL. The specialty in MPL comparing to conventional photolithography simulations is energy distribution inside the photoresist caused by the photonic jet. The distinctive energy distribution affects the flow rate and route of the developer, and eventually the feature is formed inside the photoresist based on the development procedure. The model will be experimentally validated for three major process parameters: exposure dosage, thickness of photoresist, and development duration. The verified model helps with determining the fabrication conditions for obtaining sub-100 nm features. Finally, the ability of the simulation for off-normal incident illuminations will be discussed by the demonstration of the creation of split-ring resonators.

One drawback of MPL in aforementioned papers is that the microspheres are not reusable. In those papers, the microspheres were directly deposited onto the photoresist and washed away during development. The third research topic focuses on the method to reuse the microspheres—mask-based microsphere photolithography (Paper VI). The key to this research is to have a conformal contact of a microsphere mask to the photoresist while the sphere mask is not wearing out after contacts. Good consistency of the absorption behavior of the perfect absorber metasurfaces is expected by improving the contact of the flexible substrates and a flexible sphere mask using the weight system. The result means to provide foundation for roll-to-roll fabrication with microsphere photolithography.

PAPER

I. POLYCRYSTALLINE METASURFACE PERFECT ABSORBERS/EMITTERS FABRICATED USING MICROSPHERE PHOTOLITHOGRAPHY

Chuang Qu and Edward C. Kinzel

Department of Mechanical and Aerospace Engineering,

Missouri University of Science and Technology, Rolla, MO, 65409, USA

ABSTRACT

Microsphere photolithography (MPL) is a practical, cost-effective nanofabrication technique. It uses self-assembled microspheres in contact with the photoresist as microlenses. The microspheres focus incident light to a sub-diffraction limited array of photonic jets in the photoresist. This letter explores the MPL technique to pattern metal-insulator-metal metasurfaces with near-perfect absorption at mid-wave infrared (MWIR) frequencies. Experimental results are compared to electromagnetic simulations of both the exposure process and the metasurface response. The microsphere self-assembly technique results in a polycrystalline metasurface; however, the metal-insulator-metal structure is shown to be defect tolerant. While the MPL approach imposes geometric constraints on the metasurface design, once understood, the technique can be used to create functional devices. In particular, the ability to tune the resonant wavelength with the exposure dose raises the potential of hierarchical structures.

Keywords: Nanolithography; Metamaterials; Nanostructure fabrication; Absorption; Subwavelength structures, nanostructures.

Metasurfaces have significant potential for controlling the way that structures interact with light. This allows the surface radiative properties to be engineered, in turns controlling radiation heat transfer to/from the surface. The radiative properties are a function of the geometry of the sub-wavelength antenna elements that constitute the metasurface. For example, a metal-insulator-metal metasurface can be designed to achieve near-unity absorption over a narrow spectral band. These perfect absorber structures have been demonstrated for frequencies ranging from microwave [1], to visible [2]. At infrared wavelengths, they have applications such as sensors [3–5], selective thermal emitters for energy harvesting (thermophotovoltaics) [6] and thermal transport control [7]. The infrared (IR) region is of particular relevance because it corresponds to the spectral region where the majority of energy is emitted from terrestrial sources.

The metal-insulator-metal configuration allows for impedance matching to free-space at discrete frequencies. Various patterns for perfect absorbing infrared metasurfaces have been proposed and studied. Different patterns provide varying degrees of field concentration and different quality factors. However, economically patterning the nanoscale geometry of an IR metasurface over area scales relevant to practical applications remains a significant challenge. For thermal transport, this can mean precisely patterning features as small as 200 nm over m^2 areas. The expense of this has limited the use of visible and IR metasurfaces to laboratory demonstrations.

For laboratory-scale fabrication, patterning is typically accomplished using the various top-down lithography techniques developed for semiconductor fabrication, such as e-beam lithography (EBL) [3–5,7], focused ion-beam milling (FIB) [8], X-ray lithography (XRL), projection optical lithography with steppers, nanoimprint lithography

(NIL) [6,9], and interference lithography [10]. While suitable for prototypes, EBL and FIB have low throughput, and per area costs exceed \$1 million/m^2.

Bottom-up techniques, which are based on a self-assembled mask, are, on the other hand, particularly appealing for metasurface applications because of significantly lower fabrication costs on a per-area basis and the potential to pattern non-planar substrates. A number of bottom-up techniques have been realized for creating metasurfaces. These include nanosphere lithography (NSL) [11] or colloidal lithography [12, 13]. In these techniques, a self-assembled microsphere array serves as a shadow mask during direction evaporation. An alternative technique, microsphere photolithography (MPL), was proposed by the Mohseni group [14–17]. This uses flood illumination of self-assembled microsphere arrays to focus sub-diffraction- limited photonic nanojets into photoresist. Conceptually, it is related to nanoparticle lens lithography (NLL) [18] using micro- spheres for laser ablation, and also to nanosphere photolithography (NSPL), using nano-level diameter spheres [19].

The various microsphere self-assembly techniques are capable of sub-100-nm features with periodicities determined by the diameter of the microspheres [16]. This imposes constraints on the metasurface design. The flexibility of these techniques can be increased by incorporating a number of off-axis approaches, directional evaporation [20], or illumination [17], to permit more complex metasurface elements to be patterned. Another significant issue is that despite recent advances for creating self-assembled single-crystal 2D microsphere monolayers, most self-assembled arrays are often polycrystalline. This microstructure is transferred to the patterned metasurface and differs from conventional top-down patterning approaches yielding single-crystal

patterns. There is limited work characterizing metasurfaces in the presence of microstructure defects such as grain boundaries, vacancies, dislocations, and locally misshaped features.

This Letter explores microsphere photolithography for patterning simple metal-insulator-metal (near) perfect metasurface absorbers at mid-wave infrared (MWIR) frequencies. It shows that the resonant wavelength for the metasurface can be adjusted by controlling the illumination dose with an average absorptance of greater than 0.95 over the 3.6–5.9 μm band. The resulting metasurface has a polycrystalline microstructure but is shown to be defect-tolerant because of low inter-element coupling.

Figure 1 illustrates the MPL process used in this Letter. 150-nm-thick aluminum followed by h = 180 nm of silicon are deposited onto glass substrate using e-beam evaporation. Following evaporation, adhesion promoter (HDMS, Silicon Resources) and photoresist (S1805, Shipley) are spin-coated onto the photoresist. After softbaking, the photoresist thickness is 480 nm. An 8.9%-by-weight aqueous suspension of polystyrene microspheres (Polysciences, Inc.) is drop-coated onto the photoresist surface. The spheres are p = 1.93 μm in diameter. As the water evaporates, the microspheres self-assemble into a hexagonal close-packed (HCP) lattice. The water evaporation/self-assembly process takes about one hour at room temperature.

After self-assembly the entire sample is flood-exposed using i-line illumination (Karl Suss MA6 mask aligner). The exposure duration is varied between different samples. After exposure, the samples are immersed in MF 319 developer (Dow) for 60 seconds, followed by rinsing with deionized water and drying with compressed air. Both the exposed areas of photoresist and the polystyrene microspheres are removed during the

development process. The sample is then hard-baked and 100 nm of aluminum is deposited using e-beam evaporation. The remaining photoresist is then lifted off using Remover PG (MicroChem) and ultrasonication. This reveals a uniform periodic aluminum disk array with geometry defined by three parameters—the dielectric thickness, *h*, controlled by the deposited thickness of silicon film; the periodicity, *p*, controlled by the diameter of the microspheres; and the disk diameter, *d*, controlled by the exposure duration.

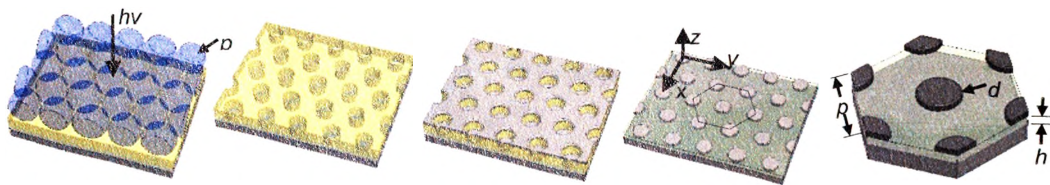

Figure 1. Illustration of MPL technique used for patterning metal- insulator-metal metasurfaces. (a) Flood exposure of self-assembled microsphere hexagonal close-packed (HCP) array; (b) hole array in photoresist after development; (c) deposition of top metal layer; and (d) the final structure after lift-off with (e) close-up showing metasurface defined by periodicity, *p*, disk diameter *d*, and insulator thickness, *h*.

Each microsphere focuses incident light to a sub-wavelength photonic jet. Figure 2 shows results from a frequency-domain finite element model (HFSS, ANSYS) of the exposure process for microspheres on top of a S1805/Si/Al substrate illuminated by normally incident, unpolarized 365-nm radiation. The simulated microsphere array has infinite periodic extents. Standing waves form in the photoresist due to reflection from the high-impedance silicon layer. This makes the exposure highly dependent on the choice of dielectric. The electric field intensity along the centerline is plotted in the inset

of Figure 2(c) with a maximum $z = 94$ nm from the surface and a minimum at the interface at the photoresist/Si interface ($z = 480$ nm from the surface). While the photonic jet at 94 nm is nearly axially symmetric, interestingly deviations occur in the azimuthal direction at the surface of the silicon ($z = 480$ nm). These result in a higher-exposure threshold along the 30° plane than in the 0° plane [indicated in Figure 2(b)]. This produces a hexagonal exposed pattern for large exposure energies as shown in the insets of Figure 2(d).

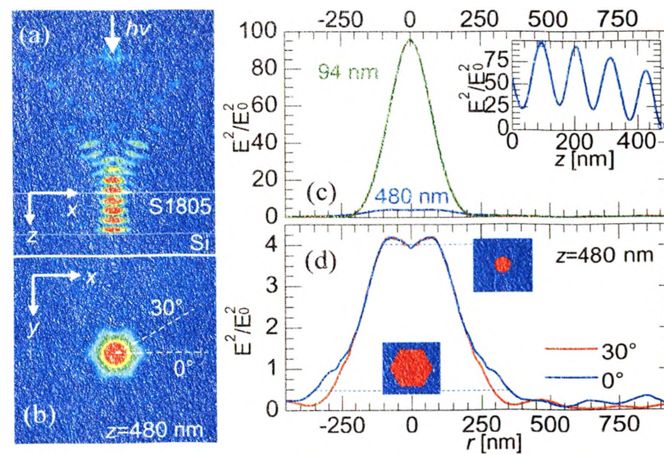

Figure 2. Simulated MPL E-field intensity enhancement for 480-nm-thick photoresist layer on 180 nm Si/optically thick Al substrate illuminated at 365 nm. (a) Enhancement in the x–z plane, saturated at 50×; (b) x–y plane immediately above the Si layer, saturated at 4.2×; (c) 94 nm into the PR where field is a maximum with inset showing response along the centerline immediately beneath the microsphere; and (d) enhancement 480 nm into the photoresist where field in a minimum.

Figure 3 shows how the diameter of the deposited disks (after lift-off) varies with exposure dose (controlled with the exposure duration). The diameter of the disks was

measured using SEM imaging, and the error bars denote the standard deviation over 1× 1 mm² fields. The insets in Figure 3 show SEM images of typical patterns. Higher-exposure dosages lead to larger disks and above a specific exposure dosage (25 mJ/cm²), with the circular disks becoming hexagonal. The datasheet threshold dose for the photoresist is 30 mJ/cm² with a contrast ratio of 2.3. The lower-exposure doses in the experiment agree with a focusing effect (field concentration) provided by the microspheres (shown in Figure 2). Qualitatively, the results in Figure 3 agree with those in Figure 2 albeit with a larger-than-predicted diameter. This can be attributed to partial-exposure effects and photo-bleaching in the photoresist. The relationship between the size of the disks and the exposure dosage is nearly linear, providing a predictable and controllable disk diameter.

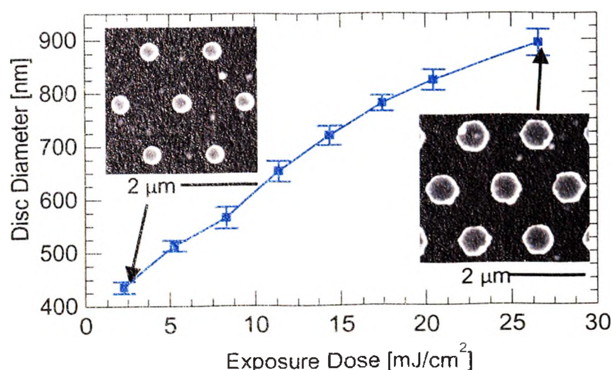

Figure 3. Measured diameter of MPL-patterned Al disks after lift-off. All samples use p =1.93 μm-diameter spheres. Insets show SEM circular and hexagonal features produced using exposure dosages of 2.28 and 26.6 mJ/cm², respectively.

The absorption spectra of the patterned metasurfaces were acquired by measuring the reflection spectra with a Fourier transform infrared spectrometer (FTIR, Thermo Nicolet Nexus 670) and IR microscope (Nicolet Continuum). This was equipped with a liquid-nitrogen-cooled mercury cadmium telluride (MCT) detector and KBr beam splitter, and purged with nitrogen gas. The reflectance spectra, $R(\lambda)$ was normalized to the reflectance from a gold mirror. A 32 × NA 0.65 objective is used to illuminate and collect radiation from a hollow cone with angles ranging from 18° to 41°. An aperture limits the interrogation area to 50 μm × 50 μm. Because of the ground plane in the metasurface there is no transmittance, and the absorptance, $A(\lambda)$, can be calculated directly from the reflectance, $A(\lambda) = 1 - R(\lambda)$.

Figure 4 compares the measured FTIR absorptance and HFSS simulation for six of the specimens with diameters measured in Figure 3. The HFSS results were calculated using ellipsometrically measured properties for e-beam evaporated films of aluminum and silicon (IR-VASE, J.A. Woollam). The simulation results predict near perfect absorptance across the MWIR (average maximum absorptances over the six samples of measured experimental results in Figure 4. The average maximum $A_{max} = 0.98$). These results agree very well with the FTIR-absorptance for the measured samples is $A_{max} = 0.95$.

Both the experiment and simulation results in Figure 4 show that the resonant wavelength for the metasurface varies linearly with the disk diameter. The measured results are slightly broader than the simulated response. This may be due to variances in the patch diameter and array periodicity, scattering from defects on the surface, as well as

the finite interrogation region in the experiment (in contrast to infinite array in the simulation).

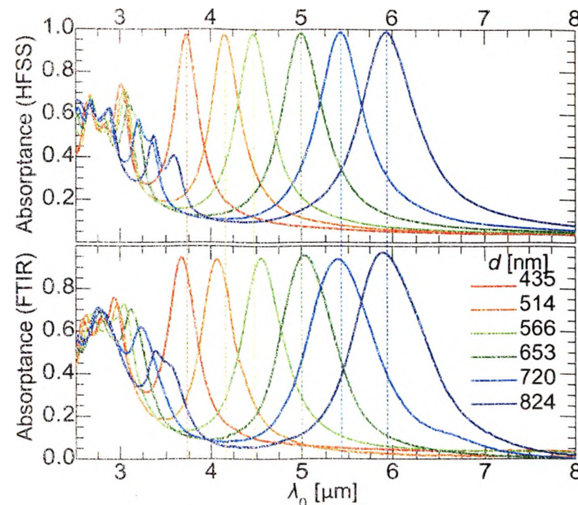

Figure 4. Comparison between simulated (dashed lines) and measured (solid lines) absorption spectra for different diameter disks.

Combined with the tunability of the disk diameter via the exposure dose, this linear variation provides a mechanism for hierarchically patterning complex metasurfaces. For example, a grayscale mask can be used to vary the single exposure, illumination intensity over the HCP microsphere array so that the metasurface response varies across a sample. The wavelength range can be adjusted beyond the MWIR by changing the thickness of the silicon insulator layer or by replacing silicon with a lower-index dielectric/semiconductor. The diameter of the disks is not sensitive to the diameter of the microspheres [15], so the periodicity can be adjusted by selecting different-diameter microspheres.

While possible to generate large single-crystal microsphere arrays [21], the results in Figure 4 are for a polycrystalline meta- surface. When the microspheres form the 2D HCP array, self-assembly is very similar to crystallization, and multiple nucleation sites lead to a polycrystalline 2D microstructure. The natural polycrystallinity of the microsphere arrays is transferred to the metasurface and can be seen in Figure 5(a), which shows crystal boundaries, point defects, and dislocations in the lattice. The effects of the microstructure are easily seen under illumination with bright white light. Diffraction causes each crystal domain in the metasurface to appear to be a different iridescent color as shown in Figure 5(b). This is further illustrated in a more controlled diffraction experiment. Figure 5(c) shows the diffraction pattern generated by the metasurface when illuminated focused to a spot size of 100 μm. Three orders are shown by a normally incident He–Ne laser beam (λ_0 = 632.8 nm) in Figure 5(c). A single-crystal HCP surface produces exactly six maxima in each diffraction order [21] so that Figure 5(c) indicates the presence of multiple crystal domains in the 100 μm interrogation area.

Figure 6 shows FTIR measurements from two regions of the metasurface generated with 17.5 mJ/cm^2 (d = 720 nm). As in Figure 4 reflection spectra was collected using an aperture size of 50 μm × 50 μm. The insets of Figure 6 show SEM images of the two regions, with artificial shading applied to highlight the crystal domains. The results show nearly identical spectra produced by a single-crystal area and a polycrystalline area, with only a slightly wider absorptance from the polycrystalline area.

The polycrystalline nature of the MPL-patterned metasurface is in contrast with top-down lithographically defined single-crystal metasurfaces. It also differs from the numerical model in Figure 4 simulating an infinite field of uniform patch arrays using a

Floquet modal expansion. At first, this result is surprising, especially given results studying truncation effects for single-crystal metasurfaces [22]. However, the HCP disk array metasurface has very little inter-element coupling. This can be seen in Figure 7,

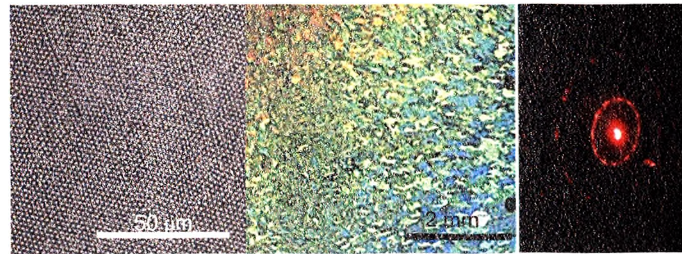

Figure 5. Polycrystalline metasurface with d = 720 nm and p = 1.93 µm. (a) SEM image showing grain boundaries and point defects; (b) far-field optical image showing colored diffraction from grains under white light illumination; and (c) diffraction pattern from a 5-mm^2 area of the metasurface illuminated with a He–Ne laser beam showing multiple discrete scattering sites.

which shows the HFSS-simulated near-field distribution at a metasurface defined by d = 653 nm at resonance. The electric field is tightly confined to the disk, particularly in the insulator region. This suggests that the effects of defects do not propagate beyond the single- unit cell and do not significantly affect the impedance of the metasurface.

In conclusion, we have demonstrated using the simple MPL technique the ability to create flexible, low-cost polycrystalline metasurfaces with near-unity absorptances over an MWIR band. Incident radiation of 93% to 98% at the design frequency can be captured with very good agreement between simulation and experiment. This permits rapid design and optimization of IR metasurfaces. The MPL technique has significant potential for large-area fabrication of IR metasurfaces, with the resonant wavelength

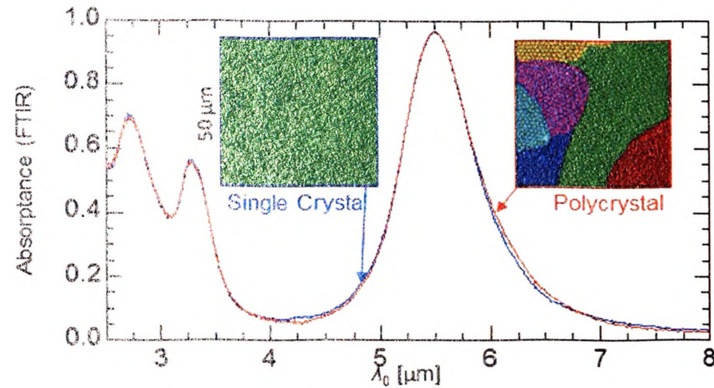

Figure 6. Measured absorption spectra for single and polycrystalline areas. The insets show SEM images of the two areas (both 50 μm × 50 μm) with the individual 2D crystal domains indicated by color.

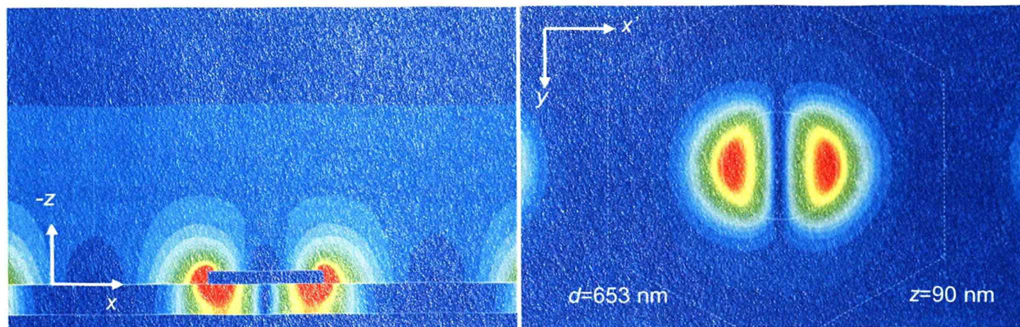

Figure 7. Simulated electric field for an infinitely large single-crystal metasurface with d = 653 nm at λ = 5.00 μm for TE illumination incident from 29.5°. (a) *xz* plane and (b) *xy* plane 240 nm (midplane) into the Si layer.

scaling with the exposure dose. This facilitates a hybrid top-down/bottom-up approach where different areas can be designed to have a different metasurface response. Finally, the hexagonal close-packed disk array is shown to be highly defect tolerant. This robustness allows the design to accommodate different metasurface microstructures.

REFERENCES

[1] N. I. Landy, S. Sajuyigbe, J. J. Mock, D. R. Smith, and W. J. Padilla, "Perfect Metamaterial Absorber," Phys. Rev. Lett. **100**, 207402 (2008).

[2] J. B. Pendry, "Negative refraction makes a perfect lens," Phys. Rev. Lett. 85, 3966 (2000).

[3] N. Liu, M. Mesch, T. Weiss, M. Hentschel, and H. Giessen, "Infrared perfect absorber and its application as plasmonic sensor," Nano Lett. 10, 2342 (2010).

[4] A. Tittl, P. Mai, R. Taubert, D. Dregely, N. Liu, and H. Giessen, "Palladium-based plasmonic perfect absorber in the visible wavelength range and its application to hydrogen sensing," Nano Lett. 11, 4366 (2011).

[5] K. Chen, R. Adato, and H. Altug, "Dual-Band Perfect Absorber for Infrared Spectroscopy," ACS Nano 6, 7998 (2012).

[6] C. Wu, B. Neuner III, J. John, A. Milder, B. Zollars, S. Savoy, and G. Shvets, "Dual-Band Perfect Absorber for Infrared Spectroscopy," J. Opt. 14, 024005 (2012).

[7] X. Liu, T. Tyler, T. Starr, A. F. Starr, N. M. Jokerst, and W. J. Padilla, "Taming the blackbody with infrared metamaterials as selective thermal emitters," Phys. Rev. Lett. 107, 4 (2011).

[8] Y. Zhang, L. Zhou, J. Q. Li, Q. J. Wang, and C. P. Huang, "Ultra-broadband and strongly enhanced diffraction with metasurfaces," Sci. Rep. 5, 10119 (2015).

[9] L. J. Guo, "Nanoimprint lithography: Methods and material requirements," Adv. Mater. 19, 495 (2007).

[10] I. B. Divliansky, A. Shishido, I.-C. Khoo, T. S. Mayer, D. Pena, S. Nishimura, C. D. Keating, and T. E. Mallouk, "Fabrication of two-dimensional photonic crystals using interference lithography and electrodeposition of CdSe," Appl. Phys. Lett. 79, 3392 (2001).

[11] J. C. Hulteen and R. P. Van Duyne, "Nanosphere lithography: A materials general fabrication process for periodic particle array surfaces," J. Vac. Sci. Technol. A 13, 1553 (1995).

[12] R. Walter, A. Tittl, A. Berrier, F. Sterl, T. Weiss, and H. Giessen, "Large-Area Low-Cost Tunable Plasmonic Perfect Absorber in the Near Infrared by Colloidal Etching Lithography," Adv. Opt. Mater. 3, 398 (2015).

[13] T. D. Dao, K. Chen, S. Ishii, A. Ohi, T. Nabatame, M. Kitajima, and T. Nagao, "Infrared Perfect Absorbers Fabricated by Colloidal Mask Etching of Al–Al_2O_3–Al Trilayers," ACS Photon. 2, 964 (2015).

[14] W. Wu, D. Dey, O. G. Memis, A. Katsnelson, and H. Mohseni, "A novel self-aligned and maskless process for formation of highly uniform arrays of nanoholes and nanopillars," Nano. Res. Lett. 3, 351 (2008).

[15] W. Wu, A. Katsnelson, O. G. Memis, and H. Mohseni, "A deep sub-wavelength process for the formation of highly uniform arrays of nanoholes and nanopillars," Nanotechnology, 18, 485302 (2007).

[16] A. Bonakdar, M. Rezaei, R. L. Brown, V. Fathipour, E. Dexheimer, S. J. Jang, and H. Mohseni, "Deep-UV microsphere projection lithography," Opt. Lett. 40, 2537 (2015).

[17] A. Bonakdar, M. Rezaei, E. Dexheimer, and H. Mohseni, "High-throughput realization of an infrared selective absorber/emitter by DUV microsphere projection lithography," Nanotechnology, 27, 035301 (2016).

[18] Y. C. Chang, S. M. Wang, H. C. Chung, C. B. Tseng, and S. H. Chang, "Observation of Absorption-Dominated Bonding Dark Plasmon Mode from Metal–Insulator–Metal Nanodisk Arrays Fabricated by Nanospherical-Lens Lithography," ACS Nano 6, 3390 (2012).

[19] Z. Szabo, J. Volk, E. Fulop, A. Deak, and I. Barsony, "Regular ZnO nanopillar arrays by nanosphere photolithography," Photon. Nanostruct. 11, 1 (2013).

[20] S. Cataldo, J. Zhao, F. Neubrech, B. Frank, C. Zhang, P. V. Braun, and H. Giessen, "Hole-mask colloidal nanolithography for large-area low-cost metamaterials and antenna-assisted surface-enhanced infrared absorption substrates," ACS Nano 6, 979 (2012).

[21] X. Meng and D. Qiu, "Gas-flow-induced reorientation to centimeter-sized two-dimensional colloidal single crystal of polystyrene particle," Langmuir 30, 3019 (2014).

[22] J. A. D'Archangel, E. Z. Tucker, and G. D. Boreman, "Spectral modification of array truncation effects in infrared frequency selective surfaces," Infrared Phys. Technol. 71, 285 (2015).

II. INFRARED METASURFACES CREATED WITH OFF-NORMAL INCIDENCE MICROSPHERE PHOTOLITHOGRAPHY

Chuang Qu and Edward C. Kinzel

Department of Mechanical and Aerospace Engineering,

Missouri University of Science and Technology, Rolla, MO 65409, USA

ABSTRACT

Fabricating metasurfaces over large areas at low costs remains a critical challenge to their practical implementation. This paper reports on the use of microsphere photolithography (MPL) to create infrared metasurfaces by changing the angle-of-incidence of the illumination to steer the photonic jet. The displacement of the photonic jet is shown to scale with the diameter of the microsphere while the exposure dose scales with the square of the microsphere diameter. This process is robust in the presence of local defects in the microsphere lattice. The paper demonstrates patterning split ring resonators and tripole based metasurfaces using MPL, which are fabricated and characterized with FTIR. The combination of bottom-up and top-down approaches in off-normal incidence microsphere photolithography technique provides cost-effective, flexible, and high-throughput fabrication of infrared metasurfaces.

Keywords: Nanolithography; Metamaterials; Nanostructure fabrication; Subwavelength structures, nanostructures.

Metasurfaces and Frequency Selective Surfaces (FSS) are composite structures that provide an engineered electromagnetic scattering response. They consist of

subwavelength antenna elements whose 2D geometry determines the ensemble properties. These surfaces have applications such as planar lenses [1], holograms [2], carpet cloaks [3], perfect absorbers [4], Surface-Enhanced Raman Spectroscopy (SERS) and Surface-Enhanced Infrared Absorption (SEIRA) templates [5]. The subwavelength nature of these devices requires nanoscale patterning at infrared and optical frequencies. Metasurfaces can be readily prototyped using direct-write techniques such as Electron-Beam Lithography (EBL) [2,5] or Focused Ion Beam (FIB) milling [6], however, these techniques are cost prohibitive for practical applications where the nanoscale features in the metasurface must be patterned over cm2 to m2 areas. The inability to fabricate metasurfaces over these length scales is the principal obstacle to the implementation of metasurfaces to practical engineering problems.

Conventional projection lithography is possible for IR/THz FSS with μm + feature sizes and has been demonstrated for patch type perfect absorbers in the MWIR [7]. However, this becomes very expensive on an area basis for more complicated nanoscale features due to the requirements for masks and steppers. Similar cost/reliability concerns exist for developing variants of Nanoimprint Lithography [8] when it is applied at large scales. Interference lithography can also create arrays of patches/disks [9] but requires precise alignment and is limited for creating sub-element nanoscale features. Another option is colloidal techniques based on the self-assembly of microspheres into a Hexagonal Close Packed (HCP) lattice. This includes Nanosphere Lithography (NSL) [10] where the microsphere array is used as a shadow mask during PVD evaporation or etching. The NSL technique can be used to create complicated patterns including functional IR resonators using directional evaporation [11]. However, in NSL the

microspheres are consumed in the process and the technique requires precise manipulation of the sample in high-vacuum. A different approach is to use the self-assembled microspheres as optical elements to focus light. This has been termed microsphere/nanosphere photolithography (MPL/NPL) [12, 13], and Nanoparticle Lens Lithography (NLL) [14]. In this technique, the microspheres are in contact with a photoresist layer and produce and focus incident light to a photonic jet [15] with FWHM width of $\lambda/3$. This is a result of both evanescent and propagating fields, which allows the subwavelength photonic jet to extend more than λ into the photoresist [16]. The MPL technique has previously been used for pattering metasurfaces/FSS [4, 13]. The resonator size and hence wavelength was shown to be dependent on the illumination dose providing a pathway to hierarchical patterning of metasurfaces. This differs slightly from the Microlens Projection Lithography approach developed by the Whitesides group [17] where the microspheres, embedded in an elastomeric membrane, are separated from the photoresist and used to image a far-field pattern onto the photoresist.

Mohseni et al. demonstrated steering the photonic jet around the unit cell by tilting the substrate under collimated radiation [18, 19] or by controlling the angular spectrum of the illumination using a Fourier mask [20]. Using Deep UV (248 nm) illumination, they were able to define sub 100 nm features [20], included the creation of both holes and posts using positive and negative tone resists, respectively. This approach was also used by Zhang et al. [19] to fabricate nanostructures for enhancing the emission from LEDs and previously by Guo et al. [21] for the ablation of 360 nm wide lines in a thin SbTe film using silica microspheres and off normal illumination using a KrF excimer laser.

The objective of this paper is to explore the off-normal incidence MPL pattering process for the fabrication of IR metasurfaces. The process is introduced and characterized with respect to both the exposure of the photoresist as well as lift-off. The microsphere size, exposure dosage and incident angle are mapped experimentally and through simulation. Finally, functional infrared metasurfaces featuring split-ring resonators and tripoles are fabricated using the technique. These metasurfaces are also characterized experimentally and compared to simulation. The results demonstrate the robustness of the process with respect to local disorder in the microsphere lattice and show ability to pattern a wide range of practical metasurfaces.

Figure 1 illustrates the general fabrication process for microsphere photolithography. The microspheres are self-assembled onto a photoresist film, forming a Hexagonal Close-Packed (HCP) lattice. Several different techniques have been developed for self-assembling the microspheres [22] including convective self-assembly and liquid interface assembly. After the spheres are self-assembled and any excess solvent is removed, the microspheres are illuminated with UV light at angle measured from the surface normal (θ, φ) shown in Figure 1(a). Each microsphere focuses the incident light to a photonic jet inside the photoresist layer. The development process removes the spheres as well as the photoresist from the exposed regions to reveal the desired pattern as shown in Figure 1(b). Patterns can be transferred to the substrate using standard techniques such as etching or lift-off. Lift-off is used in this paper to deposit metal patterns (Figure 1(c)).

Figure 2 shows results of frequency-domain finite element method simulation (ANSYS HFSS) of the off-axis exposure process. A Floquet modal expansion is used to

model an infinitely periodic hexagonal close packed array of polystyrene (n = 1.69) microspheres rests on a 480 nm thick layer of S1805 (n = 1.73) which is on top of a BK7 glass (n = 1.52) substrate. The microspheres are illuminated with a λ_0 = 365 nm (i-line) plane wave at $\varphi = 0$. Figures 2 (a-c) shows the normalized electric field energy distribution under $\theta = 20°$ for different sized microspheres on the xz plane as well as the midplane of the photoresist ($z = -240$ nm). In each case, the incident field is collected by the sphere and focused to a confined jet with FWHM $\sim\lambda_0/3$. The normalized electric field energy is plotted in Figure 2(d) for p = 3 μm spheres at the surface, midplane, and substrate interface of the photoresist (z = 0, −240, and −480 nm) under different angles of illumination. The intensity of the jet scales with $\sim p^2$ (the cross sectional capture area of the spheres). The FWHM diameter increases with the angle of incidence. The center of the photonic jet is offset from the center of the microsphere by a displacement, δ, which scales with θ. This relationship can be normalized with the sphere diameter so that δ/p is constant for a given θ. This displacement is almost independent of φ. The simulations agree with a first order paraxial model for the process where the focus of the microsphere shifts with angle of incidence $\delta = f \cdot \theta$, where the focal length f of a ball lens in air is given by $f = n \cdot p/[4(n-1)]$.

A set of two-step illumination experiment was performed to verify the simulation results. Microposit S1805 positive tone photoresist was spun to a thickness of 480 nm on a glass microscope slide. After softbaking of the photoresist, polystyrene microspheres (Polysciences, Inc.) are drop-coated (convective self-assembly) onto the photoresist film. The illumination angles are determined by two computer controlled rotation stages positioned under a stationary i-line flood exposure source (Bachur). The stages enable

continuous rotation of the polar angle $-90° < \theta < 90°$ and azimuthal angle $0 \leq \varphi < 360°$. For this experiment, the samples were exposed at polar angle θ, rotated to angle $-\theta$, and exposed a second time. After the exposures, the samples are immersed in MF 319 developer (Dow), followed by rinsing with deionized water and drying with compressed air, before hard baking. This generates two holes centered around the center of the microsphere.

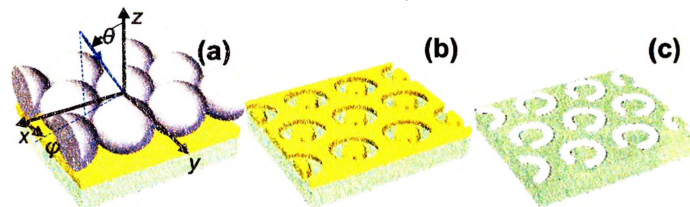

Figure 1. Illustration of fabrication procedure (a) directional illumination of self-assembled microspheres from polar angle, θ, and azimuthal angle, φ, (b) pattern revealed in photoresist after exposure and development (c) final metal split-ring resonators after lift-off.

Figure 3 shows SEM images of different hole-pairs generated with $p = 3$ μm spheres. The photoresist was cross sectioned using FIB milling (Helios Nanolab 600, FEI) through the center of each hole pair. Figure 3(a) shows partially exposed holes generated with two-step illumination at $\theta = \pm 10°$ at a dose of 1.44 mJ/cm^2 each time. The holes are separated by $2\delta = 670$ nm and do not completely penetrate the photoresist (diameter ~220 nm in diameter). Figure 3(b) shows the results of illuminating a different sample by $\theta = \pm 10°$ but with an increased dose of 3.6 mJ/cm^2. The center-to-center separation is the same but the exposed holes clear the photoresist with a diameter of 520

nm. When the illumination angle is increased to 25° off normal, the separation increases to $2\delta = 1530$ nm, and the diameter of the holes increases to 700 nm as shown in Figure 3(c). The increase in the hole diameter with larger angles of incidence agrees with the predictions of simulation shown in Figure 2(d).

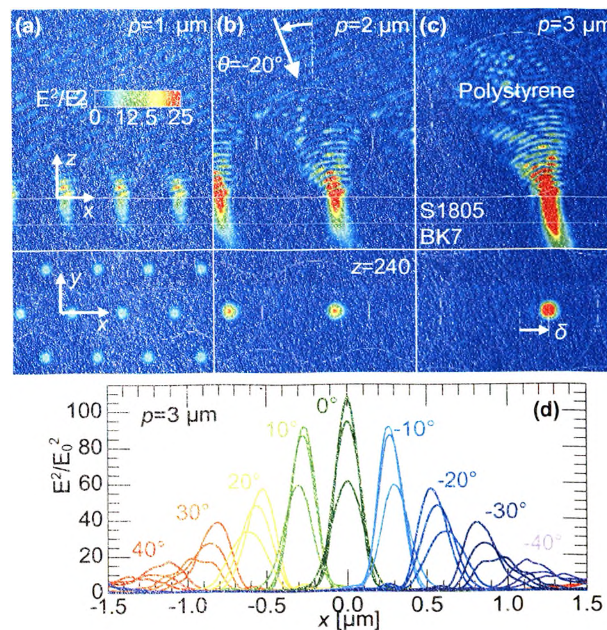

Figure 2. Simulation of off-axis exposure of different sized microspheres. Normalized electric field energy distribution (a) 1 μm (b) 2 μm and (c) 3 μm for -20° off normal illumination and (d) response at 0, 240 and 480 nm depths into the photoresist under different angles of incidence for 3 μm microspheres.

Evaporation and lift off were performed to study the effects of the exposure angle in a pattern transfer scenario. A 100 nm-thick aluminum film was deposited onto the patterned photoresist. The photoresist was then stripped using ultrasonication and Remover PG (MicroChem) to reveal metallic micro/nano features on the substrate. The

convective self- assembly procedure (drop-coating) creates polycrystalline arrays of microspheres with grains in different orientations. As a result, the azimuthal angle varies from grain to grain. Figure 4 shows disk pairs in different orientations. The disks are equidistant from the center of the spheres and their position depends on the location of the spheres and polar angle but is independent of the azimuthal angle. This agrees with simulation and allows the creation of detailed patterns without needing to align the crystal orientation to the illumination.

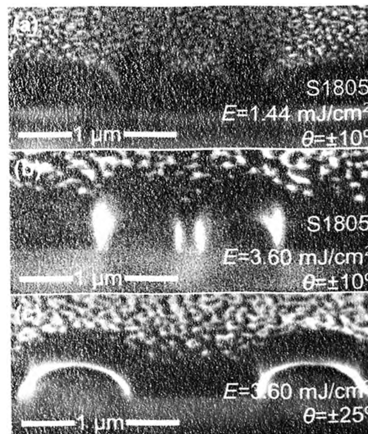

Figure 3. SEM images taken from 52° of hole-pairs after FIB cross sectioning (a) 1.44 mJ/cm^2, ±10°; (b) 3.6 mJ/cm^2, ±10°; (c) 3.6 mJ/cm^2, ±25°. Au/Pd was sputtered onto the photoresist prior to imaging to avoid charging.

Figure 5 plots the measured displacement, δ, of the disk pairs from the center of the microspheres produced with illumination from different polar angles. Both p = 2 and 3 μm microspheres were used and the displacement scales linearly with the microsphere diameter and the illumination angle. The dose affects the size of the disk but does not

change the offset. The error bars in the Figure represent the variation in the separation over a 100 μm × 100 μm area. In this experiment angles less than $\theta = 10°$ resulted in the disks merging together. The dashed lines in Figure 5 show the center of the photonic jet predicted by the HFSS simulation (Figure 2) at the top surface of the photoresist and the photoresist/glass interface.

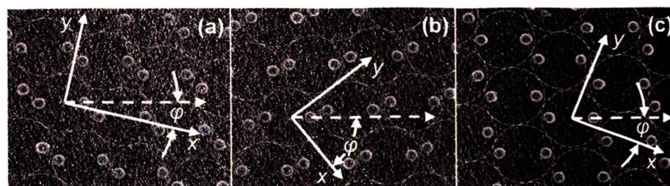

Figure 4. (a)-(c) SEM images of disks pairs (E=7.2 mJ/cm^2, θ=±35°, p=3 μm) after lift-off (a) φ=13°, (b) φ=52°, and (c) φ=22° resulting from different orientations of the microsphere lattice relative to the illumination directions.

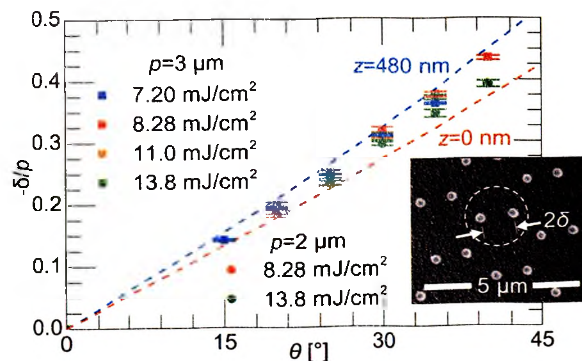

Figure 5. Measured disk displacement normalized to sphere diameter for deposited disks produced with different incident angles. Dashed lines show simulated displacement at the top and bottom of the photoresist.

Figures 4 and 5 show the robustness of the MPL process. Structures will take on the HCP lattice of the microsphere array including the microstructure resulting from the self-assembly process. The spherical coordinates of the illumination system map to polar coordinates in the unit cell; the azimuthal angle does not change and the polar angle determines the radial displacement with a nearly linear mapping between $\theta = 0$ and 45° corresponding to the center and edge of the unit cell. The feature size scales with the exposure dose [4].

IR metasurfaces can be designed for these constraints. To explore this, we used the technique to pattern two different functional devices. Figure 6 shows results from an array of Split Ring Resonators (SRR). These are a widely studied metamaterial element because of the ability of the SRR to create an artificial magnetic response as well as sensing applications. The fundamental resonance has a half-wave current response in the bent wire elements providing an inductive response. The electric field is concentrated in the gap region which enhances the capacitance. This leads to a dipole response parallel to the gap, so that the fundamental resonance will be excited when the incident E-field is polarized across the gap.

The SRRs in Figure 6 were created by spin-coating 480 nm of S1805 onto a glass microscope slide. Microspheres, $p = 3$ μm, were drop-coated onto the photoresist. This leads to cm^2 areas with single crystals on the order of 300 μm. The microsphere array was illuminated from $\theta = 30°$. From Figure 5, this corresponds to a diameter of 1.8 μm (2δ). A second computer controlled stage was use to rotate φ from 0 to 345° in $\Delta\varphi = 15°$ steps. At each step the sample was exposed using a fluence of $E = 7.2$ mJ/cm^2. After development and hardbaking, lift-off was used to transfer 100 nm thick aluminum

patterns to the substrate. The width of the features shown in the inset of Figure 6 is 750 nm. The dimensions of the SRR were selected to place the primary resonant mode at the same wavelength silica absorption peak due to phonon mode coupling [23].

The reflectance spectra of the metasurface were measured using Fourier Transform Infrared (FTIR) spectrometer (Perkin-Elmer micro-FTIR). The SRRs have a distinct linearly polarized response which is dependent by the orientation of the gap. The gap's angular position is determined in the specimen rather than the lattice coordinate system. Figure 6 shows the measured reflectance of the SRRs for radiation polarized parallel to the gap in red and the perpendicular to the gap in blue. The dashed lines show the simulated response of the metasurface from HFSS. In the simulation, the glass microscope slide is modeled as SiO_2. The properties of both SiO_2 and Al are taken from IR ellipsometry. The insets show simulated normal E-field distributions at the surface of the SRR for the three lowest energy modes (λ = 7.8, 4.7, and 3.8 μm) with arrows indicating the direction of current flow. There is reasonable agreement between the experimental and simulated reflectance spectra, with the discrepancy attributable to uncertainty in the substrate dielectric properties.

Figure 7 shows results for a Metal-Insulator-Metal tripole based metasurface absorber/emitter patterned with MPL. A tripole is a common Frequency-Selective Surface (FSS) element used at microwave frequencies [24] and is polarization independent because the two orthogonal modes share common current paths [25]. The presence of the ground plane prevents any transmission, so that radiation not reflected by the surface is absorbed. From Kirchhoff's law the absorptance is equal to the emittance, so the device acts as a selective emitter with applications for controlling thermal

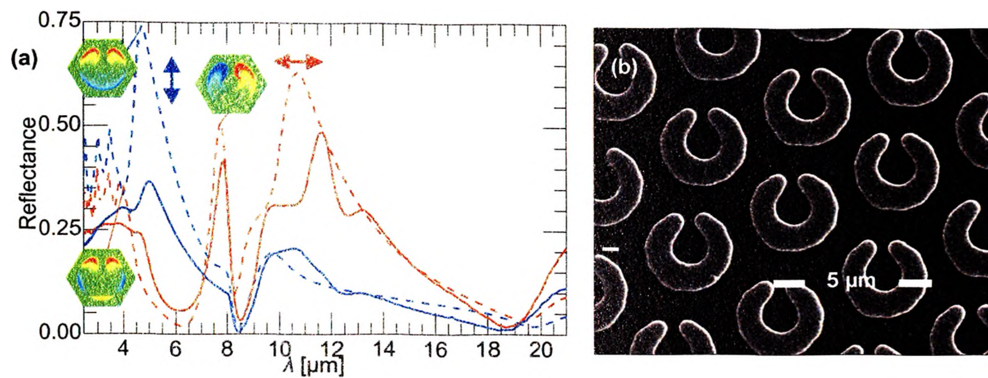

Figure 6. Reflectance spectra of split ring resonator sample shown in the inset (SEM image). Red and blue lines represent the response for incident radiation polarized parallel and perpendicular to the SRR gap. The solid and dashed lines show FTIR and simulation results, respectively.

transport. The tripoles are separated from a 200 nm thick aluminum ground plane by a 250 nm silicon dioxide film. As with the SRRs, 3 μm microspheres were used. The sample was exposed at $\theta = 15°$, 20°, and 25° at three different relative azimuthal angles, $\varphi = 0°$, 120° and 240° (9 steps) with a fluence of $E = 7.2$ mJ/cm2. Figure 7 shows agreement between the unpolarized reflectance measured with FTIR and HFSS simulation.

The tripoles show a single resonance at $\lambda = 5.5$ μm with an absorptance greater than 0.85. This can be tuned by adjusting the illumination angles to increase or decrease the tripole arm length. The exposure can also be adjusted to control the width of the patterns. There is relatively little coupling between adjacent tripoles so they are also not affected by the lattice orientation. It is important to note that the photonic jet was not significantly affected by the presence of the ground plane, expanding the range of devices that can be patterned with this method.

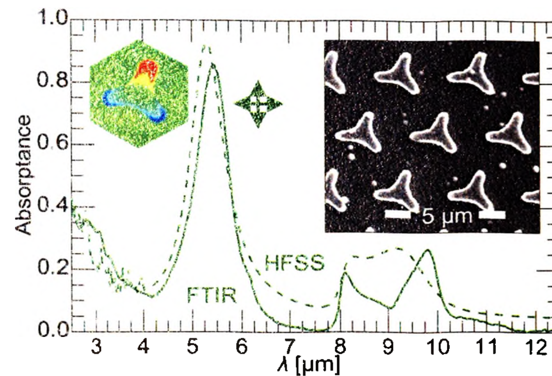

Figure 7. Absorption spectra of tripole FSS shown in the inset (SEM image). The solid and dashed lines show FTIR and simulation results, respectively.

In conclusion, microsphere photolithography is shown to be a versatile tool for patterning IR metasurfaces. The combination of bottom-up self-assembly of microsphere array and top-down, direct-write exposure allows inexpensive patterning of detailed elements over large areas at low-cost. Control of the illumination angle-of-incidence allows the photonic jet to be precisely steered around the unit cell defined by the microsphere. The displacement of the photonic jet from the center of the microsphere is shown to be independent of the orientation of the microsphere lattice and scales with the microsphere diameter. The width of the exposed region scales with the exposure dose and can be further reduced to facilitate patterning metasurfaces for SWIR or visible wavelengths. The ability to pattern structures with a ground-plane is significant for expanding the types of metasurfaces that can be patterned with the technique and opens more possibilities for spectral engineering and field concentration for sensing applications. Finally, the agreement between idealized simulations of infinitely periodic structures with experimental results for both the MPL process and the metasurfaces

illustrates the robustness of the process in the presence of lattice defects and other irregularities from the self-assembly process.

REFERENCES

[1] J. B. Pendry, "Negative refraction makes a perfect lens," Phys. Rev. Lett. 85(18), 3966–3969 (2000).

[2] L. Wang, S. Kruk, H. Tang, T. Li, I. Kravchenko, D. N. Neshev, and Y. S. Kivshar, "Grayscale transparent metasurface holograms," Optica 3(12), 1504–1505 (2016).

[3] X. Ni, Z. J. Wong, M. Mrejen, Y. Wang, and X. Zhang, "An ultrathin invisibility skin cloak for visible light," Science 349(6254), 1310–1314 (2015).

[4] C. Qu and E. C. Kinzel, "Polycrystalline metasurface perfect absorbers fabricated using microsphere photolithography," Opt. Lett. 41(15), 3399–3402 (2016).

[5] B. Lahiri, A. Z. Khokhar, R. M. De La Rue, S. G. McMeekin, and N. P. Johnson, "Asymmetric split ring resonators for optical sensing of organic materials," Opt. Express 17(2), 1107–1115 (2009).

[6] Y. Zhang, L. Zhou, J. Q. Li, Q. J. Wang, and C. P. Huang, "Ultra-broadband and strongly enhanced diffraction with metasurfaces," Sci. Rep. 5(1), 10119 (2015).

[7] J. A. D'Archangel, D. J. Shelton, R. Hudgins, M. K. Poutous, and G. D. Boreman, "Large area infrared frequency selective surface with dimensions reproducible by optical lithography," J. Vac. Sci. Technol. B 32(5), 051807 (2014).

[8] L. J. Guo, "Nanoimprint lithography: methods and material requirements," Adv. Mater. 19(4), 495–513 (2007).

[9] I. B. Divliansky, A. Shishido, I.-C. Khoo, T. S. Mayer, D. Pena, S. Nishimura, C. D. Keating, and T. E. Mallouk, "Fabrication of two-dimensional photonic crystals using interference lithography and electrodeposition of CdSe," Appl. Phys. Lett. 79(21), 3392–3394 (2001).

[10] J. C. Hulteen and R. P. Van Duyne, "Nanosphere lithography: a materials general fabrication process for periodic particle array surfaces," J. Vac. Sci. Technol. A 13(3), 1553–1558 (1995).

[11] M. C. Gwinner, E. Koroknay, L. Fu, P. Patoka, W. Kandulski, M. Giersig, and H. Giessen, "Periodic Large-Area Metallic Split-Ring Resonator Metamaterial Fabrication Based on Shadow Nanosphere Lithography," Small 5(3), 400–406 (2009).

[12] W. Wu, D. Dey, O. G. Memis, A. Katsnelson, and H. Mohseni, "Fabrication of large area periodic nanostructures using nanosphere photolithography," Nanoscale Res. Lett. 3(10), 351–354 (2008).

[13] Z. Szabó, J. Volk, E. Fulop, A. Deak, and I. Barsony, "Regular ZnO nanopillar arrays by nanosphere photolithography," Phot. Nano. Fund. Appl. 11(1), 1–7 (2013).

[14] Y. C. Chang, S. M. Wang, H. C. Chung, C. B. Tseng, and S. H. Chang, "Observation of absorption-dominated bonding dark plasmon mode from metal-insulator-metal nanodisk arrays fabricated by nanospherical-lens lithography," ACS Nano 6(4), 3390–3396 (2012).

[15] X. Li, Z. Chen, A. Taflove, and V. Backman, "Optical analysis of nanoparticles via enhanced backscattering facilitated by 3-D photonic nanojets," Opt. Express 13(2), 526–533 (2005).

[16] M. S. Kim, T. Scharf, S. Mühlig, M. Fruhnert, C. Rockstuhl, R. Bitterli, W. Noell, R. Voelkel, and H. P. Herzig, "Refraction limit of miniaturized optical systems: a ball-lens example," Opt. Express 24(7), 6996–7005 (2016).

[17] M. H. Wu, C. Park, and G. M. Whitesides, "Generation of submicrometer structures by photolithography using arrays of spherical microlenses," J. Colloid Interface Sci. 265(2), 304–309 (2003).

[18] A. Bonakdar, S. J. Jang, and H. Mohseni, "Novel high-throughput and maskless photolithography to fabricate plasmonic molecules," J. Vac. Sci. Technol. B 32(2), 020604 (2014).

[19] Y. Zhang, T. Wei, Z. Xiong, L. Shang, Y. Tian, Y. Zhao, P. Zhou, J. Wang, and J. Li, "Enhanced optical power of GaN-based light-emitting diode with compound photonic crystals by multiple-exposure nanosphere-lens lithography," Appl. Phys. Lett. 105(1), 013108 (2014).

[20] A. Bonakdar, M. Rezaei, R. L. Brown, V. Fathipour, E. Dexheimer, S. J. Jang, and H. Mohseni, "Deep-UV microsphere projection lithography," Opt. Lett. 40(11), 2537–2540 (2015).

[21] W. Guo, Z. B. Wang, L. Li, D. J. Whitehead, B. S. Luk'yanchuk, and Z. Liu, "Near-field laser parallel nanofabrication of arbitrary-shaped patterns," Appl. Phys. Lett. 90(24), 243101 (2007).

[22] X. Meng and D. Qiu, "Gas-flow-induced reorientation to centimeter-sized two-dimensional colloidal single crystal of polystyrene particle," Langmuir 30(11), 3019–3023 (2014).

[23] D. J. Shelton, I. Brener, J. C. Ginn, M. B. Sinclair, D. W. Peters, K. R. Coffey, and G. D. Boreman, "Strong coupling between nanoscale metamaterials and phonons," Nano Lett. 11(5), 2104–2108 (2011).

[24] B. A. Munk, Frequency Selective Surfaces Theory and Design (John Wiley & Sons, 2000).

[25] J. Ginn, D. Shelton, P. Krenz, B. Lail, and G. Boreman, "Polarized infrared emission using frequency selective surfaces," Opt. Express 18(5), 4557–4563 (2010).

III. THERMAL RADIATION FROM MICROSPHERE PHOTOLITHOGRAPHY PATTERNED METASURFACES

Chuang Qu and Edward C. Kinzel

Department of Mechanical and Aerospace Engineering,

Missouri University of Science and Technology, Rolla, MO 65409, USA

ABSTRACT

Frequency-Selective Surfaces (FSS) type metasurfaces consist of periodic arrays of antenna elements. They can be scaled from microwave frequencies to the infrared wavelengths where they allow the scattering response to be engineered. This includes the spectral absorptance/emittance. At IR wavelengths, the features sizes of the metasurface are sub-micron which poses manufacturing issues for the meter squared scales required for most heat transfer applications. In this paper, we investigate the use of Microsphere Photolithography for creating spectrally selective metasurfaces. This approach uses a self-assembled array of microspheres as a lens array to focus a lattice of photonic jets into photoresist. These can be used with lift-off to create metal-insulator-metal (MIM) or even five-layer of resonant structures. We study the design constraints and synthesize a broadband emitter in the mid-infrared. The spectral absorptance is measured experimentally using FTIR. The structures are then tested at moderate temperatures to demonstrate the ability to affect surface temperature/heat flux in practical applications.

Broadband absorbing/emitting metamaterials have significant potential to spectrally optimize the radiative response of structures. This has applications for energy

harvesting applications as solar cells [1] and thermophotovoltiacs as well as thermal imaging [2] and chemical sensing. Basic metasurface elements produce a single resonance. This can be used to achieve an impedance match to free space and produce perfect absorption, typically involving a metal-insulator-metal (MIM) configuration. Broadband-absorption from a metasurface can be achieved by incorporating different features into a larger unit cell. This can be accomplished layering different features or by tessellating multiple features in-plane. Crosses [3], squares [4], L shapes [5] as well as trapezoid [6] arrays have been proposed for spectral engineering at visible and infrared wavelengths. An alternative approach is to stack multiple MIM layers in a stacked design with two different dielectric spacers [7]. Dayal and Ramakrishna studied on metasurfaces comprising of metallic circular discs separated by dielectric films and producing two distinct absorption peaks [8-9].

Micro/nanofabrication presents paramount challenge for producing FSS metasurfaces operating at infrared/visible frequencies. Feature sizes are often sub-micron and micro/nano fabrication techniques such as electron-beam lithography (EBL) [3-6], focal ion beam (FIB) milling are commonly employed. Conventional projection photolithography [7] can also be used for longer wavelength devices. Charged particle beam techniques (e.g. EBL) are cost-prohibitive and time-consuming, especially for application relevant large areas. Alternative micro/nano fabrication techniques are required to realize the potential impact of metasurfaces. Several promising techniques involve self-assembly of microspheres, including Nanosphere Lithography (NSL) [10] and Microsphere Photolithography (MPL) [11]. The distinction between these two techniques is that in NSL, the self-assembled Hexagonal Close-Packed (HCP)

microsphere arrays act as a shadow mask while in MPL they are used as an optical element to focus flood illuminated light to sub-diffraction limited photonic jets inside a layer of photoresist. The MPL approach has advantages in terms of versatility. For example, the photonic jet can be steered around the unit cell by controlling the angle of incidence. We previously studied MPL for the fabrication of simple FSS metasurfaces with spectral selectivity in the MWIR [12] with resonant wavelength dependent on the exposure dose.

This paper work aims to use the microsphere photolithography approach to create broadband metasurface absorbers/emitters at sufficient scales to affect radiant heat transfer. A multilayer (two cavity) metasurface design is fabricated and hierarchically patterned to demonstrate macroscale emissivity control as a result of micro/nanoscale features.

Figure 1 illustrates MPL approach for patterning metasurfaces. Pattern transfer is accomplished via lift-off. The structures presented in this work were prepared by first depositing 150 nm of aluminum onto glass microscope slide substrates using electron-beam evaporation (CHA). Without breaking vacuum, h_1=180 nm of silicon was evaporated on top of the aluminum film. The samples were removed from the chamber and spin coated with HDMS adhesion promoter followed by a 480 nm thick film of positive tone photoresist (S1805, Shipley). After soft baking of photoresist, polystyrene microsphere (Polyscience) with p= 2 μm (nominal) in diameter was self-assembled on the photoresist by drop coating. Following deposition of the microsphere lattice, the entire sample was flood exposed using i-line illumination. The exposure duration was varied to control the diameter d of the exposed features on different samples. After

exposure, the samples were immersed in MF 319 developer (Microposit) for 60 s. This removed the exposed areas of photoresist along with the polystyrene microspheres, to reveal an HCP array of holes in the photoresist.

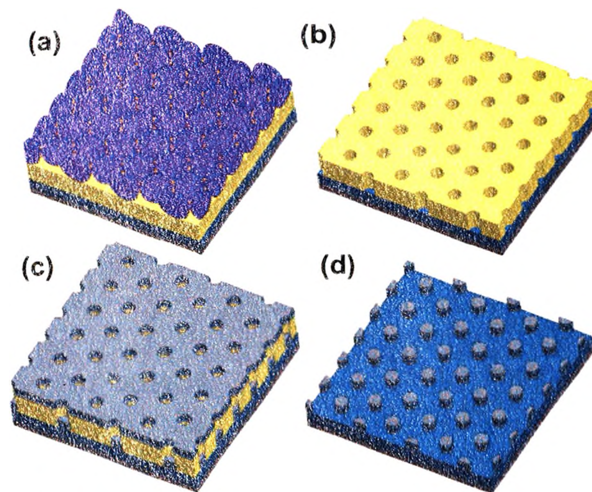

Figure 1. Fabrication of metasurface with MIMIM structure using Microsphere Photolithography (a) microspheres applied on photoresist on Si/Al films (b) holes revealed after photolithography and development (c) deposition of Al/Si/Al (d) final MIMIM structure with Al/Si/Al disk stack on Si/Al.

Following hard baking, three thin-film layers, (aluminum 100 nm, h_2=silicon 80 nm, aluminum 80 nm) were deposited sequentially onto the samples to create a MIMIM structure. Only the first 100 nm thick layer of aluminum was deposited on some samples to create MIM structures. Following deposition, the remaining photoresist was removed in ultrasonic bath of Remover PG (MicroChem) to reveal the uniform disk arrays depicted in Figure 1(d).

The principle design variables for the metasurfaces are the periodicity, p, diameter d, and two dielectric cavity heights, h_1 and h_2. The periodicity is determined by the microsphere diameter and the disk diameter can be adjusted by changing the exposure dose. The dielectric heights are specified during deposition. Because of the continuous aluminum ground plane the total transmittance is negligible. Therefore the absorptance is given by α=1-ρ, where ρ denotes the reflectance. From Kirchhoff's law, the angle dependent spectral absorptance is equal to the emittance, ε. The reflectance can be experimentally measured using a FTIR spectrometer (Thermo Nicolet Nexus 670) and IR microscope (Nicolet Continuum). The instrument is equipped with a liquid nitrogen cooled Mercury Cadmium Telluride (MCT) detector and KBr beam splitter, and purged with nitrogen gas.

Figure 2 shows representative SEM images of the fabricated samples. Figure 3 shows comparison of experimental results between MIMIM and MIM samples. Near unity of absorption are observed for all samples. The red curves represent absorption spectra for MIMIM samples, and blue ones are for MIM samples. At small diameters of disks such as d=566 nm shown in Figure 3(a), two curves results for the MIM and MIMIM structures are almost identical with a single resonance at λ=4.8 μm. However, for larger diameter disks created with longer exposure doses, the MIMIM samples show an additional higher energy peak corresponding to the 2nd resonance for the upper resonator. The shorter wavelength is due to a slightly conical shape of the disk (see Figure 2) as well as the shorter dielectric thickness h_2.

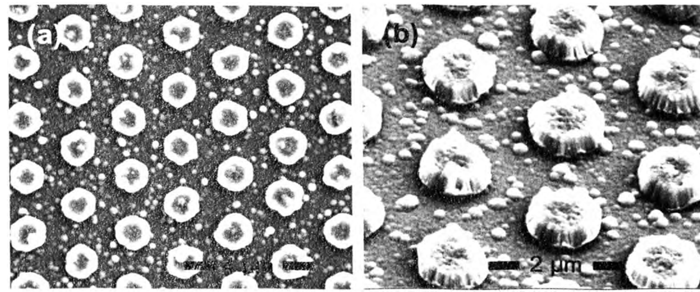

Figure 2. SEM image of the MIMIM disc arrays (a) top view (b) 45° tilt during imaging.

The addition of the resonance significantly increases the bandwidth of absorber with negligible increase in fabrication cost. Figure 3(b-d) shows that the presence of the second resonator minimally affects the first resonance. For example, the d=894 nm sample has a resonance λ=7.5 μm while the second resonance is centered at λ=5.6 μm, leading to absorption α>0.6 over the λ=5-8.2 μm interval. For thicker layers of photoresist it would be possible to incorporate additional resonators. In addition, the dielectrics can be different materials with different indices of refraction.

Hierarchical patterns are found widely in the natural world and are often imitated for biologically inspired designs such as such as superhydrophobic (lotus leaves), strong adhesion (gecko feet), and color display (butterfly wings) surfaces. In these cases the geometry the key parameters are the periodicity and the area [13]. A key advantage of the MPL approach is the ability to hierarchically pattern metasurfaces over large areas, combining bottom-up and top-down paradigms. For example the exposure dose can be modulated over large areas using a gray-scale mask. Because the feature size is dose dependent, the resonant wavelength can be varied over the metasurface. This is useful for applications relying on the phase of the reflected radiation (e.g. Fresnel zone plates

and holograms) as well as tuning the emissivity spatially, ultimately affording the ability to engineer the thermal response in radiation heat transfer dominated environments such as space.

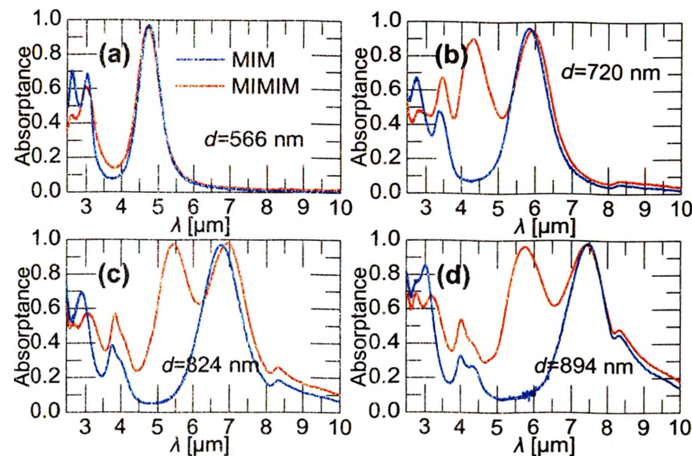

Figure 3. Absorption spectra of MIMIM (black) & MIM (red) samples with disk diameters of (a) 566 nm (b) 720 nm (c) 824 nm (d) 894 nm.

Figure 4 illustrates this concept. After depositing a ground plane, dielectric layer, and photoresist, microspheres were self assembled over a 40 mm diameter region of the substrate. A mask was used to expose the university's logo and the surroundings with 60 mJ/cm^2 and 144 mJ/cm^2, respectively.

After exposure the same deposition/lift-off procedure as Figures 2 and 3 was followed to reveal the final pattern. The sample was uniformly heated up on hot plate and imaged using thermal infrared camera (FLIR T-420). The difference in the spectrally integrated emittance of the university logo generates an apparent temperature difference for the camera.

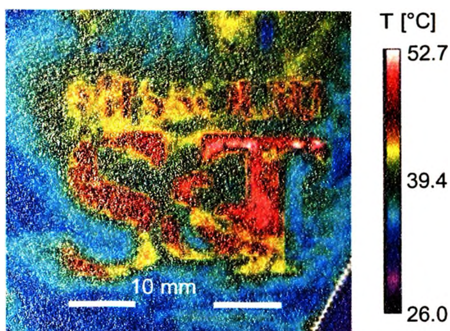

Figure 4. Thermal image of MIM-structure metasurface fabricated by MPL hierarchical patterning.

Figure 5 shows the FTIR measured absorptance for the two regions of the sample. The thermal camera is sensitive to radiation in the λ=7.5-13 μm band. Over this interval the spectrally integrated emittance for the logo is 0.28 while the background is 0.12. The sample successfully controls local temperature and local radiation heat transfer performance on the metasurface.

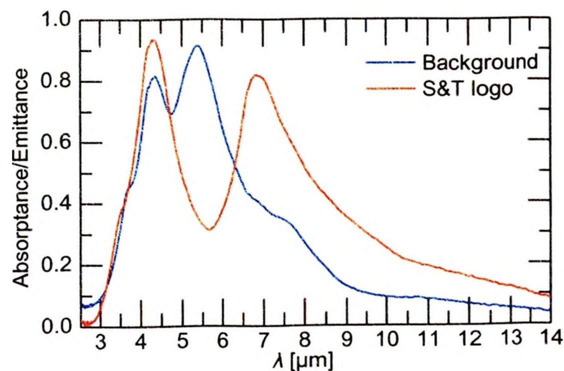

Figure 5. Absorptance/Emittance spectra of S&T logo area (blue) and background area (red).

In this paper, we have explored Microsphere Photolithography technique for fabrication of multicavity MIMIM broadband metasurface absorbers in the thermal infrared spectral region. The ability to hierarchically pattern metasurfaces using MPL was also proposed and demonstrated using exposure with a grayscale mask. These approaches facilitate heat transfer applications because of the ability to pattern large areas at relatively low cost. For the simple disk metasurface the resonant wavelength is shown to be determined by exposure dose. This resonant wavelength is minimally affected by the presence of additional resonators. Applications of the MPL technique include energy harvesting, thermal imaging, and thermal management.

REFERENCES

[1] D. Li, D. Wan, X. Zhu, Y. Wang, Z. Han, S. Han, Y. Shan, and F. Huang, "Broadband antireflection TiO_2–SiO_2 stack coatings with refractive-index-grade structure and their applications to Cu(In,Ga)Se_2 solar cells," Sol. Energy Mater. Sol. Cells **130**, 505 (2014).

[2] J.K. Hyun, C.W. Ahn, W.C. Kim, T.H. Kim, M.S. Hyun, W.O. Lee, H.Y. Kim, and J.H. Park, "Broadband enhancement of infrared absorption in microbolometers using Ag nanocrystals," Appl. Phys. Lett. 107, 1 (2015).

[3] W. Ma, Y. Wen, and X. Yu, "Broadband metamaterial absorber at mid-infrared using multiplexed cross resonators," Opt. Express 21, 30724 (2013).

[4] J. Hendrickson, J. Guo, B. Zhang, W. Buchwald, and R. Soref, "Wideband perfect light absorber at midwave infrared using multiplexed metal structures," Opt. Lett. 37, 371 (2012).

[5] Y. Bai, L. Zhao, D. Ju, Y. Jiang, and L. Liu, "Wide-angle, polarization-independent and dual-band infrared perfect absorber based on L-shaped metamaterial," Opt. Express 23, 8670 (2015).

[6] K. Aydin, V.E. Ferry, R.M. Briggs, and H. A. Atwater, "Broadband polarization-independent resonant light absorption using ultrathin plasmonic super absorbers," Nat. Commun. 2, 517 (2011).

[7] N. Zhang, P.H. Zhou, D.M. Cheng, X.L. Weng, J.L. Xie, and L.J. Deng, "Dual-band absorption of mid-infrared metamaterial absorber based on distinct dielectric spacing layers," Opt. Lett. 38, 1125 (2013).

[8] D. Govind and S.A. Ramakrishna, "Design of multi-band metamaterial perfect absorbers with stacked metal–dielectric disks," J. Opt. **15**, 55106 (2013).

[9] G. Dayal and S.A. Ramakrishna. "Multipolar localized resonances for multi-band metamaterial perfect absorbers," J. Opt. **16**, 94016 (2014).

[10] J. C. Hulteen and R. P. Van Duyne, "Nanosphere lithography: A materials general fabrication process for periodic particle array surfaces," J. Vac. Sci. Technol. A **13**, 1553 (1995).

[11] W. Wu, A. Katsnelson, O. G. Memis, and H. Mohseni, "A deep sub-wavelength process for the formation of highly uniform arrays of nanoholes and nanopillars," Nanotechnology **18**, 485302 (2007).

[12] C. Qu and E.C. Kinzel, "Polycrystalline metasurface perfect absorbers fabricated using microsphere photolithography," Opt. Lett. **41**, 3399 (2016).

[13] A. K. Geim, S. V Dubonos, I. V Grigorieva, K. S. Novoselov, A. A. Zhukov, and S. Y. Shapoval, "Microfabricated adhesive mimicking gecko foot-hair," Nat. Mater. **2**, 461 (2003).

IV. FABRICATION OF INFRARED BROADBAND POLARIZED EMITTING METASURFACES USING MICROSPHERE PHOTOLITHOGRAPHY

Chuang Qu, Chen Zhu, Edward C. Kinzel

Department of Mechanical and Aerospace Engineering,

Missouri University of Science and Technology, Rolla, MO 65409, USA

ABSTRACT

This paper describes the low-cost, scalable fabrication of 2D metasurface LWIR broadband polarized emitter/absorber. A Frequency Selective Surface (FSS) type design consisting of dipole antenna elements is designed for resonance in the 7.5- 13 μm band. Frequency-domain Finite Element Method (FEM) is used to optimize the design with ellipsometrically measured properties. The design is synthesized to be broadband by creating a multiple cavities and by hybridizing the dipole modes with phonon resonances in a germanium/silica dielectric which separates metallic elements from a continuous ground plane. While IR metasurfaces can be readily realized using direct-write nanofabrication techniques such as E-Beam Lithography, or Focus-Ion Beam milling, or two-photon lithography, these technologies are cost- prohibitive for large areas. This paper explores the Microsphere Photolithography (MPL) technique to fabricate these devices. MPL uses arrays of self-assembled microspheres as optical elements, with each sphere focusing flood illumination to a sub-wavelength photonic jet in the photoresist. Because the illumination can be controlled over larger scales (several μm resolutions) using a conventional mask, the technique facilitates very low cost hierarchical patterning with sub-400 nm feature sizes. The paper demonstrates the fabrication of metasurfaces over 15 cm^2 and are measured using FTIR and imaged with a thermal camera.

Keywords: microsphere photolithography, radiation heat transfer, infrared, polarized emitting metasurfaces

1. INTRODUCTION

Frequency-Selective Surface (FSS) type metasurfaces have significant potential for engineering scattering properties in the infrared. While these are readily prototyped using conventional direct-write nanofabrication tools such as E-beam lithography (EBL) and focused ion beam (FIB) milling, these techniques are cost prohibitive over large areas [1]. This is significant because the applications for these devices such as thermophotovoltaics, daytime radiative cooling, and Surface Enhanced Infrared Absorption (SEIRA) will need to be patterned inexpensively over large areas. Frequency-selective-surface type of metasurface with polarization-dependent performance has been demonstrated in previous papers as mid-infrared filters [2] and polarization-selective emitters/absorbers [3-4].

Microsphere Photolithography (MPL) uses self-assembled microsphere arrays as an optical element [5]. The microspheres form Hexagonal Close-Packed (HCP) lattices on the photoresist. The microspheres focus collimated flood illumination to an array of sub-wavelength high-aspect ratio photonic jets [6]. These photonic jets have the same periodicity as the microsphere array, which in many practical cases is polycrystalline. The photonic jets can also be steered around the microsphere unit cell by controlling the angular spectrum of the flood illumination. This can be done practically by tilting the sample during exposure [7]. After exposure and development of the photoresist, pattern transfer can be carried out using conventional techniques such as lift-off, etching or

electrodeposition. In this paper, lift-off is used to deposit both dielectrics and metal elements through the exposed regions. Off-angle illumination provides significant flexibility and the intensity of the illumination can be controlled with a grayscale mask to facilitate hierarchical patterning [8, 10].

This paper presents the development of the MPL process for IR metasurfaces. MPL provides low-coat and scalable fabrication of IR metasurfaces. The technique also imposes constraints on the design. The periodicity is hexagonal close packed a width spacing determined by the microsphere diameters and is broken up to a polycrystalline microstructure. The surface is polycrystalline which prevents element alignment with the HCP unit cell orientation [9]. It also limits the effectiveness of designs with large inter-element coupling.

To explore the process, a broadband polarized metasurface is synthesized using ANSYS HFSS. This consists of a HCP array of dipole resonators separated from a ground plane by continuous layers of germanium and silica for broadening the bandwidth of the metasurface. The dipole resonance couples to a phonon mode in the silica which adds a third resonance. The dimensions of the metasurface are optimized to maximize the absorption across the 7.5-13 μm band for radiation parallel to the dipoles and minimize absorption for cross-polarized radiation. The significance of this work is the ability to achieve spectral engineering over large areas and the paper seeks to define a framework for similar metasurfaces to provide an engineered scattering response with respect to wavelength, polarization, and angle of incidence. The process of scaling the up the MPL technique is discussed along with the sensitivities to factors such as the sphere self-assembly procedure and hierarchical exposure.

2. EXPERIMENT

Figure 1 exhibits the dipole feature designed in (a) and the patterning of hexagonal distributed metallic dipole features with MPL approach in (a)-(d). The structure of the metasurface is metallic (Al) dipoles and substrate separated by continuous dielectric planes of SiO_2 and Ge. The principle design variables in the unit cell of the dipoles are periodicity, p, length, l and width, w of dipoles and the height of dielectric layers (SiO_2, Ge) as substrate, h_1 and h_2. During fabrication procedure, the periodicity is determined by the diameter of microspheres because the microspheres are hexagonally close packed. The length and width of aluminum dipoles can be controlled by adjusting exposure dose, which is presented in previous study [9]. The heights of dielectric layers are specified in deposition. The substrate of the metausrface presented in this work is prepared by depositing 150 nm of aluminum onto glass microscope slide using an electron-beam evaporator (CHA). Then without breaking vacuum, h_1 = 333 nm of germanium follow by h_2 = 50 nm of silica are deposited on the top of the aluminum film. After cooling down to room temperature, the substrate is removed from the chamber and spin-coated with HMDS as adhesion promoter at 5000 rpm for 1 minute. After that, a 480 nm thick film of positive tone photoresist (S1805, Shipley) is spin-coated on the samples followed by a soft bake at 115 °C for 90 seconds. A monolayer of hexagonal close packed, self-assembled silica microsphere with p = 3 μm (nominal) in diameter is transferred from air/water interface onto the photoresist layer as shown in Figure 1(b). The silica microspheres mixed in butanol are firstly dispensed on water surface in a Teflon beaker, and then the microspheres are floating on the air-water interface and eventually self-assembled on the interface with small single crystals on water surface

inside a beaker. The microsphere array is finally transferred onto photoresist while pulling the substrates out of the water surface.

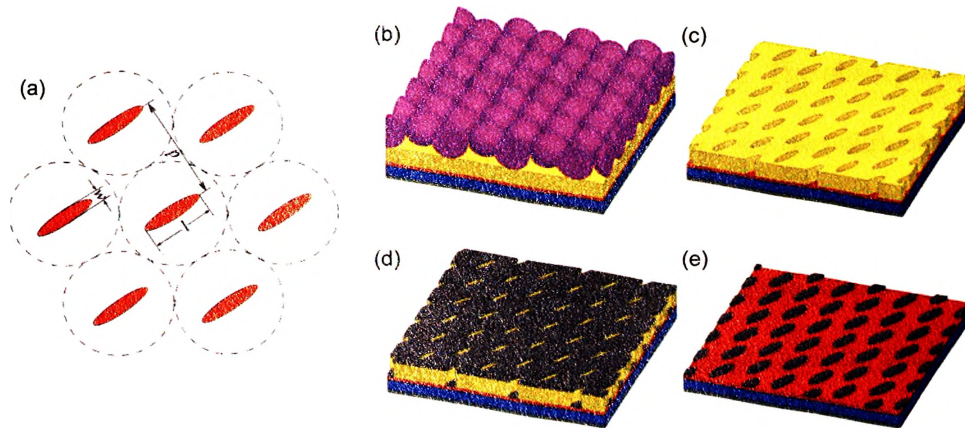

Figure 1. Illustration of creating dipole patterns in MPL process. (a) Self-assembled microspheres form hexagonal close pattern on photoresist (b) dipole arrays in photoresist after off-axis illumination and development (c) deposition of top metal layer (d) the metallic dipoles on SiO_2/Ge/Al substrate (e) top view of a unit cell of the dipole array, showing the metasurface is defined by periodicity *p*, dipole length l and dipole width *w*.

In order to create the array dipole features, the samples are flood exposed using *i*-line illumination with off-axis illumination system. The illumination angle is determined by computer controlled rotation stages that enable continuous rotation of the polar angle from -90° to 90° under a stationary flood illumination source. For this experiment, the samples were exposed five times at different polar angle (±27°, ±12°, and 0°) to create dipoles. The maximum polar angle can be shifted to control the length of the dipoles because the offset of a single exposure site to the center scales with incident angle8.

After exposures, the samples were immersed in MF 319 developer (Microposit) for 60 seconds. The silica microspheres were removed from the top along with the exposed photoresist and the array of dipoles in the photoresist is revealed, as shown in Figure 1(c). Following exposure and development, a 100 nm thick layer of aluminum is deposited on the samples using E-beam evaporator. Then the remaining photoresist is removed in Remover PG (MicroChem) with the help of ultrasonic bath. The final array of Al dipoles is left on the substrate.

The characterization of the metasurface is conducted using a Fourier-Transform Infrared spectrometer (FTIR, Thermo Nicolet Nexus 670) with VeeMAX accessory which enables the controlling of angle (30°-80°) and polarization status of the IR incidence (wavelength range 2.5 μm- 25 μm). The transmittance of the samples is negligible due to the continuous ground layer of optically thick aluminum. Thus the absorptance can be given by $\alpha = 1 - \rho$, where ρ is the reflectance measured with FTIR spectrometer. From Kirchhoff's law, the angle dependent spectral absorptance is equal to the emittance, ε. The instrument is equipped with DTGS detector and KBr beam splitter, and purged with nitrogen gas.

Figure 2 shows simulated absorption spectra of polarized metasurface at 30° off-normal illumination when the dipoles are parallel to the plane of incidence (assuming optimized dimensions and film thicknesses) using HFSS. The simulation model is based on the design with $l = 2.1$ μm and $w = 500$ nm. Figure 3 illustrates the absorptance of TE and TM incidences measured using FTIR. Due to the shape of the dipole resonator, the samples act differently in reflection/emission with polarized light (i.e. TE/TM wave) in IR spectrum. Figure 3 (right) shows the experimental results of samples that exposed at

5.94 mJ/cm^2 with the polar angle vary from -27° to 27°. The red curves represent absorption spectra for TE incidence while blue ones for TM incidence. Among the curves with TE polarized incidences, two main absorption peaks are observed: the peak at ~8 μm is from the phonon resonance, and the peak at ~10.5 μm comes from the dipole resonant mode. The broadband absorption in thermal infrared region (7.5 μm-13 μm) is achieved by hybridizing the dipole mode with phonon modes. The absorptances by dipole resonances are controlled by the heights, h_1 and h_2 of the two dielectric layers. The total absorptance/emittance of the metasurface shown in Figure 3 in 7.5 μm-13 μm region is integrated as 39.80%. For TM polarized incidences, the dipole mode is at width of the dipoles and the absorption peak is at smaller wavelength and the absorptance in thermal infrared region is much lower (8.76%).

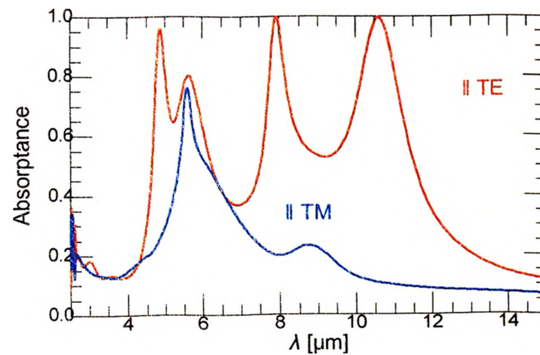

Figure 2. HFSS simulation of polarized metasurface at 30° off-normal illumination when the dipoles are parallel to the plane of incidence (assuming optimized dimensions and film thicknesses). The red line shows the absorption spectrum at TE polarization and the blue line shows the curve at TM polarization incidence.

Hierarchical patterns are ubiquitous in nature range from lotus leaves to butterfly wings that inspired biomimetic design such as superhydrophobicity. One of the advantages of MPL approach is the ability to fabricate hierarchical pattern metasurface over large scale with relatively low cost [10]. Applications such as thermophotovoltaics that need large patterned area can be beneficial from this approach. Figure 4 illustrates the basic concept. According to the fabrication procedure described above, a mask of a hollow university's logo was used on photoresist during exposures. The polar angle of flood illumination varies from -24° to 24° to create dipole array as resonators. The surroundings were not exposed as control area. After lift-off, only university logo area has dipole arrays. The sample was uniformly heated up on a hot plate and imaged using a thermal infrared camera (FLIR SC500) with a linear polarizer placed between the thermal camera and the sample. Firstly, the university logo appeared when the polarization of emittance from logo was parallel to the polarizer by adjusting the angle of the polarizer, as shown in Figure 4 (a). The difference in emittance between university logo area and surrounding areas creates an obvious temperature difference in the image. Then the logo disappeared when the polarizer turned 90°, which means the emittance from logo and background are identical at the specific polarization orientation, as shown in Figure 4 (b). The hierarchical pattern provides the polarization dependence on cloaking in thermal infrared spectrum.

3. CONCLUSION

This paper presents fabrication of broadband, polarization dependent metasurface emitters in thermal infrared spectrum with microsphere photolithography, a low-cost and

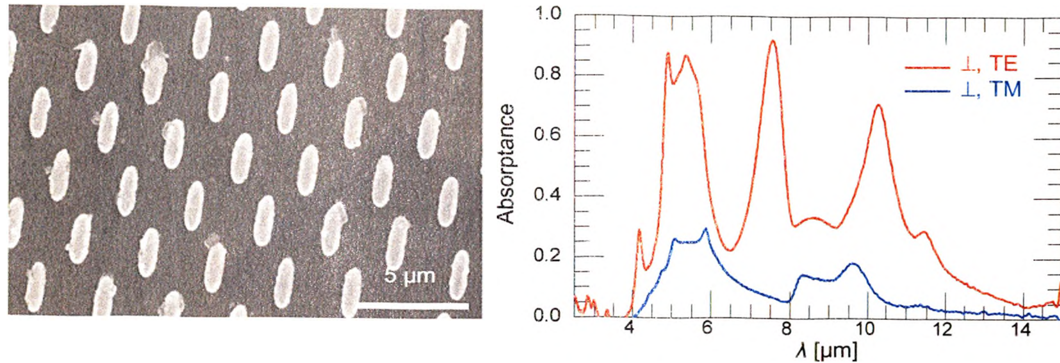

Figure 3. (Left) SEM image of dipole arrays fabricated in MPL approach (Right) Absorption spectra of TE (red) TM (blue) incidences from sample exposed with polar angle from -27° to 27°.

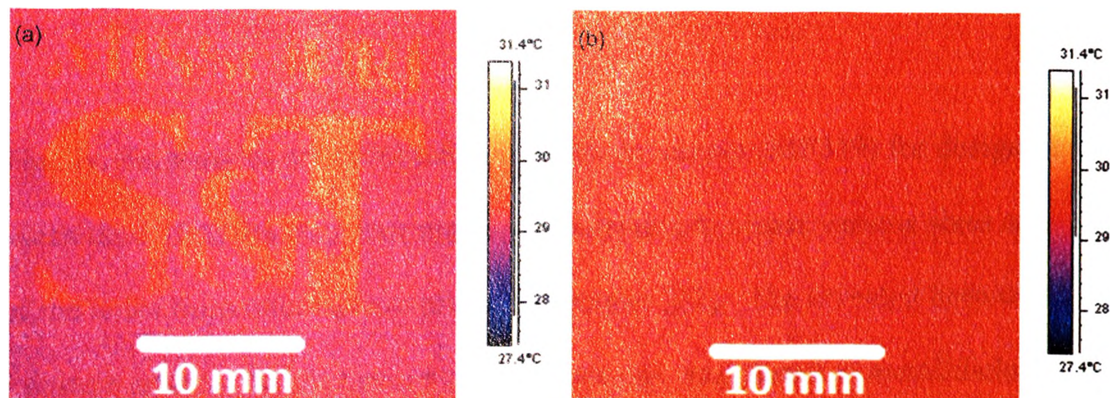

Figure 4. Thermal images of hierarchical FSS metasurface through a polarizer whose orientation (a) parallel to the polarization of emittance (b) perpendicular to the polarization of emittance.

scalable fabrication technique. The emitter achieves broadband absorption by hybridizing dipole modes at multiple cavities and phonon mode resonances. MPL process enables creation of flexible designs on length and width of dipoles for optimization of the performance of the metasurfaces. The absorptance change from TE to TM polarized incidences is 39.80% to 8.76% with a contrast of 31.04%. Temperature

dependence on polarized emittance through radiation heat transfer is captured by thermal infrared camera. The large-area, polarized emitting metasurfaces with hierarchy fabricated using microsphere photolithography are potentially used for infrared cloaking and filtering applications.

REFERENCES

[1] Mohseni, H., "Nanosphere photolithography for sub-100nm features," SPIE newsroom, 15 March 2016, http://spie.org/newsroom/6382-nanosphere-photolithography-for-sub-100nm-features.

[2] Tang, Y., Bossard, J. A., Werner, D. H., and Mayer, T. S.. "Single-layer metallodielectric nanostructures as dual-band midinfrared filters," Applied Physics Letters, 92(26), 263106-263106-3(2008).

[3] Ginn, J., Shelton, D., Krenz, P., Lail, B., and Boreman, G., "Polarized infrared emission using frequency selective surfaces," Optics Express, 18(5), 4557-63 (2010).

[4] Puscasu, I., Schaich, W., and Boreman, G. D., "Resonant enhancement of emission and absorption using frequency selective surfaces in the infrared," Infrared Physics & Technology, 43(2), 101-107 (2002).

[5] Bonakdar, A., Jang, S. J., Brown, R. L., Rezaei, M. and Mohseni, H., "Deep UV microsphere nanolithography to achieve sub-100 nm feature size," Proc. SPIE 9170, 16 (2014).

[6] Chen, Z., Taflove, A. and Backman, V., "Photonic nanojet enhancement of backscattering of light by nanoparticles: a potential novel visible-light ultramicroscopy technique," Optics express, 12(7), 1214-1220 (2014).

[7] Zhang, Y., Wei, T., Xiong, Z., Shang, L., Tian, Y., Zhao, Y., Zhou, P., Wang, J., and Li, J., "Enhanced optical power of GaN-based light-emitting diode with compound photonic crystals by multiple-exposure nanosphere-lens lithography," Appl. Phys. Lett. 105(1), 013108 (2014).

[8] Qu, C. and Kinzel, E. C., "Infrared metasurfaces created with off-normal incidence microsphere photolithography," Optics Express, 25(11), 12632-12639 (2017).

[9] Qu, C. and Kinzel, E. C., "Polycrystalline metasurface perfect absorbers fabricated using microsphere photolithography," Optics letters, 41(15), 3399-3402 (2016).

[10] Qu, C. and Kinzel, E.C., "Thermal Radiation From Microsphere Photolithography Patterned Metasurfaces," ASME 2017 Heat Transfer Summer Conference, American Society of Mechanical Engineers. V002T13A007-V002T13A007 (2017).

V. MODELING OF MICROSPHERE PHOTOLITHOGRAPHY

Chuang Qu, Chen Zhu, Edward C. Kinzel

Department of Mechanical and Aerospace Engineering,

Missouri University of Science and Technology, Rolla, MO 65409, USA

ABSTRACT

Microsphere photolithography is a micro/nano fabrication technique that utilizes self-assembled microsphere array to focus light into photonic jets and create orderly periodic pore arrays in photoresist. This paper studies on modeling of microsphere photolithography process. The model contains main process parameters such as exposure dosage, development duration, and thickness of photoresist, which determine the characteristics of the features generated from the process. With the experimental validation of the models, more simulation cases such as the discussion on resolution and off-normal illuminations are presented. Sub-100 nm hole/disk arrays are achieved in the experiment by the predicted fabrication conditions from simulation. Additionally, micron-scale split-ring resonator arrays are experimentally demonstrated with the fabrication conditions predicted from linear superpositions of the simulation results for multiple off-normal incident microsphere photolithography. This paper provides guidance for creating large-area micro-/nano- structure arrays using microsphere photolithography for potential sensing and energy management applications.

Keywords: microsphere photolithography, modeling, simulation, nanomanufacturting, metasurface.

1. INTRODUCTION

Over the past decade, the class of structure composes of highly ordered periodic features with micron/sub-micron scale feature sizes and periodicities has been developed as visible/infrared metasurfaces, photonics crystals, hydrophobic/hydrophilic surfaces, to name a few. The devices with such class of structures are widely used for cloaking [1], sensing [2], and thermal detections [3], etc. One challenge in the study of the structures is that the devices are cost-prohibitive and time-consuming in fabrication, especially for the ones with large areas. For example, Electron-Beam Lithography (EBL) [4] and Focused Ion Beam (FIB) milling [5] are capable of prototyping of these structures only for lab scales. NanoImprint Lithography (NIL) [6] and Interference Lithography (IL) [7] are promising alternatives; however, the structures are limited to planar substrates, and the experimental setups are complicated and demanding. Bottom-up fabrication approaches utilizing the self-assembly of dielectric microsphere /nanospheres are proposed as well. Nanosphere Lithography (NSL) [8] utilizes the interstices between the spheres as shadow masks for nanopattern transfers. The hexagonal-closed-packed (HCP) sphere array limits the distribution pattern and the shape of the elements while the particles are not recycled after use.

Microsphere photolithography (MPL) is proposed as a simple, cost-effective, and high-throughput manufacturing alternative for highly ordered periodic microstructures on large areas [9]. MPL uses the microsphere as microlenses instead of shadow masks in NSL; the spheres work in parallel in creating the structures for large-areas with single exposures while maintaining decent resolution of sub-100 nm [10]. MPL transfers the periodic pattern to the photoresist by the photo-chemical process as conventional

photolithography with photonic jets [11]--subwavelength, energy-enhanced wave fields generated by the spherical lenses. MPL exhibits the flexibility of creating metasurfaces with complex designs and hierarchical topography of the periodic features combining with the tailoring of the incident angles of the photonic jet by either Fourier mask [12] or tip/tilt stages [13]. Previous references have demonstrated the capability of MPL for fabrication of perfect absorber metasurfaces [14], LED [15], and localized surface plasmon resonance devices [16] for potential sensing [16], condensation control [17], and energy management applications.

The modeling of optical lithography and development of photoresist (PR) begins in the early 1970s since the work by Dill et al [18-19]. The references described the important parameters for photoresist: A, B as the bleachable and non-bleachable absorption coefficient, respectively; and C as the exposure rate constant for photoresist. In the photo-chemical patterning process for positive photoresist, the UV light alters the chemical composition of the inhibitor to be more soluble to the developer. The relative concentration of the inhibitor is dependent on the energy distribution of the light inside the photoresist as explained by exposure kinetics. Meanwhile, the concentration of inhibitor directly affects the development behavior [20]. Lithography simulators are developed based on the exposure and development models with specified etching algorithms. For example, in SAMPLE, string model algorithm describes the boundaries for developed and undeveloped regions approximated by a series of points [21]; linear weight method creates the weights of the photoresist profile by summing up line segments at give positions (PROLITH/2) [22]; and 3D cell-removal algorithm uses logic matrices for the characterization of development status of cells (SOLID) [23]. However,

these simulators are not used for the modeling for MPL because of the specialty of the photonic jet.

This paper explores the modeling and simulation of the MPL process. Section 2 illustrates the general fabrication process using microsphere photolithography in detail. Section 3 describes the modeling process. With the model verified by experimental results shown in Section 4, the fabrication conditions for achieving the resolution is discussed. Finally, the ability of the simulation for off-normal incident illuminations is shown by the demonstration of the metasurface with split-ring resonator elements.

2. FABRICATION PROCESS

Samples with various fabrication conditions are created using microsphere photolithography. The standard fabrication MPL procedures are: 1) application of photoresist; 2) application of microsphere array; 3) exposure; 4) development.

Deposition and soft-bake are important steps when applying the photoresist onto the substrate. The physical properties of the photoresist such as thickness, Dill parameters, and refractive index are important to the photo-chemical reaction and affected by the deposition and soft-bake procedures. The photoresist used in this paper is Shipley S1805 positive photoresist. The thickness h of the photoresist is normally determined by spinning/accelerating rates in spin-coating, and it can be thinned further by mixing its solvent Propylene Glycol Methyl Ether Acetate (PGMEA) [24]. In the experiments, the photoresists are spin-coated on the substrates at 5000 rpm for 60 seconds. From the measurement by ellipsometry, the thicknesses for mixing ratios of 1:0, 1:0.5 and 1:1.5 (V_{S1805}:V_{PGMEA}) are ~540 nm, 260 nm and 120 nm. Then the

photoresist is soft-baked on a hotplate at 70 °C for 60 seconds. In this process, the solvent is evaporated from the photoresist layer. The residue solvent has a powerful influence on the dissolution rate of the photoresist films; it increases the free volume and thus the diffusivity of the exposure products. High baking temperature causes the reducing content of the solvent as well as the inhibitor. Less inhibitor left makes the photoresist less photosensitive, and the patterns can be difficult to be developed especially for small features. Besides, the decomposition of the inhibitor by heating causes dark erosion because the thermal exposure has the same effect as UV exposure. Investigations of the influences of soft-baking on the lithographic performance of both positive and negative photoresists are shown in [25-26] for the optimization of lithography process. The substrates used for all samples in this study are glass. Glass substrates have matched-index to the photoresist for minimizing the standing wave generation in the photoresist.

The microspheres are self-assembled into HCP array by nature. The diameter of the close-packed microspheres determines the periodicity of the features. A monolayer, large-area, and single crystalline array of the microsphere is the ideal template for MPL. Recent studies on improving the area and crystallinity of the monolayer of the microsphere array are described as spin-coating [27], Langmiur-Blodgett [28], and via Air-Water Interface (AWI) [29]. The spheres can be deposited either directly onto the photoresist or on a UV transparent superstrate, which is used as a repeatable sphere mask. In the experiment, AWI method is used: 2 μm-in-diameter dry silica microspheres are mixed in the solution 1-butanol with 30 mg/L of SDS surfactant; the microspheres are assembled on air-water interface over the substrate, and then directly transferred onto the

photoresist layer when the water dries out. The refractive index of the silica microspheres is 1.45 [30].

The photoresist under the sphere array is illuminated by UV light source. The wavelength of the light source [10], the incident angle [31], and exposure dosage [14] are important aspects for size control of the features in the exposure process. I-line light source (λ=365 nm) is used to expose S1805 photoresist in this paper. In the experiments, the sweep of exposure dosages is accomplished by changing the exposure duration as

$$E_{\exp} = I_{src} \times t_{\exp} \tag{1}$$

where $E_{\exp}$ denotes for the exposure dosage (mJ/cm^2), I_{src} presents the constant power intensity for the light source (14 mW/cm^2 for the work in this paper); and $t_{\exp}$ is the exposure duration. The power intensity is redistributed inside the photoresist at each location ($I_{PR}(x,y,z)$) by the focusing effect of the microspheres; $I_{PR}(x,y,z)$ is estimated using electromagnetic (EM) simulations of the E-field ratios and the equation below:

$$R_E = \frac{I_{PR}(x,y,z)}{I_{src}(x,y,z)} = \left[\frac{E(x,y,z)}{E_0(x,y,z)}\right]^2 \tag{2}$$

The E-field intensity distribution $E(x,y,z)$ in the photoresist can be determined by full-wave frequency domain Finite Element Method (FEM) ANSYS HFSS. The incident polar and azimuth angles are controlled by a tip-tilt stage which enables ranges of azimuth angle φ [0°, 360°) and polar angle θ [-90°, 90°] with angle resolution of 0.015°. These angles are defined in Figure 1. The polar angles are independent on the orientation of the crystal.

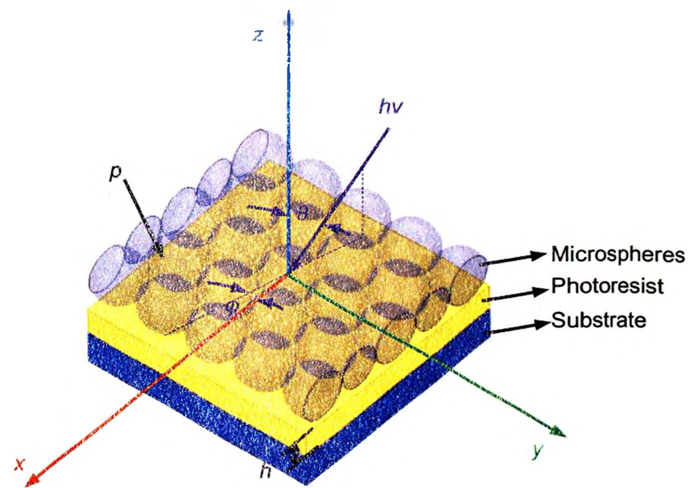

Figure 1. Exposure model.

Finally, the samples are immersed into fresh developer (MF319) for designated development time. The development time was controlled to create various sizes and shapes of the holes from microsphere photolithography [32]. The revealed hole/disk periodic feature array in the photoresist can be inversely transferred to metal/dielectric via lift-off. In this study, the hole patterns are transferred into Al disk array by e-beam evaporation and lift-off (remover PG).

The characterization of the size and shape of the features created in the experiments are conducted by scanning electron microscope imaging (Helios Nanolab 600). The holes in the photoresist are FIB cross-sectioned with prior Pt protection material depositions.

3. MODELING

This section introduces the modeling and simulation of microsphere photolithography. The procedures being modeled include the photo-chemical process in the exposure and the chemical process in the development. The exposure kinetics explains the absorption of the photons by the photoresist and the alteration of the inhibitors by

$$\frac{dm(x,y,z)}{dt_{\exp}} = -C \cdot I_{PR}(x,y,z) \cdot m(x,y,z) \tag{3}$$

where m is the relative concentration of the inhibitor of the photoresist; C is the exposure constant (Dill parameter); $I_{PR}(x,y,z)$ is the power density at the position (x,y,z) in the photoresist shown in equation (2). For a constant I_{PR} at the location (x,y,z), the integration of exposure time t_{exp} in (3) gives

$$m(x,y,z) = \exp[-C \cdot E_{PR}(x,y,z)] \tag{4}$$

E_{PR} denotes the energy at location (x,y,z) in the photoresist and determines the concentration of inhibitor left at the location after exposure.

The original Mack model [20] gives the simple development kinetics that the updated concentration of the inhibitor m directly affects the development behavior by changing the development rate by assuming the development rate is reaction-controlled

$$R = R_{\max}(1-m)^n \tag{5}$$

where $R_{\max}$ denotes the maximum development rate for fully exposed photoresist; n represents the number of exposure or deblocking events that work together to get one resin molecule into solution. The development process can be regarded as a chemical

etching process that the photoresist reacts with the developer while the status of the photoresist updates with time. The three-dimensional (3D) cell-removal algorithm [24] is used in our development simulation. In this algorithm, the 3D photoresist domain, which is investigated in FEM simulations of the E-field distributions, is divided into brick volumes. For the models in this paper, the cubic volumes are uses with edge length ΔL (5 nm). The development time t_{dev} is also divided to time steps Δt_{dev}. The maximum time step is chosen to be 0.0125s, as suggested in [33]. A MATLAB code is included in the supplementary information.

Figure 2(a) shows the E-field distribution inside a 540 nm-photoresist from EM simulation by ANSYS HFSS. With the E-field ratios as input, the resulting hole profile simulated from the development model with the exposure dosage of 1.14 mJ/cm^2 and ~30 seconds of development is shown in Figure 2(b). The same sample is created in experiment; Figure 2(c) shows the corresponding SEM image of the cross section of the hole from experiment.

There are three sets of parameters used for the photoresist development modelling process in addition to the exposure properties: 1) refractive index of the photoresist for the exposure wavelength; 2) Dill parameter C; 3) R_{max} and the n. The refractive index of photoresist is determined by ellipsometry and as input of the electromagnetic simulation. The C parameter is measured in transmission experiments as described in [19]. The R_{max} and n numbers are fitted parameters; the starting point of the numbers for fitting are referred to in [22, 34]. While the differences of diameter of holes (D) between the corresponding experiment results and simulation results are minimized, the fitting numbers are summarized in Table 1.

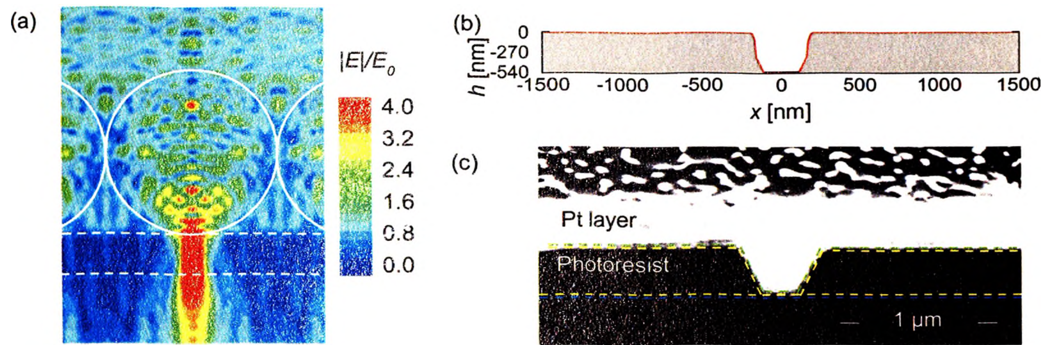

Figure 2. (a) E/E_0 ratio from HFSS simulation; (b) Hole profile generated from development model (scale changed for matching (c)); (c) Hole profile from SEM image with 52° tilt while imaging. The hole is in 540 nm photoresist; exposure dosage for this sample is 1.14 mJ/cm^2; the development duration is 15s.

Table 1. Fitting parameters used in the model.

Parameter \ *h* [nm]	540	260	120
R_{max}	60	63	66
C	0.04	0.032	0.018
n	2.7	1.8	1.4

4. DISCUSSION

4.1. RESOLUTION STUDY

Figures 3 and 4 show the validation of the model by experimental data for all of the process parameters discussed. Figure 3 contains the exposure dosage curves for 120 nm, 260 nm and 540 nm thick photoresist for 15 seconds of development. In Figure 3,

the curves are the simulation results from the model described in Section 3 and the solid square data points with error bars are from the experimental results. Figure 4 shows the simulated and experimental dosage curves for the 540 nm thick photoresist and development duration is of 15 and 60 seconds. The fitting parameter in the model are kept constant for the simulations of the different development durations. The insets in Figures 3 and 4 are representive SEM images for holes under various exposure dosages, development durations, and thicknesses.

The average error between the experimental data and the simulation results, determined from all of the data in Figures 3 and 4, is 8.11%. The relatively small error

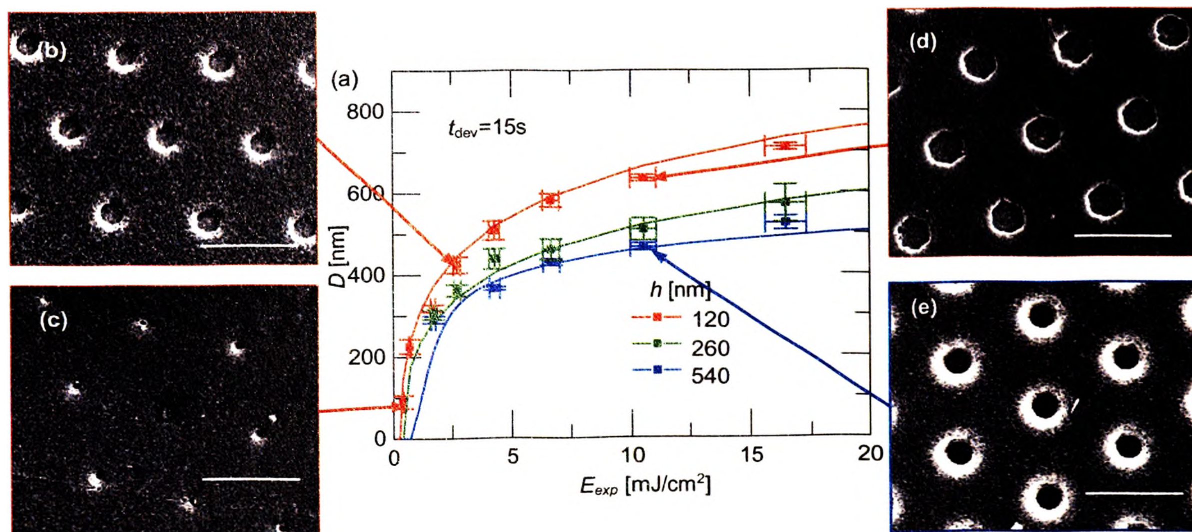

Figure 3. (a) Hole diameter versus exposure dosage on various thicknesses of photoresist with 15 seconds development durations. Red, green, and blue dots/lines are for the 120 nm photoresist, 260 nm photoresist, and 540 nm thick photoresist, respectively. Representative SEM images of hole arrays for (b) 120 nm thick photoresist with exposure dosage of 2.71 mJ/cm^2; (c) 120 nm thick photoresist with exposure dosage of 0.42 mJ/cm^2; (d) 120 nm thick photoresist with exposure dosage of 10.50 mJ/cm^2; (e) 540 nm thick photoresist with exposure dosage of 10.50 mJ/cm2. Scale bar: 2 μm.

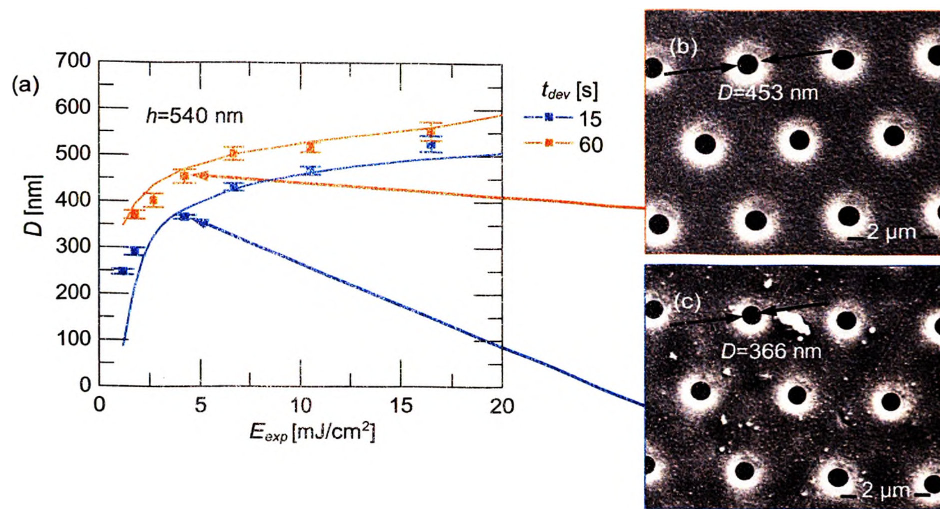

Figure 4. (a) Hole diameter versus exposure dosage for various development durations on 540 nm thick photoresist. The blue and orange symbols are for the 15 and 60 seconds developments, respectively. (b) SEM image of the sample processed with 4.26 mJ/cm^2 exposure dosage and 60 seconds development time; (c) SEM image of the sample processed with 4.26 mJ/cm^2 and 15 seconds development time. Scale bar: 2 μm.

between the simulation data and experimental results quantified over a wide range of process parameters demonstrated the validity of the model. The validation of the models permits confident simulation of more fabrication conditions, including the parameter sets where experimental results are challenging to obtain. The results for the simulation with expanded process parameter sets are included in Figure 5 (c).

Figure 5 (a) and (b) shows examples of the flow path of the developer during the process for 120 nm photoresist. The minimum development time (τ_{min}) in MPL process in defined as the development time from which a hole is through photoresist. The relationship between the actual development time and τ_{min} determines whether the hole pattern can be transferred by sensing if the holes are through. Figure 5 (a) and (b) show two series of hole profiles from various development durations under two exposure

dosages for 120 nm photoresist. Before the minimum development time ($0.8\tau_{min}$), the holes are not through the photoresist. In the development model, the development rate scales exponentially with the energy inside the photoresist, this means the central portion (location of the photonic jet kernel) develops easier. The developer at the center of the exposed region firstly reaches to the bottom of the photoresist at τ_{min}, which results in very small features. Then the photoresist is developed laterally with the gradient of the development rate profile when the development in the center reaches the bottom of the photoresist, causing an increase in the hole diameter. At the same time, the sidewall of the holes increases as the development goes, and eventually becomes vertical on both sides ($1.2\tau_{min}$-$2.4\tau_{min}$). The holes with vertical sidewalls are ready for pattern transferring.

The τ_{min} is important since it can be used for determining the suitable development durations for achieving small features. At the center of the exposed region (x=y=0), the dosage ratio along z direction can be regarded as a constant. Using equations (2)-(5), τ_{min} can be estimated by the equation as

$$\tau_{\min} = \frac{h}{R_{\max} \cdot \left(1 - \exp\left(-C \cdot E_{\exp} \cdot R_E\big|_{x=y=0}\right)\right)^n} \qquad (6)$$

Using the dosage ratio at the center from EM simulation, τ_{min} is estimated without implementing the development model. Additionally, when only the diameter of the spheres changed from p_1 to p_2, the dosage ratio E_{R2} is easily estimated as p_2^2/p_1^2 times of the original ratio E_{R1}. Meanwhile, the exposure dosage threshold can be estimated when the minimum development time is pre-determined:

$$E_{\exp} = -\frac{1}{C \cdot R_E} \ln\left(1 - \sqrt[n]{\frac{h}{\tau_{\min} \cdot R_{\max}}}\right) \tag{7}$$

The trade-off between τ_{min} and the exposure dosage E_{exp} is plotted in Figure 5 (d) as determined from the above equations for 3 thicknesses of photoresist. τ_{min} saturates to h/R_{max} when the exposure dosage is high enough. At small exposure dosages, 120 nm photoresist exhibits wider range of exposure for finite development durations. The 120 nm-thick photoresist is used for the analysis in the following discussions.

The diameter of the holes is dependent on the lateral development rate at the bottom layer of the photoresist. As mentioned above, the dosage ratio R_E at the bottom layer (h=-120 nm) has a Gaussian distribution with respect to its position along x-axis. With equations (2)-(5), the development rate R with respect to the exposure dosage and position can be expressed as

$$R\big|_{z=-h}(E_{\exp}, x) = R_{\max} \cdot \left(1 - \exp\left(-C \cdot E_{\exp} \cdot R_E\big|_{z=-h}\right)\right)^n \tag{8}$$

where the dosage ratio to x is expressed by fitted Gaussian curves:

$$R_E\big|_{z=-h} = A(h) \cdot e^{-x^2/(s(h))^2} \tag{9}$$

In this equation, the amplitude A and standard deviation s are determined by the thickness of the photoresist. The holes are symmetric to y=0 and x=0 in xz and yz planes, so the change of the diameter ΔD is 2 times of the change in x (Δx). Generally, the partial derivation of the diameter of the holes to the exposure dosage (sensitivity 1, s1) is expressed as

$$\frac{\partial D}{\partial E_{\exp}} = \frac{-(s(h))^2}{E_{\exp} \cdot x} \tag{10}$$

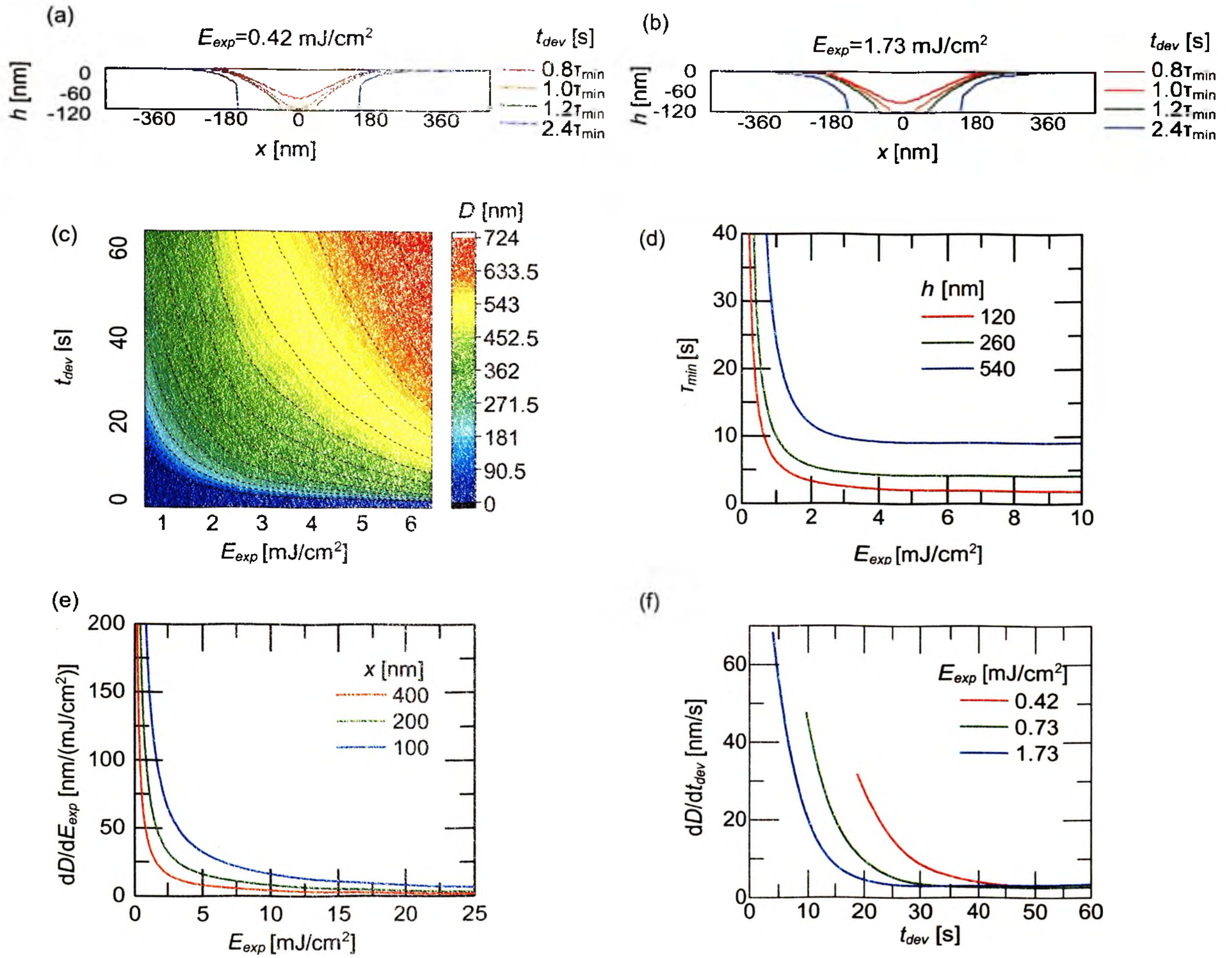

Figure 5. (a) Hole profiles with exposure dosage of 0.42 mJ/cm^2 and development durations of $0.8\tau_{min}$, τ_{min}, $1.2\tau_{min}$ and $2.4\tau_{min}$; (b) Hole profiles with exposure dosage of 1.73 mJ/cm^2 and development durations of $0.8\tau_{min}$, τ_{min} and $1.2\tau_{min}$ and $2.4\tau_{min}$;(c) The dependence of the diameter of holes (color) on exposure dosage (x) and development time (y); (d) The trade-off relation between the minimum development time τ_{min} and minimum exposure dosage E_{exp} for a through-hole for three thicknesses; (e) Sensitivity curve s_1 describing the exposure dosage dependency of the diameter of the holes; (f) Sensitivity curve s_2 describing the development time dependency of the diameter of the holes.

where x<0. This sensitivity is affected by three parameters: the exposure dosage, the exposed location, and the variance with respect of the thickness of the photoresist. The sensitivity curves of the diameter of the holes to the exposure dosage at different

locations are shown in Figure 5 (e). As the equation and the curves indicates, there is a similar trade-off between the sensitivity and the exposure dosage. The diameter is more sensitive to the dosage when the location is closer to the center of the photonic jet because of the higher development rate.

The equation above clearly states that the dosage sensitivity is inversely related to the exposure dosage, regardless of the x value. As plotted in Figure 5 (e), the sensitivity begins to saturate when the exposure dosage is high. The constant sensitivity, also the slope on the exposure dosage curves, indicates that the diameter D has an approximately linear dependence on the exposure dosage in the range where s1 curve is saturated. The variance $(s(h))^2$ affects the onset of the linear region that lower variance in the Gaussian distribution of the development rate results in lower onset of the exposure dosage.

Figure 5 (f) shows the sensitivity curve s_2 with respect to the development time under various exposure dosages. The sensitivity is extremely high in the first few seconds of the development, especially for high dosages. The variation of the diameter of the holes can be >100 nm if the development time control is within ±1s. The Gaussian-shaped distribution of the energy inside the photoresist is accounted for this phenomenon. The non-linear gradient of the energy/development rate to the distance near the center of the jet causes the abrupt change of the diameter when the hole is through. The energy/development rate gradient with respect to the distance to the center becomes linear afterwards and the holes are increasing with development time at a relatively constant ramping rate. Based on the above analysis, small dosage (0.42 mJ/cm^2), controllable development time near τ_{min} (12.5s) and 120 nm photoresist are used in the experiment for discovering the resolution of microsphere photolithography. Figure 6

shows the SEM images for the sub-100 nm holes (a) and disk array (b)-(c) found on the samples.

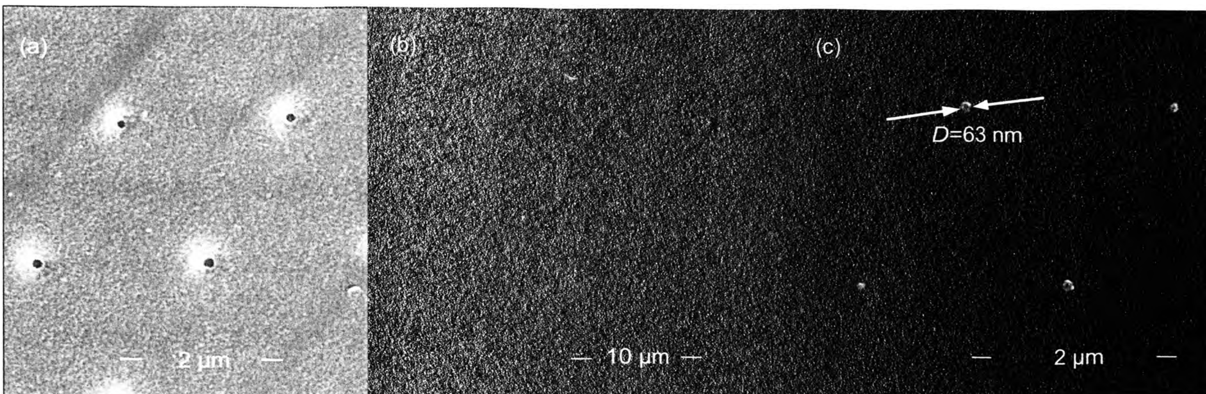

Figure. 6. SEM images of (a) sub-100 nm holes (b) sub-100 nm Al disk array (c) sub-100 nm disks are from the fabrication condition of 120 nm photoresist, 0.42 mJ/cm^2 exposure dosage, and 15 second development time.

4.2. SIMULATION FOR OFF-NORMAL ILLUMINATIONS

Microsphere photolithography has been demonstrated in [13, 31, 35] for fabrication of complicated micro-level antenna designs such as dipoles, tripoles and split-ring resonators. An important patterning rule is that the offset of the holes to the center of the microsphere scales with the polar angle of the incidence. The element designs are easily achieved by the combination of multiple exposures at various polar angles and azimuth angles.

An off-normal incidence case is simulated and experimentally validated as follows. Figure 7(a)-(d) shows the shape of the features on 540 nm photoresist from simulation, with an exposure dosage of 1.14 mJ/cm^2, incident polar angle θ=30° and

azimuth angle φ=0°, and development durations of 5s and 120s. The offset of the exposed location to the center of the sphere for 30° incidence is 569 nm in x-axis. Both the experiment and the simulation show that the hole is not through at 5-second development for this small exposure dosage. The photoresist exposed by the central portion of the jet at the exposure side is etched out faster than the peripheral areas, because the higher energy density at the center of the jet creates higher development rate. The tilted hole develops with sidewall angles decreases as the development proceeds. The hole is through for 120 seconds of development as shown in Figure 7(c)-(d) and the hole is ready for pattern transfers. The SEM image shown in Figure 7(e) shows the shape agreement with the hole profile from the simulation. Figure 7(f) shows the dependency of the effective diameter of the feature on various exposure dosages and development times for 540 nm photoresist. The effective diameters are calculated as the ovals generated from the off-normal incident illuminations are regarded as circles. The τ_{min} needed for off-normal illuminations are longer comparative to normally incidences because of the longer distance of the developer need to travel to the bottom of the photoresist.

The following example shows the modeling of linear superposition of multiple exposures for the creation of split-ring resonators. The split-ring resonator is made of 81 distinct exposures of incident polar angles θ of 30° and azimuth angles φ from 33.75° to 326.25° with an increment angle of 3.75° on 120 nm photoresist. The dosage is 0.42 mJ/cm^2 for each exposure and the total development time is 8 seconds. The energy distribution from each exposed location is simulated by HFSS and linearly superposed in the model. Figure 8 (a) shows the energy distribution on the mid-planes (y=0 nm and z=-

60 nm) obtained from HFSS simulation. Figure 8 (b) shows 2D the thickness distribution simulated from the development model where the dark brown region (thickness h=-120 nm) exhibits the final shape of the resonator. Figure 8 (d) and (f) show the 3D topography of the resonator and a hexagonal packed resonator array from the simulations.

The split-ring resonators are created in the corresponding fabrication conditions. The SEM image in Figure 8 (c) shows the resonators in photoresist. Figure 8 (e) and (g) shows SEM images of single Al split-ring resonator and resonator array after metallization and lift-off. The results show the models are suitable for linear superposition of multiple exposures. This gives the ability for MPL to do trajectory and pattern designs and predictions.

5. CONCLUSION

We discussed the modeling of microsphere photolithography process—a simple and cost-effective microfabrication technique for metasurfaces. The feature size from the experiments with various exposure dosages, development durations, and thicknesses of photoresist are compared with our simulation results; an average difference of less than 9% is obtained. For a given photoresist, the diameter of the hole features are co-dependent on the exposure dosage and development time in a reciprocal-style trade-off. The combination of exposure dosage/development time for through-photoresist holes can be determined through the models; this helps predict the fabrication conditions for small features as well. Meanwhile, the diameter of holes, especially for small holes, are highly sensitive to small changes of these parameters, which requests precise controls of the fabrication conditions. The study guides us to fabricate sub-100 nm holes/disks with

controllable longer development time with small exposure dosage in lab. Finally, we show the ability of the simulation of MPL on off-normal incidence illuminations; this helps the trajectory designs on more consistent off-normal illumination problems. The modeling of MPL leads the fabrication of large-area periodic micro/nano feature arrays in a simple and predicable way using microsphere photolithography.

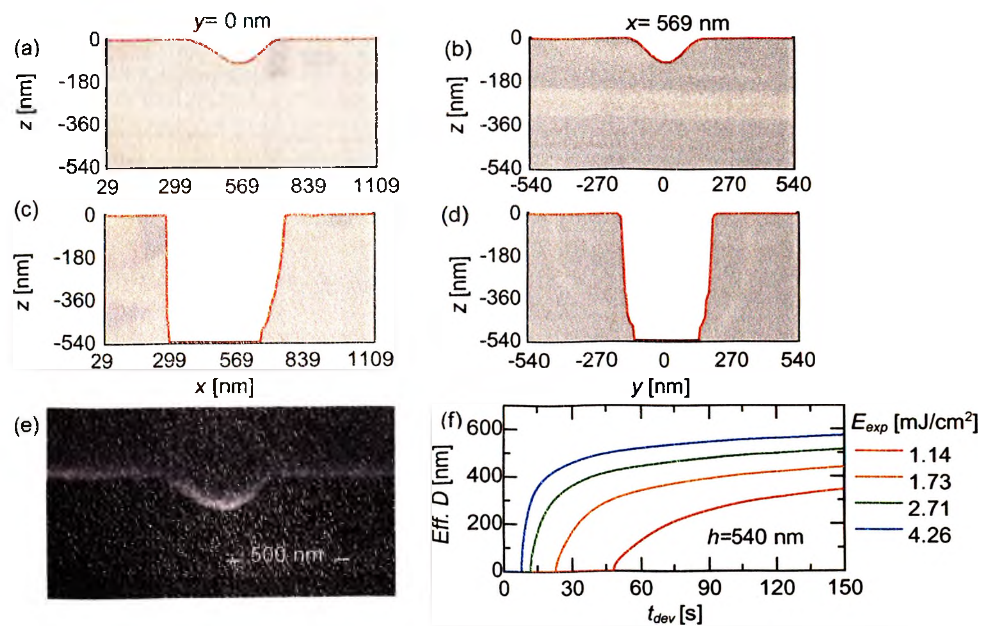

Figure 7. Hole profiles from simulation (a) 5s development, *xz* plane (b) 5s development, *yz* plane (c) 120s development, *xz* plane (d) 120s development, *yz* plane and experiment (e) 5s development, *xz* plane. The exposure is in *xz* plane with an angle of 30° and exposure dosage of 1.14 mJ/cm^2. (f) Effective diameter of holes for various development durations and exposure dosages.

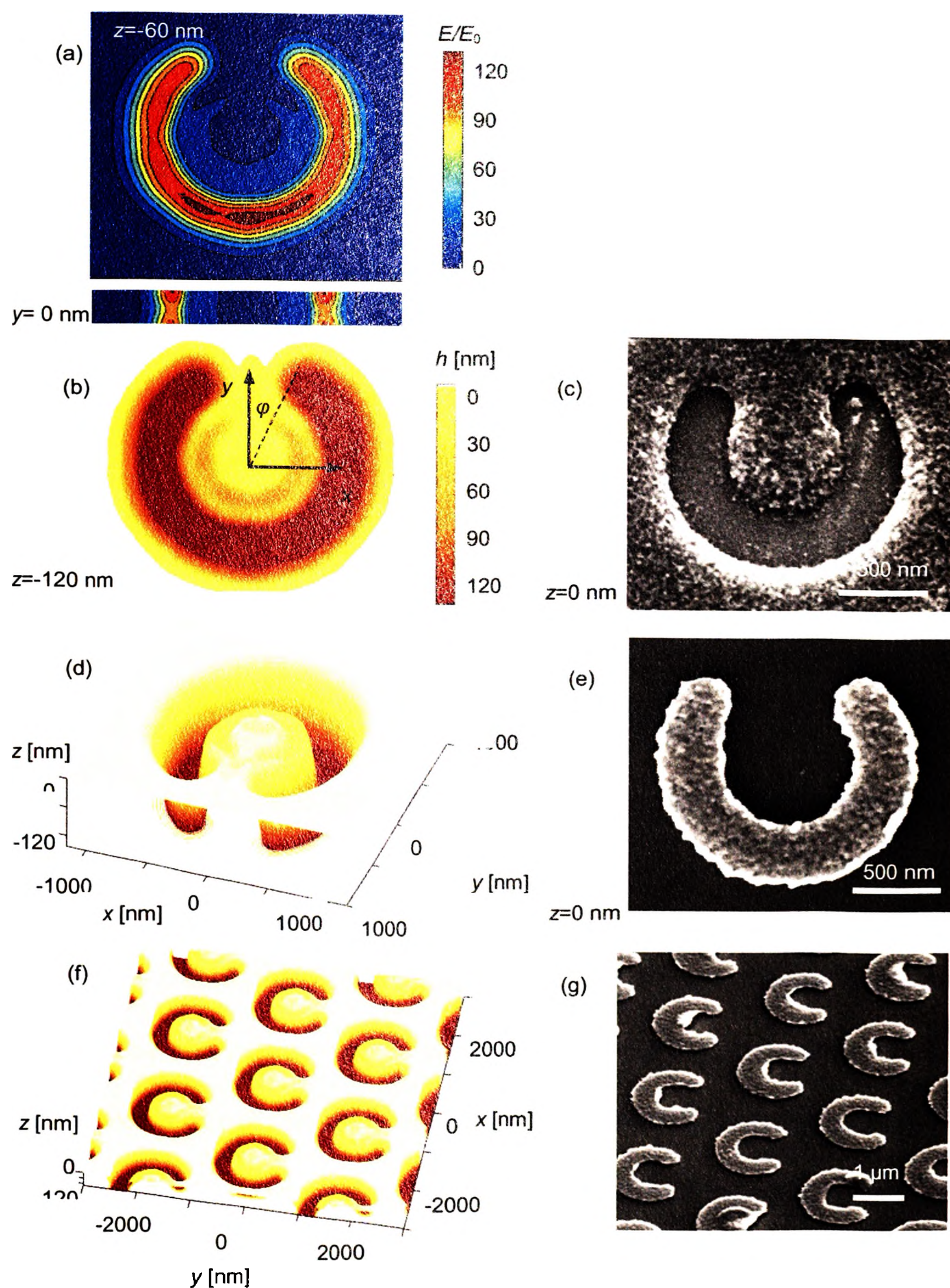

Figure 8. Simulation results and corresponding SEM images of split-ring resonators. (a) E/E_0 after superposition from HFSS simulation; (b) 2D hole profile predicted by development model (z=-120 nm); (c) SEM image of a split-ring resonator in photoresist; (d) 3D Hole profile predicted by development model; (e) SEM image of a single Al split-ring resonator after metallization and lift-off of the sample in (c); (f) 3D hole array from simulation; (g) SEM images of an array of split-ring resonator.

REFERENCES

[1] X. Ni, Z. J. Wong, M. Mrejen, Y. Wang, and X. Zhang, "An ultrathin invisibility skin cloak for visible light," Science 349(6254), 1310–1314 (2015).

[2] B. Lahiri, A. Z. Khokhar, R. M. De La Rue, S. G. McMeekin, and N. P. Johnson, "Asymmetric split ring resonators for optical sensing of organic materials.," Opt. Express **17**, 1107–1115 (2009).

[3] T. Liu, C. Qu, M. Almasri, and E. Kinzel, "Design and analysis of frequency-selective surface enabled microbolometers," SPIE **9819**, 98191V–98191V–8 (2016).

[4] Y. Zhang, T. Wei, Z. Xiong, L. Shang, Y. Tian, Y. Zhao, P. Zhou, J. Wang, and J. Li, "Enhanced optical power of GaN-based light-emitting diode with compound photonic crystals by multiple-exposure nanosphere-lens lithography," Appl. Phys. Lett. **105**, 3–7 (2014).

[5] Zhang, Y., Zhou, L., Li, J.-Q., Wang, Q.-J., and Huang, C.-P., 2015, "Ultra-Broadband and Strongly Enhanced Diffraction with Metasurfaces.," Sci. Rep., **5**, p. 10119.

[6] L. J. Guo, "Nanoimprint lithography: Methods and material requirements," Adv. Mater. **19**, 495–513 (2007).

[7] E. Gazzola, a. Pozzato, G. Ruffato, E. Sovernigo, and a. Sonato, "High-throughput fabrication and calibration of compact high-sensitivity plasmonic lab-on-chip for biosensing," Optofluidics, Microfluid. Nanofluidics **3**, 13–21 (2016).

[8] J. C. Hulteen and R. P. Van Duyne, "Nanosphere lithography: A materials general fabrication process for periodic particle array surfaces," J. Vac. Sci. Technol. A Vacuum, Surfaces, Film. **13**, 1553 (1995).

[9] W. Wu, A. Katsnelson, O. G. Memis, and H. Mohseni, "A deep sub-wavelength process for the formation of highly uniform arrays of nanoholes and nanopillars," Nanotechnology **18**, 485302 (2007).

[10] A. Bonakdar, S. J. Jang, R. L. Brown, M. Rezaei, and H. Mohseni, "Deep UV microsphere nanolithography to achieve sub-100 nm feature size," in *Proc. of SPIE* (2014), Vol. 9170, p. 917016.

[11] X. Li, Z. Chen, A. Taflove, and V. Backman, "Optical analysis of nanoparticles via enhanced backscattering facilitated by 3-D photonic nanojets.," Opt. Express **13**, 526–533 (2005).

[12] A. Bonakdar, M. Rezaei, E. Dexheimer, and H. Mohseni, "High-throughput realization of an infrared selective absorber/emitter by DUV microsphere projection lithography," Nanotechnology **27**, 035301 (2016).

[13] C. Qu and E. C. Kinzel, "Infrared metasurfaces created with off-normal incidence microsphere photolithography," Opt. Express **25**, 12632 (2017)

[14] C. Qu and E. C. Kinzel, "Polycrystalline metasurface perfect absorbers fabricated using microsphere photolithography," Opt. Lett. **41**, 3399–3402 (2016).

[15] T. Wei, K. Wu, D. Lan, Q. Yan, Y. Chen, C. Du, J. Wang, Y. Zeng, and J. Li, "Selectively grown photonic crystal structures for high efficiency InGaN emitting diodes using nanospherical-lens lithography," Appl. Phys. Lett. **101**, (2012).

[16] Y.-C. Chang, J.-S. Huang, and H.-C. Chung, "Controlled fabrication of photonic crystals in situ using nanospherical-lens lithography," SPIE Newsroom **2**, 2–4 (2012).

[17] M. R. Haque, C. Qu, E. C. Kinzel, and A. R. Betz, "Droplet Growth Dynamics during Atmospheric Condensation on Nanopillar Surfaces," Nanoscale Microscale Thermophys. Eng. **33**, 321–332 (2018).

[18] F. H. Dill, A. R. Neureuther, J. A. Tuttle, and E. J. Walker, "Modeling Projection Printing of Positive Photoresists," IEEE Trans. Electron Devices **22**, 456–464 (1975).

[19] F. H. Dill, W. P. Hornberger, P. S. Hauge, and J. M. Shaw, "Characterization of Positive Photoresist," IEEE Trans. Electron Devices **22**, 445–452 (1975).

[20] C. Mack, *Fundamental Principles of Optical Lithography: The Science of Microfabrication,* Wiley, (2007).

[21] S. N. Nandgaonkar and A. R. Neureuther, "A General Simulator for VLSI Lithography and Etching Processes: Part I-Application to Projection Lithography," IEEE Trans. Electron Devices (1979).

[22] C. A. Mack, "PROLITH: a comprehensive optical lithography model," in *Optical Microlithography IV* (International Society for Optics and Photonics, 1985), Vol. 538, pp. 207–221.

[23] W. Henke, D. Mewes, M. Weiß, G. Czech, and R. Schießl-Hoyler, "Simulation of defects in 3-dimensional resist profiles in optical lithography," Microelectron. Eng. **13**, 497–501 (1991).

[24] A. Pozzato, G. Grenci, G. Birarda, and M. Tormen, "Evaluation of a novolak based positive tone photoresist as NanoImprint Lithography resist," Microelectron. Eng. **88**, 2096–2099 (2011).

[25] T. A. Anhoj, A. M. Jorgensen, D. A. Zauner, and J. Hübner, "The effect of soft bake temperature on the polymerization of SU-8 photoresist," J. Micromechanics Microengineering **16**, 1819–1824 (2006).

[26] A. Kozlowski and F. Circle, "Process Optimization of Single Coat Positive Photoresist for Thick Film Applications," **2640**, (2006).

[27] Y. Cheng, P. G. Jönsson, and Z. Zhao, "Controllable fabrication of large-area 2D colloidal crystal masks with large size defect-free domains based on statistical experimental design," Appl. Surf. Sci. **313**, 144–151 (2014).

[28] M. Szekeres, O. Kamalin, R. A. Schoonheydt, K. Wostyn, K. Clays, A. Persoons, and I. Dekany, "Ordering and optical properties of monolayers and multilayers of silica spheres deposited by the Langmuir-Blodgett method," J. Mater. Chem. **12**, 3268–3274 (2002).

[29] X. Meng and D. Qiu, "Gas-flow-induced reorientation to centimeter-sized two-dimensional colloidal single crystal of polystyrene particle.," Langmuir **30**, 3019–23 (2014).

[30] http://en.nanomicrotech.com/products_detail/productId=43.html

[31] A. Bonakdar, M. Rezaei, R. L. Brown, V. Fathipour, E. Dexheimer, S. J. Jang, and H. Mohseni, "Deep-UV microsphere projection lithography," Opt. Lett. **40**, 2537–2540 (2015).

[32] C. Geng, Q. Yan, C. Du, P. Dong, L. Zhang, T. Wei, Z. Hao, X. Wang, and D. Shen, "Large-Area and Ordered Sexfoil Pore Arrays by Spherical-Lens Photolithography," ACS Photonics **1**, 754–760 (2014).

[33] I. Karafyllidis, P. I. Hagouel, A. Thanailakis, and A. R. Neureuther, "An efficient photoresist development simulator based on cellular automata with experimental verification," IEEE Trans. Semicond. Manuf. **13**, 61–75 (2000).

[34] C. A. Mack, "Development of Positive Photoresists," J. Electrochem. Soc. **134**, 148 (1987).

[35] J. Bin Yeo and H. Y. Lee, "Realization of multi-paired photonic crystals by the multiple-exposure nanosphere lithography process," Scr. Mater. **66**, 311–314 (2012).

VI. MASK-BASED MICROSPHERE PHOTOLITHOGRAPHY

Chuang Qu, Edward C. Kinzel

Department of Mechanical and Aerospace Engineering,

Missouri University of Science and Technology, Rolla, MO 65409, USA

ABSTRACT

Microsphere Photolithography (MPL) uses a self-assembled array of transparent microspheres to focus incident ultraviolet radiation and produce an array of photonic jets in photoresist. Typically, the microspheres are self-assembled directly on the photoresist layer and are removed after exposure during development. Reusing the microsphere array reduces the expense of the process. A mask is formed by transferring the self-assembled microsphere array to a transparent tape. This can be used for multiple exposures when pressed into contact with the photoresist. This paper demonstrates the use of this process to pattern infrared metasurface absorbers and discusses the effects of the mask-based MPL process on the metasurface performance.

Keywords: Microsphere photolithography, mask-based, micro/nano fabrication process

1. INTRODUCTION

Infrared and optical metasurfaces are composed of micro/nano- periodic antenna element arrays and are of significant interest for applications such as sensing [1], cloaking [2], energy harvesting [3], and self-cleaning surfaces [4]. Traditional micro/nano fabrication techniques are typically used to prototype metasurfaces including conventional photolithography, electron beam lithography (EBL), and focal ion beam

(FIB) milling. However, these fabrication techniques are cost prohibitive for large scale fabrication required to investigate the performance of metasurfaces over large areas as well as economic production for practical implementations. Techniques with colloidal micro/nanospheres are efficient alternatives to traditional process. Examples include Nanosphere Lithography (NSL) [5], Microsphere Photolithography (MPL) [6-7], Microsphere Projection Photolithography (MPP) [8], and direct write techniques using microspheres [9-14]. Many of these techniques take the advantage of the ability to self-assemble spherical particles into a Hexagonal Close Packed (HCP) monolayer by a number of different techniques. In the classic Nanosphere Lithography technique, a self-assembled HCP particle array is used as a shadow/etch mask. This permits the transfer of triangle shaped patterns at the interstitial locations between the particles. Microsphere Projection Photolithography, the microspheres serve as ball lenses and are used to image a mask onto photoresist at the focal distance of the microspheres. While suffering spherical aberration, the technique has been used to pattern intricate patterns.

Microsphere Photolithography (MPL) uses self-assembled microspheres in direct contact with photoresist to focus collimated radiation to an array of photonic jet. Photonic jet combines near and far-field scattered radiation to produce a sub-diffraction field concentration propagating sustained over a wavelength in the photoresist [15]. The electric field enhancement can be more than two orders of magnitude with a diameter as low as $\lambda 0/3$ FWHM. The large aspect ratio of the photonic jet facilitates pattern transfer via etching or lift-off. Complex patterns can be created by controlling the angular spectrum of the illumination (similar to MPP). This can be accomplished in a local direct-write approach by rotating the sample under a static illumination source [7]. These

dimensions are ideal for patterning metasurfaces in the mid-infrared and can be scaled to near-infrared and visible wavelengths.

Using the microsphere array to focus light as opposed to using the microsphere array as a shadow mask has the advantage that it is not necessarily consumed during the patterning process. This is significant because, while much less expensive than EBL/FIB, the microspheres and their self-assembly still constitute a significant expense. The use of mask- based microsphere arrays has been proposed for laser processing materials such as semiconductors [9-10, 14], metal alloys [11], and polymers [16]. Using a contact mask introduces problems similar to Nano Imprint Lithography (NIL), including contamination and maintaining contact over a large area. However, because the microspheres do not need to physically displace the resist, the wear issues surrounding NIL are reduced as is the fabrication expense of the mask. This paper discusses on creating uniform micro featured array over cm^2 area using microsphere photolithography with a transportable mask. Mid-infrared metasurfaces are created by exploiting multiple exposures using the same mask. The performances of the metasurfaces are used to validate the consistency of the samples when the mask is used at different times.

2. EXPERIMENTS AND DISCUSSION

The setup for the mask-based microsphere photolithography experiments in this paper is illustrated in Figure 1. A thin polyimide substrate (2 mil thick) is spin coated with 480 nm of S1805 photoresist (Microposit). This rests on an elastomer (EcoFlex) of thickness 5 mm. A flexible mask (hexagonal packed microspheres secured by UV transparent tape) is pressed against the substrate using a weight which generates ~4 kPa

across the interface. The center of the weight is open to allow the microspheres to be normally illuminated with a collimated light source through the tape. The conformal nature of the tape and substrate help to ensure good contact as the elastomer helps to distribute the load over the interface.

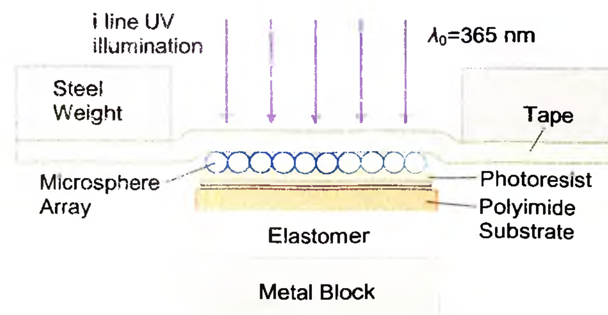

Figure 1. Illustration of mask-based microsphere photolithography approach.

The preparation of the mask begins with the spontaneous self-assembly of a microsphere array on air-water-interface following the protocol in Ref. 17. Dry silica microspheres (2 μm diameter) are first mixed into 1-Butanol solution with a concentration of 300 mg/mL. A glass slide is inserted vertically into a Teflon beaker containing deionized water sufficiently deep enough to submerge the slide. The microsphere/Butanol mixture is dispensed onto the surfaces of the deionized water. Capillary forces cause the microspheres to self-assemble into a Hexagonal Close-Packed (HCP) lattice on the air-water interface. A portion of the microsphere array is transferred onto the glass slide when it is slowly removed from the deionized water at a speed of 0.016 mm/s.

Following inspection of the microsphere array on the glass slide it is transferred to the tape by carefully pressing the adhesive coated side of the tape to the microspheres. Figure 2 shows SEM images of the microsphere mask (tape) along with a 2D Fourier Transform of the image. The microsphere array covers ~25×25 mm^2 area on the tape.

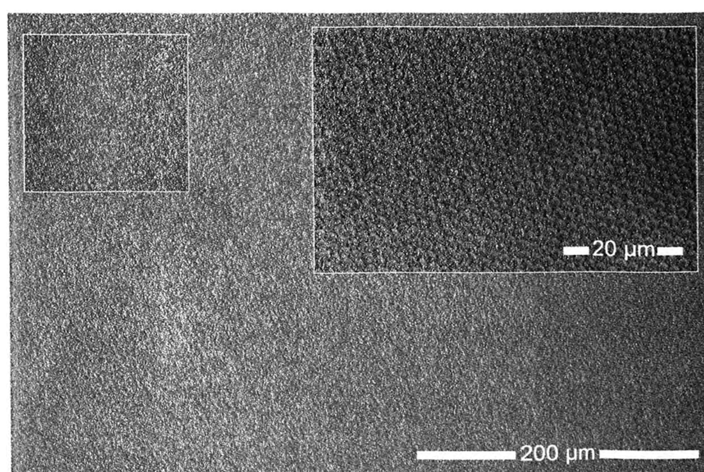

Figure 2. SEM image of microsphere mask (tape) with inset showing 2D Fourier Transform.

The sample, tape mask and metal block are coarsely aligned before illumination with *i*-line (λ_0=365 nm) radiation with irradiation, E=12.5 mW/cm^2 for 3s. Each microsphere generates a photonic jet in the photoresist. The sample is then soft baked at 115 °C for 90 s before developing in MF319 for 60 s to reveal a HCP hole array. Figure 3 shows a SEM image the sample after development. The diameter of the holes is ~940 nm. The periodicity is determined by the diameter of the microspheres while the hole diameter can be controlled by adjusting the exposure fluence [6].

The hole array created by the lithography process can be used for pattern transfer by either etching or the lift-off procedure. Figure 4 shows aluminum disks on the surface of the polyimide created using lift-off of the photoresist following deposition of 100 nm of aluminum using an e-beam evaporator. The photoresist was stripped using ultrasonication in Remover PG (MicroChem). Figure 4 illustrates the importance of controlling the separation between the microspheres and the photoresist. This gap can vary significantly when the weight is not applied especially if a rigid substrate and mask are used. Figures 4a and 4b show different locations of the sample patterned without the weight. Both the size of the disks as well as the periodicity change in regions of the sample that are not in good contact. The doubling of the periodicity can be attributed to the Talbot effect [18]. This is a diffractive effect that generates repeating patterns including doubling the periodicity of the original grating. While the gap used to pattern Figure 4b is not known, it agrees with a frequency-domain FEM simulation (ANSYS Electronics 18.2) of a 10 μm separation between the microspheres and photoresist. This is shown in Figures 4c and 4d which plot the simulated magnitude of the normalized energy in the electric field 240 nm from the surface of the photoresist (midplane) for gaps of 0 and 10 μm, respectively.

While the doubling of the periodicity can be advantageous, maintaining a 10 μm gap precisely over a large area requires optically flat surfaces and significantly raises the expense of the fabrication process. The objective becomes minimizing the gap so that the exposure is directly from the photonic jets. This must be accomplished without excessive pressure leads to wear of the mask, specifically the transfer of microspheres from the tape to the photoresist.

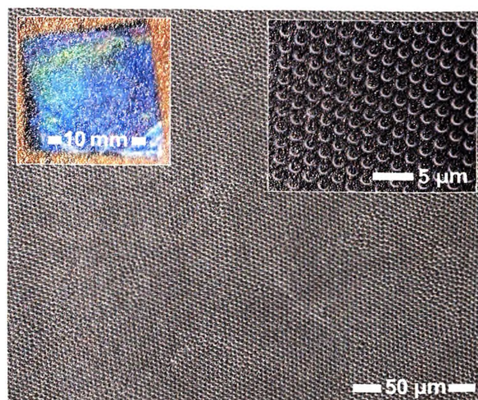

Figure 3. SEM image of holes in S1805 photoresist.

Functional infrared metasurfaces have previously been fabricated using conventional microsphere photolithography with the microspheres directly self-assembled [6-7]. Basic absorbing structures are formed by separating resonant disks from a ground plane by an insulating layer. This structure affords the ability to consistency of the process. Thirteen samples were created with the same tape mask. E-beam evaporation was used to deposit a 150 nm of aluminum onto the polyimide substrate. A 200 nm thick layer of silicon is evaporated on top of the aluminum without breaking vacuum. The photoresist is then spin coated on top of the silicon and exposed using the microsphere mask using a consistent fluence of 62.5 mJ/cm^2. The lift-off procedure was used to pattern the disks on the silicon layer. SEM images of several of the samples are shown in Figure 5.

The absorption spectra of the samples were measured using FTIR (Thermo-Nicolet, Nexus 670). A VeeMAX accessory (Pike) was used to measure the reflectance spectra from the samples over a 9.5 mm diameter aperture from 30° off-normal

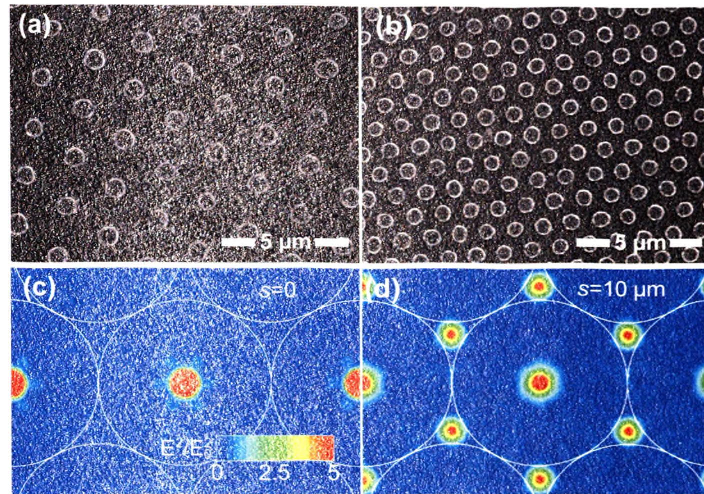

Figure 4. Experimental results showing the change in pattern periodicity due to diffractive effects at large gaps (a) 2 µm periodicity (b) 1 µm periodicity. Scale bar: 5 µm. Simulation on MPL exposure process with different gaps (c) 0 µm (d) 10 µm.

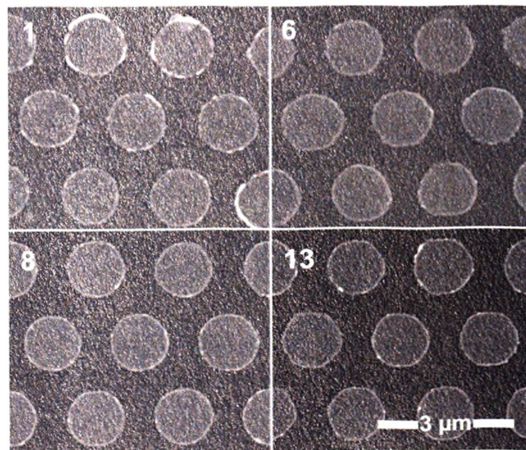

Figure 5. SEM images of samples 1, 6, 8 and 13.

incidence. The reflectance is normalized to the reflectance from a gold mirror. Because there is no transmission through the aluminum ground plane, the absorptance, α, can be calculated from the reflectance, ρ, $\alpha(\lambda) = 1 - \rho(\lambda)$. Figure 6 show the absorptance spectra

from 11 of the 13 samples (all exposed using the same mask). A polarization averaged ANSYS simulation of the metasurface is also plotted (dashed lines) and was designed for resonance at λ=8 μm. At this wavelength and angle of incidence the simulated absorptance is α=0.98.

The resonant wavelength and absorptance of the various samples are summarized in Figure 7. After removing the outliers of Samples 2 and 10, the mean resonant wavelength for the remaining 9 samples is λ=7.99 μm with a standard deviation of 0.09 μm and a mean resonant absorptance of α=0.81 with a standard deviation of 0.07.

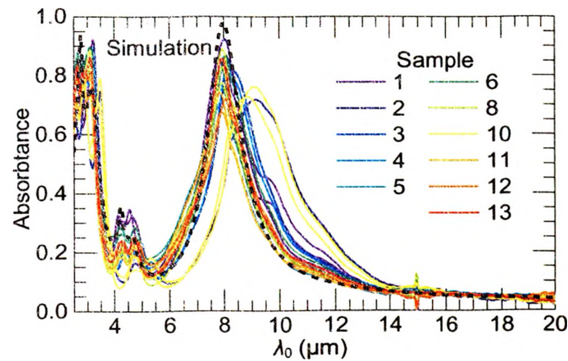

Figure 6. Measured absorptance for different metasurfaces patterned with a common microsphere mask. The simulated absorptance is plotted with a dashed line.

The results in Figures 5-7 suggest the feasibility of the process. The good agreement of the resonant wavelength shows good uniformity in the disk diameters. This indicates that the gap is well controlled. However, the absorptance is significantly lower than the value predicted by simulation. This suggests that the metasurface does not cover the entire aperture. Gaps in the metasurface occur due to defects into the microsphere

mask are transferred to the metasurface. This can be caused by the self-assembly process which results in a polycrystalline HCP array. At the boundaries between the grains, the physical contact can cause the loss of microspheres (transferred to the photoresist). Improving the microsphere deposition process can potentially improve the process. This is limited by the variance in the size of the microspheres (~2% for commercial silica microspheres). These microspheres can nucleate multilayer defects in the lattice.

Control of the contact forces is critical for the process. Using a flexible substrate allows conformal contact and lowers the force required to minimize the gap between the microspheres and the photoresist. The adhesive force provided by the tape is also significant in maintaining the microspheres on the mask. Future studies will resolve the balance of adhesive forces on the microspheres from the mask superstrate and the photoresist.

3. CONCLUSIONS

This paper demonstrates the ability of creating multi-centimeter sized periodic microstructures using mask-based microsphere photolithography. Simulation and experiment show that minimizing the gap is critical for consistent performance. The repeatability of the technique using a simple weight system and flexible substrate is evaluated in the context of an infrared metasurface absorber. This is sufficient for uniform contact over cm^2 areas. A tape based microsphere mask was re-used over 13 times and produces minimal deviations in the resonant wavelength and maximum absorptance. Future work will improve the consistency of these results by improving the mask/microsphere adherence, the uniformity of the HCP lattice.

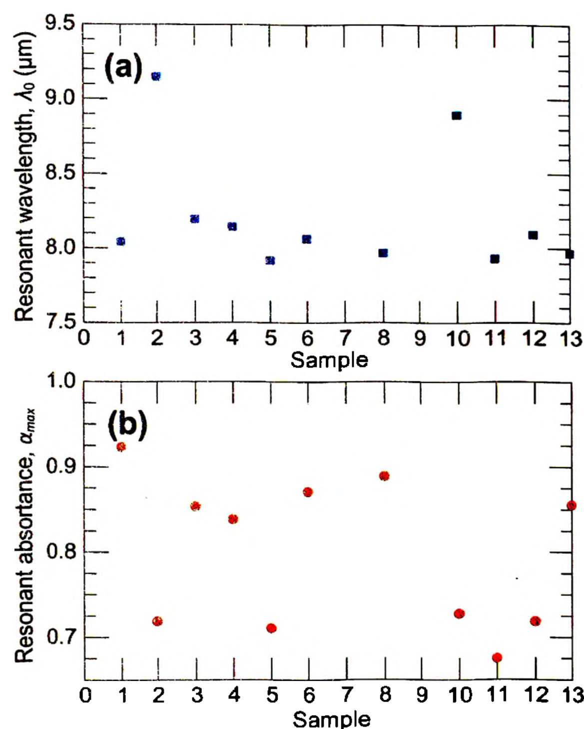

Figure 7. Properties of the different samples (a) resonant wavelength and (b) resonant absorptance.

REFERENCES

[1] Lahiri, B., Khokhar, A. Z., De La Rue, R. M., McMeekin, S. G., and Johnson, N. P., (2009), "Asymmetric Split Ring Resonators for Optical Sensing of Organic Materials.," Opt. Exp., 17(2), pp. 1107–1115.

[2] Ni, X., Wong, Z. J., Mrejen, M., Wang, Y., and Zhang, X., (2015), "For An Ultrathin Invisibility Skin Cloak for Visible Light Materials and Methods," Science, 349, pp. 1310–1314.

[3] Wu, C., Neuner III, B., John, J., Milder, A., Zollars, B., Savoy, S., and Shvets, G., (2012), "Metamaterial-Based Integrated Plasmonic Absorber/emitter for Solar Thermo- Photovoltaic Systems," J. Opt., 14(2), pp. 24005.

[4] Celia, E., Darmanin, T., Taffin de Givenchy, E., Amigoni, S., and Guittard, F., (2013), "Recent Advances in Designing Superhydrophobic Surfaces," J. Colloid Interface Sci., 402, pp. 1–18.

[5] Hulteen, J. C., and Van Duyne, R. P., (1995), "Nanosphere Lithography: A Materials General Fabrication Process for Periodic Particle Array Surfaces," J. Vac. Sci. Technol. A, 13(3), p. 1553.

[6] Qu, C., and Kinzel, E. C., (2016), "Polycrystalline Metasurface Perfect Absorbers Fabricated Using Microsphere Photolithography," Opt. Lett., 41(15), pp. 3399–3402.

[7] Qu, C., and Kinzel, E. C., (2017), "Infrared Metasurfaces Created with Off-Normal Incidence Microsphere Photolithography," Opt. Express, 25(11), p. 12632.

[8] Wu, M.-H., and Whitesides, G. M., (2001), "Fabrication of Arrays of Two-Dimensional Micropatterns Using Microspheres as Lenses for Projection Photolithography," Appl. Phys. Lett., 78(16), pp. 2273.

[9] Sedao, X., Derrien, T. J.-Y., Romer, G. R. B. E., Pathiraj, B., and Huis in 't Veld, A. J., (2013), "Large Area Laser Surface Micro/nanopatterning by Contact Microsphere Lens Arrays," Appl. Phys. A, 111(3), pp. 701–709.

[10] Sedao, X., Derrien, T. J. Y., Romer, G. W. R. B. E., Pathiraj, B., and Huis In T Veld, A. J., (2012), "Laser Surface Micro-/nano-Structuring by a Simple Transportable Micro- Sphere Lens Array," J. Appl. Phys., 112(10), pp. 103111.

[11] Polushkin, N. I., (2005), "Direct Patterning of Magnetic Media via Focusing Light by Microsphere Arrays," Appl. Phys. Lett., 86(13), pp. 1–3.

[12] McLeod, E., and Arnold, C.B., (2008) "Subwavelength direct-write nanopatterning using optically trapped microspheres," Nature Nanotechnology, 3, pp. 413-417.

[13] Pan, H., Hwang, D. J., Ko, S. H., Clem, T. A., Frechet, J. M. J., Bauerle, D., and Grigoropoulos, C. P., (2010), "High- Throughput near-Field Optical Nanoprocessing of Solution- Deposited Nanoparticles," Small, 6(16), pp. 1812–1821.

[14] Lu, Y. F., Zhang, L., Song, W. D., Zheng. Y. W., and Luk'yanchuk. B. S., (2000) "Laser writing of a subwavelength structure on silicon (100) surfaces with particle-enhanced optical irradiation," J. Exp. Theor. Phys. Lett., 72(9), pp. 457–459.

[15] Li, X., Chen, Z., Taflove, A., and Backman, V., (2005), "Optical Analysis of Nanoparticles via Enhanced Backscattering Facilitated by 3-D Photonic Nanojets.," Opt. Exp., 13(2), pp. 526–533.

[16] O'Connell, C., Sherlock, R., and Glynn, T. J., (2010), "Fabrication of a Reusable Microlens Array for Laser-Based Structuring," Opt. Eng., 49(1), pp. 14201.

[17] Meng, X., and Qiu, D., (2014), "Gas-Flow-Induced Reorientation to Centimeter-Sized Two-Dimensional Colloidal Single Crystal of Polystyrene Particle.," Langmuir, 30(11), pp. 3019–3023.

[18] Zhang, X. A., Elek, J., and Chang, C. H., (2013), "Three- Dimensional Nanolithography Using Light Scattering from Colloidal Particles," ACS Nano, 7(7), pp. 6212–6218.

SECTION

2. CONCLUSION

This dissertation studied on microsphere photolithography, a scalable nanomanufacturing technique with three research objects: (1) generation of IR metausurfaces with various designs and elaborate IR performances using microsphere photolithography; (2) modeling of microsphere photolithography; (3) preliminary study on scaling the process using a reusable mask for future roll-to-roll configuration.

Microsphere photolithography is proposed as an easy, low-cost, and versatile tool for the manufacturing of metasurfaces. MPL enables the fabrication of metasurfaces with complex designs by using on/off normal illuminations and greymasks for hierarchical patterning. The size of the features scales with exposure dosages for IR metasurfaces. The illumination angle of incident can be tailored for creating complex micro-antenna elements that the photonic jet to be precisely steered around the unit cell defined by the microsphere. The ratio of the offset of the photonic jet to the microsphere diameter is shown to be independent of the size and orientation of the sphere lattice. The metasurfaces fabricated from microsphere photolithography are characterized: (1) the design of hexagonal-close-packed metal-insulator-metal absorber/emitter with metal disks as top layer achieves near unity absorptances in mid-wave infrared spectrum; (2) metasurface with split-ring resonator/tripole features show polarization dependent/independent performances; (3) the designs of multicavity/hybridizing silica phonon mode for achieving multiband/broadband metasurface in thermal infrared spectrum are shown. The yield of the process is improved to $>cm^2$ by self-assembly metrologies and better microspheres with $CV<2\%$. With a polycrystalline microsphere

array from the self-assembly, the polycrystalline metasurfaces have been proven to be robust in the presence of the lattice defects with a good agreement between simulation and experiment. The potential application of the IR metasurfaces includes but not limited to infrared cloaking, sensing, filtering, and energy harvesting.

The modeling of microsphere photoresist process is demonstrated and validated by experimental results. The model is based on the electromagnetic simulation of the photonic jet, photo-chemical kinetics and 3D cell-removal algorithm. For a given photoresist, the diameter of the hole features are co-dependent on the exposure dosage and development time. The minimum combination of exposure dosage/development time for through-photoresist holes can be determined through the models. The diameter of holes changes dramatically with small deviations of the process parameters around the time when the hole is through; the development duration is the main source of variation in the experiments. Thus, the combination of ultrathin photoresist, small exposure dosage, and long development time makes the sub-100 nm features available by MPL. The model is validated for off-normal incident illuminations as well. The modeling of MPL leads the fabrication of metasurfaces in a predicable way using microsphere photolithography.

Scaling microsphere photolithography using roll-to-roll is the long-term goal of this project. The preliminary experiment of using mask-based microsphere photolithography shows the possibility of this concept. The repeatability of the technique using a simple weight system, a flexible microsphere mask, and flexible substrates is evaluated for infrared metasurface absorbers created. The tape-based microsphere mask was re-used over 13 times and produces minimal deviations in the resonant wavelength

and maximum absorptance. The samples are scaled up to >cm^2. Future work is to scale the metasurfaces up further by improving the mask/microsphere adherence and contact uniformity for roll-to-roll fabrications.

APPENDIX A.

MATLAB CODE FOR SIMULATION OF MICROSPHERE PHOTOLITHOGRAPHY

The original Mack model [19] gives the simple development kinetics that the new concentration of the inhibitor m directly affects the development behavior by changing the development rate

$$R = R_{max} \frac{(a+1)(1-m)^n}{a+(1-m)^n} + R_{min}$$

where R_{max} denotes the maximum development rate for fully exposed photoresist; is the minimum development rate for the unexposed photoresist; refers to the diffusion rate constant; and represents the number of exposure or deblocking events that work together to get one resin molecule into solution. Assuming the development rate is reaction-controlled, meaning the diffusion is fast and less important, the constant . The equation above can be simplified as (5) in Paper V.

In the cell-removal algorithm, the 3D photoresist domain, which is investigated in FEM simulations of the E-field ratio distributions, is divided into brick volumes. For the models in paper V, cubic cells are used with edge length ΔL (5 nm). Each cell is represented by the corresponding location indices in the output matrix from HFSS simulation. The cells on the top and the bottom layers of the photoresist have the height of $\Delta L/2$. Same with the cells on the other four sides: the cells on the corresponding side has a length of $\Delta L/2$.

The E-field simulation results from HFSS are the input for the code. 3D matrices of *DOSE*, *R*, Q_v, and Q_s are defined with the same dimensions as photoresist domain analyzed in HFSS (discrete $M \times N \times O$ data points with the spacing of ΔL). The dose matrix *DOSE* is determined by equations (2)-(4) in paper V with the input. Then the development rate matrix *R* is obtained by implementing equation (6) in paper V.

The development status of the cells is defined by matrix Q_v which composes of '0' and '1' switches. Switch '1' means the cell is exposed to the developer and ready to be developed with its local development rate. '0' means the cell is not in contact with the developer. The switch of a cell in Q_v shifts from '0' to '1' when one or more neighboring cell is fully developed. The top layer of the photoresist is exposed to the developer first, so the original status of the switches of the cells on the top surface of the photoresist are set to '1', while the other cells have '0' in the Q_v matrix.

Q_s matrix is defined as the counter matrix. The counters for each cell show the percentage of the volume left during the development. The original status of all cells are 100%. For a given isotropic development rate R at a cell (a, b, c), the cell is subtracted by an amount from the counter in one time step Δt_{dev} :

$$Q_s(a,b,c,t+\Delta t_{dev}) = Q_s(a,b,c,t) - R(a,b,c)\times \Delta t_{dev} / \Delta L$$

A cell is defined as 'developed' when the corresponding counter reaches 0%. The developed cell resets the Q_v switches all of its neighboring cells to '1'.

Below is the MATLAB code for estimating the development for 260 nm photoresist under designated process parameters (exposure dosage of 1.14 mJ/cm^2 and development time of 20 seconds).

```
[fn,pn]=uigetfile('*.fld','Pick HFSS field result file');   % open UI to identify file
fpn=fullfile(pn,fn);                                         % concatenate filename and path
tic;                                                         % start timer
fid=fopen(fpn);                                              % set file identifier to fpn
fgetl(fid); fgetl(fid);                                      % load and discard the 1st two
lines (header)
[data, count]=fscanf(fid,'%f',inf);                          % read remainder of file and store
in data
fclose(fid);                                                 % close file
```

```
mn=[-540 -540 -260]; mx=[540 540 0]; sp=[5 5 5];       % define minimum, maximum,
and spacing

M=1+(mx(1)-mn(1))/sp(1); N=1+(mx(2)-mn(2))/sp(2); O=1+(mx(3)-mn(3))/sp(3);  %
number of points in x, y, and z
x=mn(1):sp(1):mx(1); y=mn(2):sp(2):mx(2); z=mn(3):sp(3):mx(3);          % define
vectors for x, y, and z

for a=1:M                                          % step over x
   for b=1:N                                       % step over y
      for c=1:O                                    % step over z
         E(a,b,c)=data(4*((a-1)*N*O+(b-1)*O+(c-1))+4);              % store data
in MxNxO array E
      end
   end
end
fprintf('File: %s loaded in %f s\n',fn,toc);       % report time to load file

E=E.^2;                                            % square E field data
Ex=E;                                              % create dose array proportionate
to E^2
Ex(isnan(Ex))=0;                                   % set NaN values to 0 in
exposure array
Qs=ones(size(E));                                  % create exposure array (fraction
of resist remaining)
Qs(:,:,O)=0.5;
Qs(:,:,1)=0.5;                                     % cells at top and bottom layer
have counter of 0.5

rmax=63;                                           % fitted number, Max
development rate
C=0.032;                                           % Dill parameter (exposure rate
constant)
t=0;                                               % initialize time
dt=0.0125;                                         % time step [s]

absinten=10;                                       % intensity of light source
[mW/cm2]
extime=0.114;                                      % exposure duration
DOSE=absinten*extime;                              % exposure dosage
n=1.8;                                             % fitted number, number of
exposure events that work together to get one resin into solution
er=rmax*((1-exp(-Ex.*C*DOSE)).^n);                 % exposure rate
Qv=zeros(size(Ex));                                % array describing region exposed
to developer
Qv(:,:,O)=1;                                       % top surface is initially exposed
```

```
h=ones(N,M)*mx(3);                              % initialize height array
figure;                                         % colormap jet;
subplot(3,1,1);
DMp=surf(x,y,h);
set(DMp,'linestyle','none'); caxis([mn(3) mx(3)]);
axis image; view(2); colorbar;
axis([mn(1), mx(1), mn(2), mx(2)]);
xlabel('x [nm]'); ylabel('y [nm]'); grid off;

subplot(3,1,2);
x_ln=line('xdata',x,'ydata',zeros(size(x)),'color',[0,0,1]);
axis image; axis([mn(1),mx(1),mn(3),mx(3)]);
xlabel('x [nm]'); ylabel('h [nm]');

subplot(3,1,3);
y_ln=line('xdata',y,'ydata',zeros(size(y)),'color',[1,0,0]);
axis image; axis([mn(2),mx(2),mn(3),mx(3)]);
xlabel('y [nm]'); ylabel('h [nm]');

tic;
q=1;
while t<20                                      % development time
   for a=1:M
      for b=1:N
         for c=1:O
            if (Qv(a,b,c)>=1)&&(Qs(a,b,c)>=0)          % Switch on and counter is above
0
               if (a<=M-1)&&(a>1)&&(b<=N-1)&&(b>1)&&(c<=O-1)&&(c>1);

                  Qs(a,b,c)=Ds(a,b,c)-er(a,b,c)*dt/sp(3); % if the cell is not on the side of
the domain, development rate*1

               if Qs(a,b,c+1)==0&&Qs(a-1,b,c)==0
                  Qs(a,b,c)=Qs(a,b,c)-er(a,b,c)*dt*sqrt(2)/sp(3); % two faces of cell is
exposed to developer, developer rate*sqrt(2);

               end
               if Qs(a,b,c+1)==0&&Qs(a+1,b,c)==0
                  Qs(a,b,c)=Qs(a,b,c)-er(a,b,c)*dt*sqrt(2)/sp(3); % two faces of cell is
exposed to developer, developer rate*sqrt(2);

               end
               if Qs(a,b,c+1)==0&&Qs(a,b-1,c)==0
                  Qs(a,b,c)=Qs(a,b,c)-er(a,b,c)*dt*sqrt(2)/sp(3); % two faces of cell is
exposed to developer, developer rate*sqrt(2);
```

```
            end
            if Qs(a,b,c+1)==0&&Qs(a,b+1,c)==0
              Qs(a,b,c)=Qs(a,b,c)-er(a,b,c)*dt*sqrt(2)/sp(3); % two faces of cell is
exposed to developer, developer rate*sqrt(2);

            end
            if Qs(a,b,c+1)==0&&Qs(a-1,b,c)==0&&Qs(a,b-1,c)==0
              Qs(a,b,c)=Qs(a,b,c)-er(a,b,c)*dt*sqrt(3)/sp(3); % three faces of cell is
exposed to developer, developer rate*sqrt(3);

            end
            if Qs(a,b,c+1)==0&&Qs(a-1,b,c)==0&&Qs(a,b+1,c)==0
              Qs(a,b,c)=Qs(a,b,c)-er(a,b,c)*dt*sqrt(3)/sp(3); % three faces of cell is
exposed to developer, developer rate*sqrt(3);

            end
            if Qs(a,b,c+1)==0&&Qs(a+1,b,c)==0&&Qs(a,b-1,c)==0
              Qs(a,b,c)=Qs(a,b,c)-er(a,b,c)*dt*sqrt(3)/sp(3); % three faces of cell is
exposed to developer, developer rate*sqrt(3);

            end
            if Qs(a,b,c+1)==0&&Qs(a+1,b,c)==0&&Qs(a,b+1,c)==0
              Qs(a,b,c)=Qs(a,b,c)-er(a,b,c)*dt*sqrt(3)/sp(3); % three faces of cell is
exposed to developer, developer rate*sqrt(3);

            end
           else Qs(a,b,c)=Qs(a,b,c)-er(a,b,c)*dt/sp(3);   % if the cell is on the side of the
domain, development rate*1

            end

         end


            if Qs(a,b,c)<0                          % Counter less than or equal to 0,
cell removed
               Qs(a,b,c)=0;
               h(a,b)=min([h(a,b),z(c)]);           % thickness defined
               Qv(a,b+1,c)=1;                       % switch on for neighboring cells
               Qv(a+1,b,c)=1;
               Qv(a,b,c+1)=1;
               if a>1
                  Qv(a-1,b,c)=1;
               end
               if b>1
                  Qv(a,b-1,c)=1;
```

```
                end
                if c>1
                   Qv(a,b,c-1)=1;

                end
             end
          end
       end
    end
  end
  set(DMp,'zdata',h,'Cdata',h); drawnow;
  set(x_ln,'ydata',h(:,round(M/2)));
  set(y_ln,'ydata',h(round(N/2),:));
  EA(q,:)=[t,sum(sum(h==mn(3)))];

  t=t+dt; q=q+1;
end
DD1=sqrt(EA(:,2)*sp(1)*sp(2)*4/pi);                    % diameter calculation

fprintf('Development simulation: %f s\n',toc);
```

The dosage ratio along the centerline is regarded as constant for a particular thickness of the photoresist. The ratio is fitted as

$$R_E\big|_{x=y=0}(h) = 355.5\sin(0.003271h + 1.502) + 314.3\sin(0.003976h + 4.539) + 20.66\sin(0.007914h + 6.496)$$
$$+0.8687\sin(0.04695h - 4.618)$$

The ratio along the centerline is ~56 when 120 nm photoresist is applied.

The amplitude A and standard deviation s in the dosage ratio equation (9) are also determined by the thickness of the photoresist. The R_E is presented as

$$R_E\big|_{y=0,z=-h}(h) = (52.61\sin(0.005018h + 0.5693) + 30.3\sin(0.00997h + 2.879) + 10.53\sin(0.0165h + 4.533) +$$
$$1.718\sin(0.03411h - 0.2915)) \cdot e^{-x^2 / [(231.5\sin(0.004687h+0.8899)+127.9\sin(0.009085h+3.036)+68.88\sin(0.02002h+3.391)+50.33\sin(0.022h+5.976))]^2}$$

For h=120 nm photoresist, $R_E = 25.45795\,e^{-\frac{x^2}{127.3373^2}}$.

Even the sub-100 nm features are observed for smaller E_{exp} with comparatively longer t_{dev} (left side of the map) and higher E_{exp} with shorter t_{dev} (right side of the map) in Figure 5(c), they can be difficult to be achieved in actual fabrications because of sensitivity issues. As an example shown in Figure 5 (b), for the exposure dosage of 1.73 mJ/cm^2, sub-100 nm hole is observed at 3-second of development, but it increases to over 200 nm in the next second. Therefore, sub-100 nm holes are difficult to be obtained for high exposure dosages in the experiments with imprecise time control in puddle development mode. On the other hand, the development time needed for small exposure dosages for a through-hole is comparatively long and better controlled. For example, the minimum duration needed for 0.42 mJ/cm^2 dosage is ~12.5s, but the sensitivity is much lower (~30 nm/s). In Figure 5(a), the hole is shown as small as 10 nm at 12.5s of development. At 14 seconds, the diameter of the hole is ~86 nm. Although the hole becomes >300 nm when the development time exceeds 30s, the 1.5s error window is allowed for the fabrication of sub-100 nm holes with the conditions. The hole at 12.5s is not suitable for pattern transfer because the sidewall angle for the hole is high. Vertical sidewalls of the holes for pattern transferring are formed as the development reaches 14s.

The error of the diameter of the holes in a hole array potentially comes from three aspects: the variance in exposure dosage ΔE_{exp}, development time Δt_{dev}, and thickness of photoresist Δh. The total difference of diameter ΔD can be expressed as

$$\Delta D = \sqrt{\left(\Delta E_{exp}\left(\frac{dD}{dE}\right)\right)^2 + \left(\Delta t_{dev}\left(\frac{dD}{dt}\right)\right)^2 + \left(\Delta h\left(\frac{dD}{dh}\right)\right)^2}$$

The errors in diameter caused in the experiments (E_1= 0.42 mJ/cm^2, t_{dev1}=15s; E_2= 1.73 mJ/cm^2, t_{dev2}=3s) are estimated. In the experiments, a spatial variation of the intensity of the light source is measured as <1 mW/cm^2 among >25 cm^2 illumination area. For the exposure dosage of E_1= 0.42 mJ/cm^2, the t_{exp} needed is only 0.03s. With the average sensitivity of ~96.5 nm/[mJ/cm^2], the total error caused by this exposure dosage justified as 2.895 nm. On the other hand, the t_{exp} needed for the dosage of E_2= 1.73 mJ/cm^2 is 0.12s. With a much lower sensitivity of 23.56 nm/[mJ/cm^2], the error caused by exposure is 2.827 nm. Assuming the variance of development duration is 1 second, the error caused by development time are 31 nm and 68 nm for E_1 and E_2, respectively. If the variance of the thickness of photoresist is negligible, the total variance for applied E_1 and E_2 and corresponding development durations are 31.13 nm and 68.06 nm, respectively.

APPENDIX B.

CONSTRAINED SELF-ASSEMBLY OF MICROSPHERES

Two-dimensional (2D) Hexagonal Close Packed (HCP) micro particle arrays come from self-assembly, a bottom-up approach. These particle arrays are applied as pattern templates in the micro/nano fabrication field, such as Nanosphere Lithography (NSL) [10], hole-mask colloidal lithography [30], Microsphere Photolithography (MPL) [31]. In NSL and hole-mask colloidal lithography, the particles act as a shadow/etch mask; the pattern of the interstices between the spheres are transferred onto substrates by vapor deposition or etching. While in MPL, the microspheres are used as micro ball-lenses to focus flood illuminated light to sub-diffraction limited photonic jets [12] to expose a layer of photoresist underneath.

The self-assembly of microspheres is a critical link in MPL process. The goal of self-assembly for these techniques is to create a large-area, single-crystalline monolayer of HCP sphere array. Common methods for the self-assembly of dielectric particles are separating the solid particles into liquid solution, and the particles can reorder when the liquid solvent goes away. Techniques for improving the dielectric particles to self-assemble into 2D HCP arrays are discussed in previous studies, such as drop-coating [32], spin-coating [33, 34], Langmiur-Blodgett method [35], convective assembly [36, 37], air-water-interface (AWI) [38], and assembly through a wedge cell [39]. Spin-coating relies on increasing evaporating rate of water on a rotating surface; however, the strong rotational force and its radial gradient of spin-coating overpower the forces behind the formation of large single crystalline domains [40]. Drop coating uses a drop of the particle suspension with a given volume and composition onto substrate. Drop-coating is simple, but the area of deposition is sporadic and limited. Convective self-assembly is promising for the creation of large-area monolayer HCP arrays by using a blade to

control the spheres, but it need high precision control between the blade and the substrate, resulting in the demand for costly of the equipment. For the three techniques mentioned above, the particles all attached on prepared solid planar substrates during the self-assembly process.

Langmiur-Blodgett (L-B) and AWI are different approaches with respect to the substrate. They require particles to self-assemble on liquid substrate as air-water or air-oil [41] interface by capillary force; this enables the particle arrays to transfer onto other types of substrates. Particle arrays have been transferred onto curved substrates such as copper wire [23] and fiber [42]. L-B method uses a trough with sliding bars pushing the particles closer. On the other hand, the motion of the particles on the water surface is controlled by capillary force [43] in the AWI technique. AWI is very promising for facile and efficient creation of large area HCP particle arrays for microsphere photolithography. At air-water interface, the liquid solvent of the particle-liquid mixture is deformed between microspheres when proper height of the solvent layer is achieved. When a concave meniscus is formed in between particles, the capillary force exhibits attraction effect. A two-stage mechanism of particle array self-assembly is proposed in [32] as a widely recognized theory. Stage I is the formation of an ordered nucleus in the assembly process. This happens due to the deformation formed as the height h of the solvent decreases below the sphere diameter p (partially immersing the particles) in the area, and the transport is caused by water/liquid evaporation from meniscus between clustered particles. The formation of the nucleus triggers the Stage II. This is when the crystal starts to grow through directional motion of particles towards the nucleus in order. N_2 can be used for blowing over the surface to provide the energy required for the

spheres to reorganize themselves into a single 2D colloidal crystal (effectively melting smaller domains and allowing them to recrystallize). This approach has demonstrated transferring cm^2 scale single crystals to glass slides and even cylindrical surfaces [23].

The purpose of the solvent is to help the particles float on the liquid substrate (water). The particles are mixed into solvent and the mixture is dispensed onto water surface. The solvent functions as a secondary thin film on the water and the particles are only in this 'second layer'; the particles self-assemble when the secondary liquid has the proper height. The solvent has to satisfy several requirements: lower density than water, immiscible with water, hydrophilic on water, non-toxic, and friendly with the dielectric particles mixed in it. An appropriate hydrophobicity of the particle to the liquid is needed to form a highly ordered monolayer [38]. Chloroform, ethanol, and butanol are mentioned in literature as solvent for different particles [44].

The concentration of particles in the mixture affects the self-assembly by tailoring the height h of the secondary layer: higher concentration corresponds to a lower liquid layer for the spheres to assemble in. The height h of the secondary layer can be estimated by the concentration of the spheres in the mixture. As the mechanism indicates, the particles self-assemble into orderly 2D arrays when the thickness of the solvent layer h is lower or equal to the diameter of the particles, so a proper concentration of the particles in the mixture is needed. The area of the single crystalline array of the particles on air-water interface are reported to be improved by re-crystallizations of the polycrystalline arrays by gas-flow [23] and solvent-vapor-annealing [45].

Dip-coating method can be used for transferring the crystal arrays [32] by vertically pulling the substrate from water surface. In this method, the withdraw speed is

determined by the sphere concentration and the feed rate of the colloidal solutions [38]. The particle arrays can also be transferred onto a substrate that placed horizontally underneath water surface when water is drained out [41, 46]. However, it could take longer for the water over substrate to evaporate.

The lift-off method for transferring the microsphere arrays from AWI is discussed with respective to two important parameters: angle of deposition Φ, and lift-off speed r, as shown in Figure B1. Samples are created to see what effect increasing the angle of deposition would have on the samples. The deposition angle is defined as the angle between the backside of the substrate being deposited and the water surface. The range of the angle in the test is from 10° to 130°. As can be seen in Figure B2, higher angles for deposition have less defective area than samples at lower angles. There seems to be a distinct separation at 80°, after which samples have less than 25% defective area. The defective area is defined as the area with multilayers/voids. All of the samples were made with 400 mg/mL and a lift speed of 0.02 mm/s. As shown above, there is a dramatic improvement at 90° deposition angle, and also is it possible at angles greater than 90°.

Microsphere deposition improves as the angle of the substrate increases, but also up to a certain point. Angles higher than 130° result in patchy areas. At 90°, the quality of the samples improves slightly when the lift speed is increased incrementally from 0.02 mm/s to 0.1 mm/s (as shown in Figure B3). At high angles of deposition, instead of seeing the defects split relatively evenly between the patches of spheres and small groups of spheres, the defective area can be mostly attributed to the small aggregation of spheres due to inappropriate mixing.

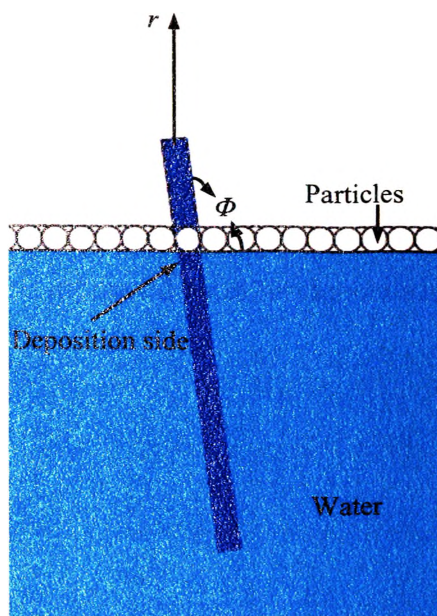

Figure B1. Scheme of transferring the self-assembled particle arrays by pulling-off.

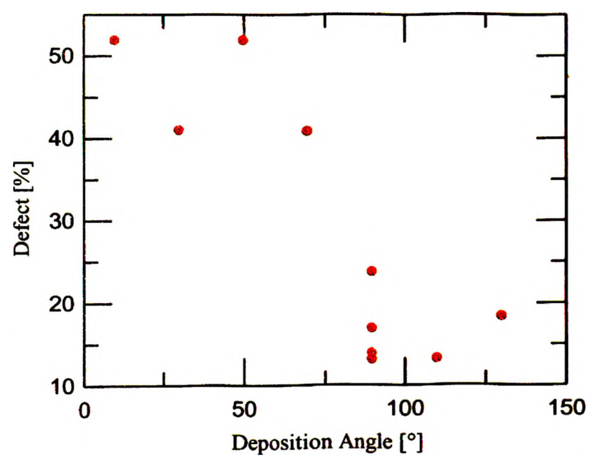

Figure B2. Angle of Deposition vs Defective Area Percentage.

Figure B3 shows the defect percentage of the microsphere array transferred onto the substrate versus lift-off speed at the deposition angle of 90°. The faster lift speeds had less area that had multilayers or other defects. The amount of bad areas spiked up as the assembled microsphere array cannot deposit on the substrate fast enough to keep up with the lift speed. Increasing the lift speed used for deposition improves the sample quality up to a certain point.

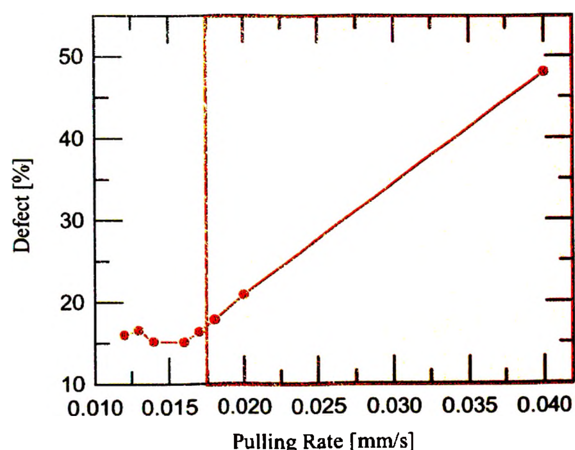

Figure B3. Lift Speed (mm/s) vs Defective Area Percentage for 200 mg/mL at 90°.

The area to the right of the red shadow indicates lift speeds for which the microsphere array is filled with voids. As shown in the Figure, 0.016 mm/s is the fastest a sample can be lifted from the solution under the current conditions.

We use a modified AWI technique for preparing the sphere array by confining the deposition area for creation of metasurfaces using microsphere photolithography in this

dissertation. Monodispersed silica and polystyrene particles can be chemically synthesized following well-established processes in [22] and [23], respectively. They are widely available commercially, with different sizes and materials (notably polystyrene and fused silica) at reasonable costs ($30/g). While polystyrene/silica is adequate for experimentation in the near-UV, pushing into the deep UV requires silica microspheres because the polystyrene is absorbing deep UV during illumination. Most substrates used for particle depositions mentioned in literature are planar and hydrophilic glass slides [33-38]. The photoresist used in the photolithography process is hydrophobic as the contact angle is as steep as 80 degrees [37]. This causes a problem with transferring particles when the substrate is vertically pulled out from the water (dip coating) because the particles cannot be attached to the substrates. To solve this problem, the substrate can be positioned horizontally under the water surface, and the particle array can fall onto the hydrophobic substrate as the water is drained.

In the experiments for the papers, we use regular O-rings with variable areas designed on top of substrate as a confined deposition area, and DI water is filled inside the O-rings. Microsphere solutions are dripped onto the water surface and started to self-assembly spontaneously with the calculated number of microspheres and thickness of liquid layer applied. The microsphere array will be transferred onto the substrate after water subphase is drained. Figure B4 shows the assembling and transferring process.

In actual deposition process, silica microspheres (NanoCym) with p=2.7 μm (nominal, polydispersity 0.005) in diameter were deposited on the photoresist. 1-Butanol is used as solvent for silica microspheres for two reasons: first, butanol is barely immiscible with water, and it is less dense so that the microspheres float in the air-

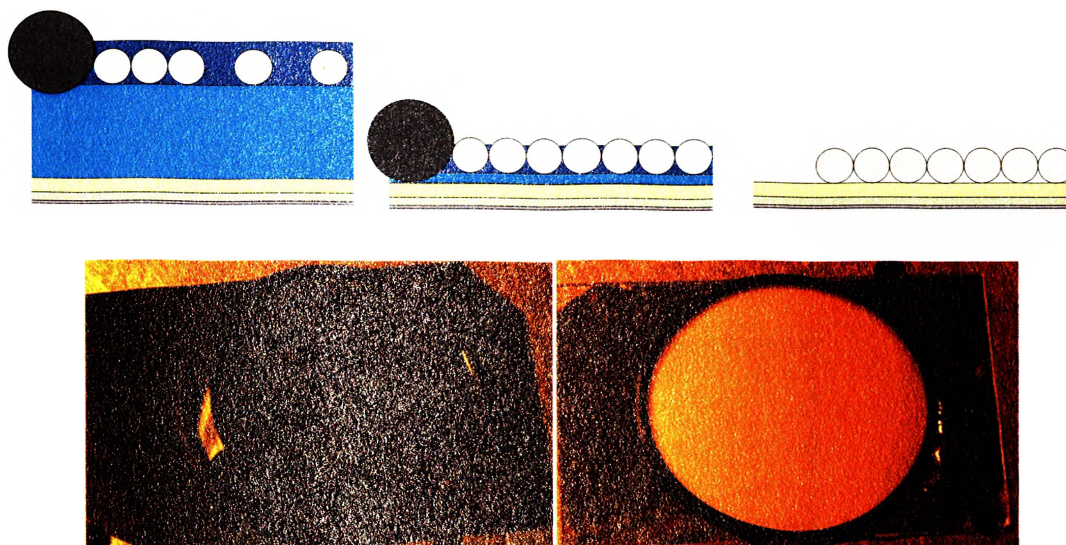

Figure B4. Schematic of self-assembly of microspheres on constrained area of air-water interface.

water interface; second, it is also friendly to silica. Surfactant (SDS) (30 mg/L) is also needed in the mixture to reduce the surface tension of water. Ultrasonication is for breaking up clumps formed in sphere solutions. A sonication duration of multiple hours is mentioned in [38], 30 minutes' ultrasonication is used in our experiments.

Then the weight percentage of microspheres in solution and volume of solution applied to the water surface are determined. The confined coating area A determines the number of spheres N needed for hexagonally close packed microspheres

$N = A/(\sqrt{3}p^2/2)$.

Given density of silica microspheres, the mass of spheres needed can be calculated. According to the principle of spontaneous assembly of microspheres by immersion capillary forces, the height of butanol layer h should be less than or equal to the diameter of microspheres p. The total volume applied on the water surface is

determined by $h \times A$. The volume of liquid can be subtracted from the total volume to determine the volume of spheres. Then the weight percentage of spheres in butanol/SDS surfactant can be determined. After the microsphere solution is mixed, it goes through ultrasonication for 10 minutes. When the concentration is too low, the particles gradually assemble in sparse patches as the suspension is dispensed onto the water surface. The suspension concentration needs to be increased for the sphere deposition area to become larger. At the same time, the volume of solvent builds up, which makes the assembly process longer and more complex.

The calculated volume of sphere solution is drawn in by a microsyringe and then dispensed onto the DI water in the O-ring. The microspheres suspended in the solvent spread over the confined area and self-assemble instantaneously due to immersion capillary force, which is generated by a thin deformed liquid layer in between spheres [29]. After the DI water and solvent drain and evaporate, the microsphere array is deposited on the substrate. Ideally, the microspheres are self-assembled into hexagonal closed packed in a crystalline way and then transferred to the substrate.

Figure B5 shows the defect percentage dependence on h/p with fixed deposition area and number of microspheres for three different sizes of microspheres. The curves show that for each size of microsphere, the lower of height/diameter ratio is, the better assembly of the microsphere array can be. The defect percentage increases dramatically when the ratio exceeds unity meaning that the height is over diameter and the three dimensional Brownian motion drives the formation of multilayer and voids.

In the current way of self-assembly, we have achieved microsphere arrays over 25 cm^2. The area of single crystalline of the microsphere array is limited by the baseline of

the size variation of the commercial silica microspheres (5% for 1.5 um and 15% for 2.0 and 2.7 um) for this particular vendor.

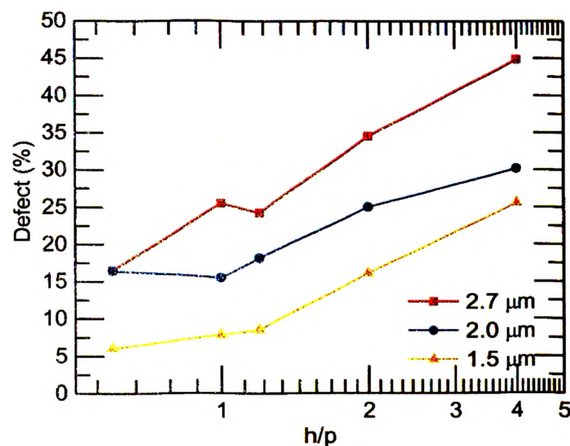

Figure B5. Scalable monolayer microsphere array versus thickness of butanol layer *h/p*.

The effect of quality of microspheres is important as illustrated in the previous paragraphs. Work with better microspheres is also conducted as used for the papers from IV to VI. The coefficient of variation (CV) is only 2% for 2 μm silica microspheres for new experiments. With the new microspheres giving a defective area percentage, it is easy to get a decent monolayer. The difficulty now is getting the crystal size to increase, which we believe is due to the high surface tension of the DI water. Some potential ideas to make this happen are adding something to the DI water to change its properties (soap/detergent/salt/SDS/butanol), or adding a layer of pure butanol on the DI water before injecting the sphere solution.

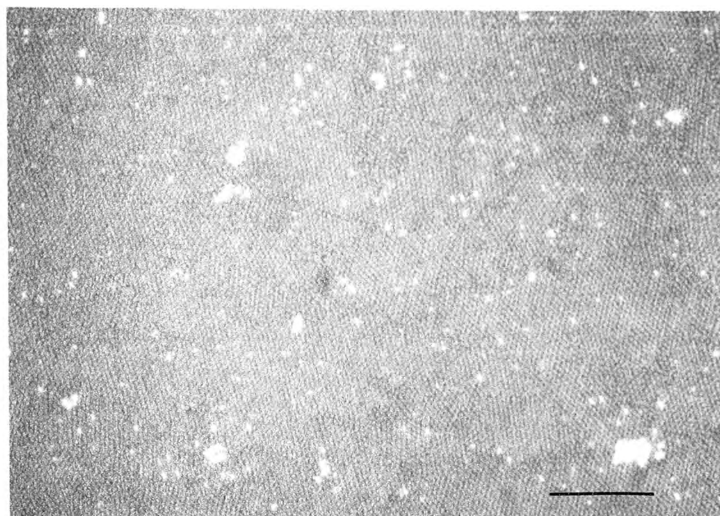

Figure B6. Deposition using only DI water as the liquid of the AWI. Scale bar: 40 μm.

Initially, microsphere deposition occurred using solely DI water for the base of the AWI (as shown in Figure B6), but it was thought that adding some other substances to the DI water might change the properties of the deposition. When the microspheres were added to the water surface, it was noted that the spheres spread across the surface rapidly. When this happens, the microspheres might not have enough time to assemble into the lowest-energy configuration, hexagonal close-packed. If this is the case, lowering the surface tension of the water might improve the crystal size and packing structure. The whitish areas on the image are most likely sphere clumps that are not separated by ultrasonication.

Greyscale microscope images Figure B7 showing the microsphere crystals by adding more SDS surfactant (~100g/mL) into the solution. The crystal size does not change significantly, but there are fewer multilayer defects. The multilayer area is less than 1% with proper initial Butanol height.

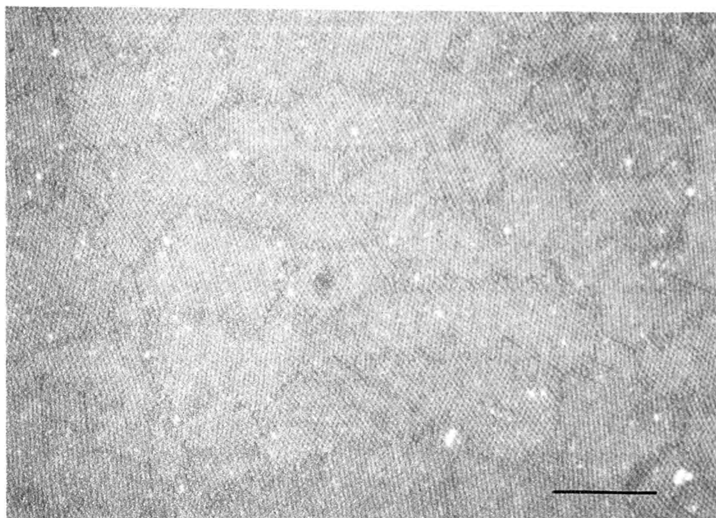

Figure B7. Deposition using SDS in DI water as the liquid of the AWI. Scale bar: 40 μm.

Figure B8 shows the microscope image of the microsphere array self-assembled on water with glass cleaner (main ingredient as Isopropyl Alcohol). Noticeably larger crystal size is observed among the sample.

Figure B9 exhibits the deposition using salt in DI water as the liquid of the AWI. Salt increases the density of the water subphase which helps with the floating. Adding more salt reduced crystal size and increased the white patches present, seemingly confirming the theory that the white patches are deposited salt. The white salt crystals are not avoidable when using the O-ring for placing the substrate horizontally and draining the water.

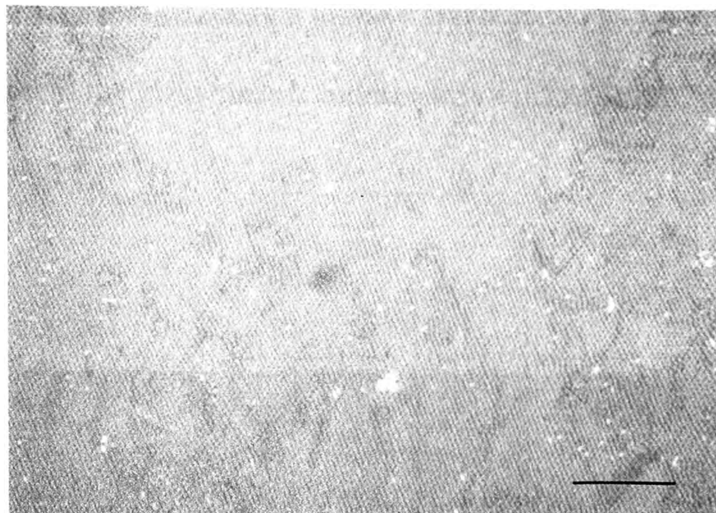

Figure B8. Deposition using glass cleaner in DI water as the liquid of the AWI. Scale bar: 40 μm.

Soap was settled on as the substance that showed the most improvement. When soap is added to water, the surface tension of water is lowered. This is because soap molecules are negatively charged on one end, so the intermolecular forces between water molecules are weakened. With soap contributing significantly to the quality of deposition, testing was done to see how effective increasing the concentration of soap/glass cleaner/Windex in the DI water. With the Teflon cup holding approximately 250 mL of water, small amounts of glass cleaner were added. Initially, 0.5 mL of glass cleaner was added, and then 1 mL, then 2 mL, and the concentration continued to increase by 1 mL until the spheres no longer resided on the AWI and fell into the liquid below.

The grain size of the samples seemed to increase with the concentration of the soap, and can be seen just by looking at the samples with the naked eye. The higher concentrations of soap produced more mirror-like microsphere assemblies. See the

images in Figures 10-12 for microscope images of the glass cleaner concentration tests. As the concentration of the glass cleaner increases to 4 mL/250 mL, the crystal size is maximized.

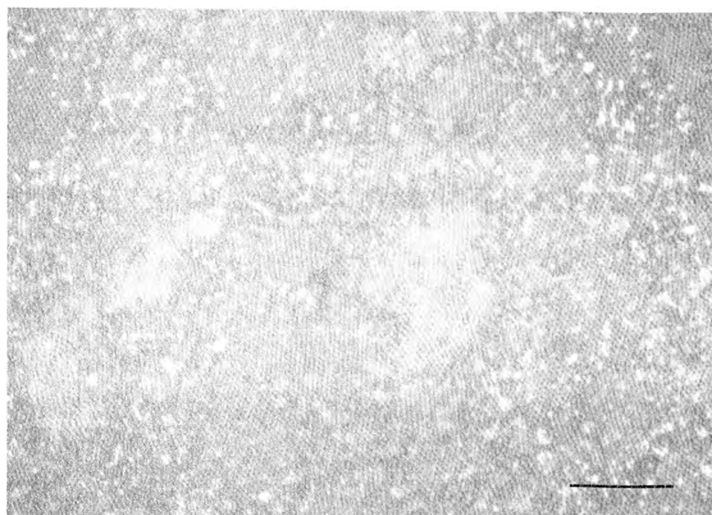

Figure B9. Deposition using salt in DI water as the liquid of the AWI. There are white patches present after this deposition that were not seen using any other liquid mixture. Scale bar: 40 µm.

With the optimized recipe with concentration of microsphere, surfactant, deposition angle, and lift-off speed, samples are created and characterized. Figure B13 shows the SEM image (a), optical image (b), and the diffraction pattern (c) of the sample showing the single crystals of the microsphere arrays formed on the substrate. The characterization indicates that the area of single crystal on the samples is as large as cm^2.

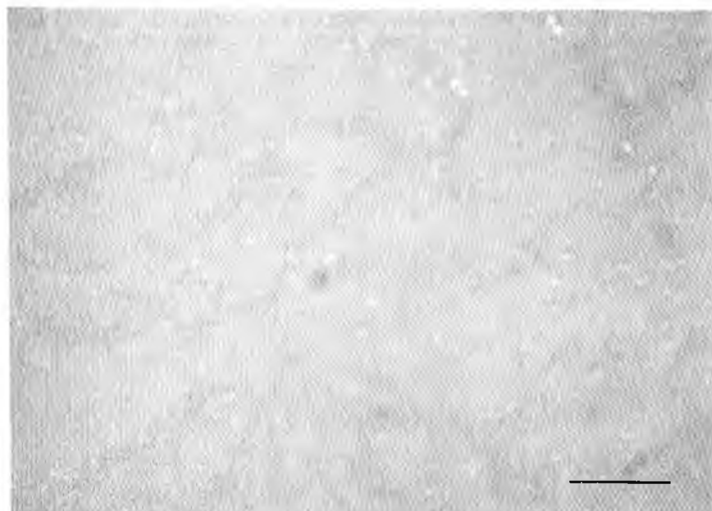

Figure B10. Sample using 0.5 mL of glass cleaner with 250 mL DI water. Scale bar: 40 μm.

Figure B11. Sample using 3 mL of glass cleaner in 250 mL DI water. Scale bar: 40 μm.

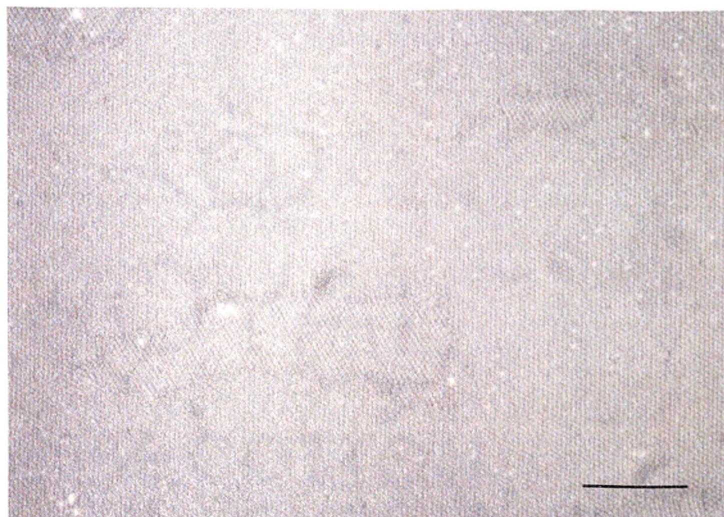

Figure B12. Sample using 4 mL of glass cleaner in 250 mL of DI water. Scale bar: 40 μm.

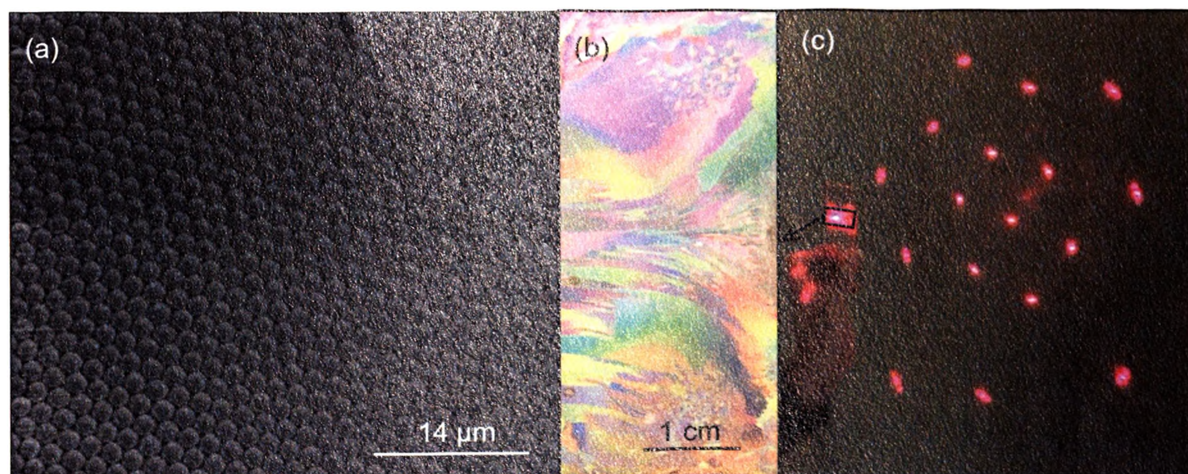

Figure B13. Polycrystalline microsphere array from self-assembly (a) SEM image of single crystal area of microsphere array (b) Far-field optical image (c) diffraction pattern illuminated with a He-Ne laser beam.

BIBLIOGRAPHY

[1] J. Valentine, S. Zhang, T. Zentgraf, E. Ulin-Avila, D.A. Genov, G. Bartel, X. Zhang, "Three-dimensional optical metamaterial with a negative refractive index," Nature, **455** (2008).

[2] B. A. Munk, Frequency Selective Surfaces Theory and Design (John Wiley & Sons, 2000).

[3] R. Adato, H. Altug "In-situ ultra-sensitive infrared absorption spectroscopy of biomolecule interactions in real time with plasmonic nanoantennas," Nature Communications, **4**(2) (2013).

[4] E. Rephaeli, A. Raman, S. Fan, "Ultrabroadband Photonic Structures To Achieve High-Performance Daytime Radiative Cooling," Nano Lett. **13** (2013).

[5] A.K. Azad, W.J.M. Kort-Kamp, M. Sykora, N.R. Weisse-Bernstein, T.S. Luk, A.J Taylor, D.A.R. Dalvit, H-T. Chen, "Metasurface Broadband Solar Absorber," Sci. Reports, **6**, 20347 (2015).

[6] A. Greenwald, J. Ryu, Y. Liu, R. Biswas, J. Ok, H. Youn, M. Kwak, M.-G. Kang, and L. J. Guo, "Roll-to-Roll Nanoimprinting Metamaterials," MRS Proc. 1412, mrsf11-1412-ff01-04 (2012).

[7] B. Lahiri, A. Z. Khokhar, R. M. De La Rue, S. G. McMeekin, and N. P. Johnson, "Asymmetric split ring resonators for optical sensing of organic materials," Opt. Express **17**(2), (2009).

[8] Y. Zhang, L. Zhou, J. Q. Li, Q. J. Wang, and C. P. Huang, "Ultra-broadband and strongly enhanced diffraction with metasurfaces," Sci. Rep. **5**(1), 10119 (2015).

[9] I. B. Divliansky, A. Shishido, I.-C. Khoo, T. S. Mayer, D. Pena, S. Nishimura, C. D. Keating, and T. E. Mallouk, "Fabrication of two-dimensional photonic crystals using interference lithography and electrodeposition of CdSe," Appl. Phys. Lett. **79**(21), (2001).

[10] J. C. Hulteen and R. P. Van Duyne, "Nanosphere lithography: a materials general fabrication process for periodic particle array surfaces," J. Vac. Sci. Technol. A **13**(3), (1995).

[11] S. Cataldo, J. Zhao, F. Neubrech, B. Frank, C. Zhang, P.V. Braun, H. Giessen, "Hole-Mask Colloidal Nanolithography for Large-Area Low-Cost Metamaterials and Antenna-Assisted Surface-Enhanced Infrared Absorption Substrates," ACS Nano, **6**(1) (2012).

[12] X. Li, Z. Chen, A. Taflove, and V. Backman, "Optical analysis of nanoparticles via enhanced backscattering facilitated by 3-D photonic nanojets," Opt. Express **13**(2), (2005).

[13] M. S. Kim, T. Scharf, S. Mühlig, M. Fruhnert, C. Rockstuhl, R. Bitterli, W. Noell, R. Voelkel, and H. P. Herzig, "Refraction limit of miniaturized optical systems: a ball-lens example," Opt. Express **24**(7), (2016).

[14] W. Wu, A. Katsnelson, O.G. Memis, H. Mohseni, "A deep sub-wavelength process for the formation of highly uniform arrays of nanoholes and nanopillars," Nanotechnology, 18 485302 (2007).

[15] W. Wu, D. Dey, O.G. Memis, A. Katsnelson, H. Mohseni, "A Novel Self-aligned and Maskless Process for Formation of Highly Uniform Arrays of Nanoholes and Nanopillars," Nanoscale Res. Lett., 3 123, (2008).

[16] W. Wu, D. Dey, A. Katsnelson, O.G. Memis, H. Mohseni, "Large areas of periodic nanoholes perforated in multistacked films produced by lift-off," J. Vac. Sci. Technol. B, 26 (2008).

[17] A. Bonakdar, S. J. Jang, R. L. Brown, M. Rezaei, and H. Mohseni, "Deep UV microsphere nanolithography to achieve sub-100 nm feature size," *Proc. of SPIE*, **9170**, 917016 (2014).

[18] A. Bonakdar, S.J. Jang, H. Mohseni, "Novel high-throughput and maskless photolithography to fabricate plasmonic molecules," J. Vac. Sci. Technol. B 32(2) 20604 (2014).

[19] C. Mack, *Fundamental Principles of Optical Lithography: The Science of Microfabrication,* Wiley, (2007).

[20] R. E. Jewett, P. I. Hagouel, A. R. Neureuther, and T. Van Duzer, "Line-profile resist developement simulation techniques," Polym. Eng. Sci. **17**, 381–383 (1977).

[21] C. A. Mack, "PROLITH: a comprehensive optical lithography model," in *Optical Microlithography IV* (International Society for Optics and Photonics, 1985), Vol. 538, pp. 207–221.

[22] W. Stober, A. Fink, "Controlled growth of monodisperse silica spheres in the micron size range," J. Colloid Interface Sci., 26 (1968).

[23] X. Meng, D. Qiu, "Gas-Flow-Induced Reorientation to Centimeter-Sized Two-Dimensional Colloidal Single Crystal of Polystyrene Particle," Langmuir, **30** (2014).

[24] N. Denkov, O. Velev, P. Kralchevski, I. Ivanov, H. Yoshimura, and K. Nagayama, "Mechanism of formation of two-dimensional crystals from latex particles on substrates," Langmuir 8, 3183–3190 (1992).

[25] Y. Cheng, P. G. Jönsson, and Z. Zhao, "Controllable fabrication of large-area 2D colloidal crystal masks with large size defect-free domains based on statistical experimental design," Appl. Surf. Sci. 313, 144–151 (2014).

[26] B. G. Prevo and O. D. Velev, "Controlled, Rapid Deposition of Structured Coatings from Micro- and Nanoparticle Suspensions," Langmuir 20, 2099–2107 (2004). (rapid convective assembly)

[27] T. Muangnapoh, A. L. Weldon, and J. F. Gilchrist, "Enhanced colloidal monolayer assembly via vibration assisted convective deposition," Appl. Phys. Lett. 103, (2013).

[28] M. Shishido and D. Kitagawa, "Preparation of ordered mono-particulate film from colloidal solutions on the surface of water and continuous transcription of film to substrate," Colloids Surfaces A Physicochem. Eng. Asp. 311, 32–41 (2007).

[29] P. A. Kralchevsky and K. Nagayama, "Capillary forces between colloidal particles," Langmuir 10, 23–36 (1994).

[30] H. Fredriksson, Y. Alaverdyan, A. Dmitriev, C. Langhammer, D. S. Sutherland, M. Zäch, and B. Kasemo, "Hole-mask colloidal lithography," Adv. Mater. 19, 4297–4302 (2007).

[31] C. Qu and E. C. Kinzel, "Polycrystalline metasurface perfect absorbers fabricated using microsphere photolithography," Opt. Lett. 41, 3399–3402 (2016).

[32] N. Denkov, O. Velev, P. Kralchevski, I. Ivanov, H. Yoshimura, and K.Nagayama, "Mechanism of formation of two-dimensional crystals from latex particles on substrates," Langmuir 8, 3183–3190 (1992).

[33] Y. Cheng, P. G. Jönsson, and Z. Zhao, "Controllable fabrication of large-area 2D colloidal crystal masks with large size defect-free domains based on statistical experimental design," Appl. Surf. Sci. 313, 144–151 (2014).

[34] J. Chen, P. Dong, D. Di, C. Wang, H. Wang, J. Wang, and X. Wu, "Controllable fabrication of 2D colloidal-crystal films with polystyrene nanospheres of various diameters by spin-coating," Appl. Surf. Sci. 270, 6–15 (2013).

[35] M. Szekeres, O. Kamalin, R. A. Schoonheydt, K. Wostyn, K. Clays, A. Persoons, and I. Dekany, "Ordering and optical properties of monolayers and multilayers of silica spheres deposited by the Langmuir-Blodgett method," J. Mater. Chem. 12, 3268–3274 (2002).

[36] B. G. Prevo and O. D. Velev, "Controlled, Rapid Deposition of Structured Coatings from Micro- and Nanoparticle Suspensions," Langmuir 20, 2099–2107 (2004). (rapid convective assembly)

[37] T. Muangnapoh, A. L. Weldon, and J. F. Gilchrist, "Enhanced colloidal monolayer assembly via vibration assisted convective deposition," Appl. Phys. Lett. 103, (2013).

[38] M. Shishido and D. Kitagawa, "Preparation of ordered mono-particulate film from colloidal solutions on the surface of water and continuous transcription of film to substrate," Colloids Surfaces A Physicochem. Eng. Asp. 311, 32–41 (2007).

[39] J. Sun, C. J. Tang, P. Zhan, Z. L. Han, Z. S. Cao, and Z. L. Wang, "Fabrication of centimeter-sized single-domain two-dimensional colloidal crystals in a wedge-shaped cell under capillary forces," Langmuir 26, 7859–7864 (2010).

[40] M. Retsch, Z. Zhou, S. Rivera, M. Kappl, X. S. Zhao, U. Jonas, and L. Qin, "Fabrication of large-area, transferable colloidal monolayers utilizing self-assembly at the air/water interface," Macromol. Chem. Phys. 210, 230–241 (2009).

[41] G. S. Lazarov, N. D. Denkov, O. D. Velev, P. A. Kralchevsky, and K. Nagayama, "Formation of two-dimensional structures from colloidal particles on fluorinated oil substrate," J. Chem. Soc. Faraday Trans. 90, 2077 (1994).

[42] M. Pisco, F. Galeotti, G. Grisci, G. Quero, and A. Cusano, "Self-assembled periodic patterns on the optical fiber tip by microsphere arrays," 9634, 1–4 (2015).

[43] P. A. Kralchevsky and K. Nagayama, "Capillary forces between colloidal particles," Langmuir 10, 23–36 (1994).

[44] G. D. Moon, T. Il Lee, B. Kim, G. Chae, J. Kim, S. Kim, J. M. Myoung, and U. Jeong, "Assembled monolayers of hydrophilic particles on water surfaces," ACS Nano 5, 8600–8612 (2011).

[45] J. Yu, C. Geng, L. Zheng, Z. Ma, T. Tan, X. Wang, Q. Yan, and D. Shen, "Preparation of high-quality colloidal mask for nanosphere lithography by a combination of air/water interface self-assembly and solvent vapor annealing," Langmuir 28, 12681–12689 (2012).

[46] P. I. Stavroulakis, N. Christou, and D. Bagnall, "Improved deposition of large scale ordered nanosphere monolayers via liquid surface self-assembly," Mater. Sci. Eng. B Solid-State Mater. Adv. Technol. 165, 186–189 (2009).

VITA

Chuang Qu received his B.E. and M.E degrees in Thermal and Power Engineering from Dalian University of Technology, Dalian, China in 2012 and 2014, respectively. He received his Doctor of Philosophy in Mechanical Engineering from Missouri University of Science and Technology in May 2019. He authored and co-authored seven journal papers and eight conference papers.